

BAGRA, BHAWNA, Ph.D. Plasmon-Exciton Coupling for Enhanced Energy Conversion (2021)

Directed by Dr. Jianjun Wei. 176pp.

The primary theme of my research is the light-matter interaction that involves plasmon-exciton coupling effect on energy conversion and optical enhancement.

Plasmons are collective oscillation of electrons in metal, which leads to concentration of optical fields in the vicinity when coupled with incident light. Excitons are bound states of electron-hole pairs in molecular or semiconductor materials, having size dependent transition optical frequencies and efficient optical emission in specific cases. Plasmon and exciton interact to form a hybridized light-matter state with multitude of potential applications including, enhanced energy conversion or transportation and sensing.

However, the interaction of coupling with plasmonic nanoslit is still fragmentary. In particular, previous investigation is mostly based on interaction with the localized surface plasmon resonance (LSPR) modes and studies based on surface plasmon polariton (SPP) are still needs to be explored with the detailed energy transfer mechanism between plasmon and excitons. Furthermore, in comparison with the absorption/scattering spectra of the plasmon-exciton, which is well studied and understood, the emitting properties of exciton due to plasmon-exciton coupling are still unclear. To address these issues, we designed and fabricated the nanoslit structures having both LSPR and SPP plasmon modes and examined the different systems for plasmon-exciton coupling effect. This research work includes understanding of plasmon-exciton coupling of the nanoslit system with immobilized exciton moieties for energy conversion, specifically, light-light energy conversion, light-electric energy conversion and optical sensing of biomolecules. (1) For

light-light energy conversion, fluorescence of Carbon Nanodots (CNDs) embedded in the nanoslit arrays is investigated. Two distinct designs are examined for fluorescence of CNDs: the CNDs immobilized in different width gold nanoslits and CNDs coupled gold nanoparticles (Au NPs) hybrids immobilized inside the gold nanoslit. Results demonstrate the enhanced fluorescence of CNDs when placed in nanoslit due to plasmon induced energy transfer to the CNDs. (2) A single nanoslit photoelectrochemical cell with CNDs and TiO<sub>2</sub> immobilization is examined for light-electric energy conversion. Enhanced photocurrent generation observed and explained with plasmon-exciton coupling between plasmonic gold nanoslit and CNDs. (3) For sensing, the research investigated a microfluidic dam with plasmonic nanoledge array structure for detection of type 1 diabetes biomarkers. The shift of the plasmon frequency with respect to the refractive index of the surrounding medium utilized as a principle for detection method. In addition to the experimental studies, a semi-analytical model for surface plasmon generation analysis and Finite-difference time-domain (FDTD) method used for simulating and modeling the optical properties from the nanoslit systems, which provides insights into the underlying physics of the plasmon-exciton coupling interactions. We found plasmon-exciton coupling in the nanostructures increases the electromagnetic (EM) field intensity by plasmonic light trapping and plasmon-induced resonance energy transfer (PIRET). This enhanced field corresponds to the modification of excitation and emission rate in exciton which ultimately enhance the energy conversion process. Fundamental understanding of the plasmon-exciton coupling in this work will leads to the

applications that includes plasmonic photovoltaic, low threshold laser, ultra-sensitive biosensors, and high efficiency optoelectronic nanodevices.

PLASMON-EXCITON COUPLING FOR ENHANCED ENERGY CONVERSION

by

Bhawna Bagra

A Dissertation Submitted to  
the Faculty of The Graduate School at  
The University of North Carolina at Greensboro  
in Partial Fulfillment  
of the Requirements for the Degree  
Doctor of Philosophy

Greensboro  
2021

Approved by

Jianjun Wei

---

Committee Chair

APPROVAL PAGE

This dissertation written by BHAWNA BAGRA has been approved by the following committee of the Faculty of The Graduate School at The University of North Carolina at Greensboro.

Committee Chair	Jianjun Wei
Committee Members	Hemali Rathnayake
	Joseph Starobin
	Shyam Aravamudhan

10/12/2020  
Date of Acceptance by Committee

10/12/2020  
Date of Final Oral Examination

## ACKNOWLEDGEMENTS

First, I would like to express my sincere gratitude to my advisor, Dr. Jianjun Wei. He is a good mentor and a wonderful scientist. His doors were always open for me whenever I needed any kind of guidance. His keen interests in my projects always motivated me to exceed expectations. In my early days at JSNN, I used to be very impatient and excitable, and Dr. Wei always used to calm me down and helped me understand the need of doing proper research first before embarking on any new project. I am very thankful to him for his constant support and encouragement. Under his tutelage, I was not only groomed academically, but also professionally.

I am also grateful to my committee members – Dr. Hemali Rathnayake, Dr. Shyam Aravamudhan and Dr. Joseph Starobin who have constantly guided me along the way. Dr. Hemali provided valuable help by strengthening my solar cells concepts for one of my projects. Dr. Shyam's door was always open for me whenever I needed any help in fabrication and provided support in establishing cross-team collaborations. I cannot thank him enough for all the help he provided me. Dr. Starobin was my Physics teacher during my first year at JSNN and it was due to his teaching, that I developed keen interest in Plasmonics.

I am very thankful to my lovely lab mates, including Dr. Xinpeng Zeng, Dr. Zheng Zeng, Dr. Yiyang Liu, Dr. Taylor Mabe, Dr. Harish Chevva, Dr. Wendi Zhang, Dr. Alex Sheardy, Dr. Durga Arvapalli, Dr. Zuowei Ji, Kokougan Allado, Anitha Jayapalan, Ziyu Yin, Mengxin Liu, Frank Tukur and Masha Azami. They have not been just my lab mates, but very good friends. I want to convey special thanks to Dr Zhang

and Dr. Mabe for being my mentors during my early days. I wish everyone all the best in their future endeavors. I also want to take this opportunity to thank all my friends who are like my family in Greensboro.

Finally, I am in eternal debt to my family and in-law's family in India for their constant and unwavering support throughout my life. Special thanks to my parents for their relentless love and support. I cannot thank my husband, Mohit, enough who moved to Greensboro just so he could live with me during my Ph.D. I would not be writing this thesis if it were not for him. There are not enough words to describe how supportive he has been ever since we got married. I hope I made all my family proud, especially my newborn daughter, Aanya.

## TABLE OF CONTENTS

	Page
LIST OF TABLES .....	vii
LIST OF FIGURES .....	viii
CHAPTER	
I. INTRODUCTION .....	1
References .....	30
II. PLASMON-ENHANCED FLUORESCENCE OF CARBON NANODOTS IN GOLD NANOSLIT CAVITIES .....	38
Overview .....	38
Introduction .....	39
Experimental Section .....	42
Results .....	45
Discussion .....	51
Conclusion.....	56
References .....	58
III. DYADS OF AU NANOPARTICLES AND CARBON NANODOTS CONFINED IN PLASMONIC NANOSLITS FOR OPTICAL ENHANCEMENT .....	63
Overview .....	63
Introduction .....	63
Experimental Section .....	68
Results .....	73
Discussion .....	80
Conclusion.....	83
References .....	85
IV. PLASMON ENHANCED PERFORMANCE OF CARBON NANODOTS BASED PHOTOELECTROCHEMICAL CELL USING GOLD NANOSLIT CAVITIES .....	92
Overview .....	92
Introduction .....	92
Experimental Section .....	97
Results .....	102

Discussion .....	106
Conclusion.....	109
References .....	110
<b>V. A PLASMONIC NANOEDGE ARRAY SENSOR FOR DETECTION OF ANTI-INSULIN ANTIBODIES OF TYPE 1 DIABETES BIOMARKER.....</b>	<b>116</b>
Overview .....	116
Introduction .....	117
Experimental Section .....	122
Results and Discussion.....	126
Conclusion.....	133
References .....	135
<b>VI. CONCLUSION AND FUTURE CONSIDERATIONS.....</b>	<b>140</b>
<b>APPENDIX A. PLASMON ENHANCED FLUORESCENCE OF CNDS IN GOLD NANOSLIT CAVITIES.....</b>	<b>145</b>
<b>APPENDIX B. DYADS OF AU NANOPARTICLES AND CARBON NANODOTS CONFINED IN PLASMONIC NANOSLITS FOR OPTICAL ENHANCEMENT.....</b>	<b>164</b>
<b>APPENDIX C. A PLASMONIC NANOEDGE ARRAY SENSOR FOR DETECTION OF ANTI-INSULIN ANTIBODY OF TYPE 1 DIABETES BIOMARKER.....</b>	<b>171</b>

## LIST OF TABLES

	Page
Table 4.1. Different variables calculated for the working electrode in light. ....	104
Table 4.2. Different variables calculated for the working electrode in dark. ....	104
Table 4.3. Different variables calculated for the control experiment in presence of light.....	105

## LIST OF FIGURES

	Page
Figure 1.1. Showing change in the color of different traditional artefacts when metal nanoparticles were incorporated in the design [2]. .....	2
Figure 1.2. Schematic representation of the plasmon excitation phenomenon.....	4
Figure 1.3. Plot between frequency and wave vector for dispersion relation of incident light (brown line) and surface plasmon (pink line). .....	5
Figure 1.4. (a) Otto configuration, (b) Kretschmann configuration. ....	6
Figure 1.5. Schematic diagram showing Surface Plasmon Resonance at the interface of metal-dielectric (a) surface plasmon polariton (SPP) and (b) localized surface plasmon (LSP) [4]. .....	7
Figure 1.6. Schematic diagram showing oscillations of coupled plasmons of two nearby metallic nanostructures separated by distance 'd'.....	9
Figure 1.7. (a) Detail description of system used for study, (b) optical absorption spectrum for dimer quantum emitter system, calculated for different resonance energy (c) optical spectrum dependence on the quantum emitter resonance width (d) optical absorption spectrum dependence on the coupling strength between plasmon and quantum emitter [25] [36]. .....	13
Figure 1.8. Major mechanisms of plasmonic energy transfer from a metal to any attached molecules or material [37]. .....	15
Figure 1.9. Schematic representation of the design used for fluorescence enhancement of the fluorophore molecule coupled with the nanostructures [39]. .....	16
Figure 1.10. (a) Shows the device design of solar cells incorporating Au NPs (b) is the comparison between IPCE curves of the solar cell and the reference [46] . .....	17
Figure 1.11. Representing the use of plasmonic nanostructures at different configuration for enhanced energy conversion [62]. .....	18
Figure 1.12. Illustration of the plasmonics based nano biosensing device used for the detection or sensing of cancer biomarkers [65]. .....	19

Figure 1.13. Different nanostructure design used: gold Nanoslit, gold nanoslit array and gold nanoledge array. ....	27
Figure 2.1. A schematic view of the setup used for the light intensity measurements (top) and illustration of the protocol for the self-assembled monolayer (SAM) formation and CND immobilization on the gold nanoslit surfaces (bottom).....	42
Figure 2.2. Characterization of the CNDs by different techniques: a) AFM topography image, b) FTIR spectra, c) UV-vis absorption spectra, and d) fluorescence emission spectra.....	47
Figure 2.3. Fluorescence images of different width Nanoslit arrays with Axio Z2M microscope. (a) upper panel are images taken using 395-440 nm filter light source, lower panel are the same fluorescent images when converted to grey scale images; (b) Fluorescence images (upper panel) taken using 450-490 nm filter and converted gray scale images (lower panel); and (c) A graphic plot showing the fluorescence intensity measured with different filters corresponding to different nanoslit width arrays.....	49
Figure 2.4. Light intensity spectra. (a) Representative net light intensity spectra of CNDs at different nanoslits after subtracting the light intensity of nanoslits before deposition of CNDs; (b) Net peak light intensity for different nanoslits with immobilized CNDs plotted as function of nanoslit width. ....	50
Figure 2.5. A plot of normalized values of fluorescence and reflection light intensity of CNDs deposited in nanoslits, and the SPG efficiencies “e” at 500 nm and 700 nm incident light vs. the width of nanoslits. ....	54
Figure 2.6. Schematic diagram illustrating the proposed process of fluorescence enhancement of CNDs because of SPR generation and energy transfer in a gold nanoslit. ....	55
Figure 3.1. Schematic illustration showing the overall design used for fluorescence enhancement of the CNDs. ....	68
Figure 3.2. Characterization of the CNDs by different techniques (a) FTIR spectra (b) Fluorescence emission spectra (c) TEM image of the CNDs. ....	74
Figure 3.3. Characterization of the CNDs-Au hybrid by different techniques (a) UV-vis spectra (b) Fluorescence emission spectra (c) TEM images of the hybrid showing 1:1 interaction. Note: All characterization in above	

Figure 3.3 for hybrid was done using 10 nm Au NPs, for all other sizes, data is shown in supplementary information.....	75
Figure 3.4. SEM images of the 100 nm width of nanoslit array fabricated by E-beam lithography. (a) shows the straight line of 100 nm width, (b) is the enlarged version of the 100 nm width nanoslit array. ....	76
Figure 3.5. Fluorescence intensity spectra. (a) shows the fluorescence intensity spectra for CNDs-Au hybrid with different size of Au NPs without the nanoslit array, (b) graphical plot showing the fluorescence intensity measured with different filters corresponding to different size of Au NPs in CNDs-Au hybrid inside the nanoslit array. ....	78
Figure 3.6. Representative net light intensity spectra of CNDs-Au NPs hybrid with different size of Au nanoparticles (a) without nanoslit and (b) inside the nanoslit. ....	79
Figure 3.7. Schematic illustration of the mechanism proposed for enhanced fluorescence of CNDs in two systems, (a) CNDs immobilized in between the Au nanoslit Au NPs, (b) CNDs with Au NPs without Au nanoslit. ....	83
Figure 4.1. Light trapping or absorption by plasmonic nanostructures in device structure when used in different configurations (a) on the surface, (b) inside the active layer, or (c) and (d) as periodic arrays at metal-semiconductor interface. ....	95
Figure 4.2. Dark field mask prepared by AutoCAD used during photolithography for the fabrication of device, (a) is the mask used for first step of lithography, (b) showing the mask used for second step of lithography. ....	97
Figure 4.3. Illustration of the approach used for fabrication of the gold electrode device. ....	99
Figure 4.4. Schematic representation of the steps used for functionalization of the gold electrode surface. ....	100
Figure 4.5. Light intensity spectra showing shift in peak and decrease in light intensity after each step of functionalization. ....	101
Figure 4.6. (a-f) i-v curve for the functionalized gold nanoslit electrode for different concentration of MB in light and dark condition. ....	103

Figure 4.7. i-v curve for the control experiment in light using solar simulator in presence of light (a) photocurrent on plain gold immobilized with CNDs and TiO <sub>2</sub> (b) photocurrent measurement of gold nanoslit electrode with only TiO <sub>2</sub> nanoparticle.....	103
Figure 4.8. A schematic view of the electron transfer chain from CNDs to TiO <sub>2</sub> to Au electrode. ....	106
Figure 4.9. Schematic representation showing how plasmon induced the enhanced photocurrent generation. ....	107
Figure 5.1. Illustration of the gold surface functionalization at the gold surfaces of the nanoledge array to immobilize human insulins and the model of plasmonic nanoledge device used for biomarker or biomolecule detection. ....	120
Figure 5.2. Fabrication Process for the Flow-over Fluidic Dam using a Multi-layered Resist (MLR) Method. (A) Spin Apply SU-8 Photoresist and Soft Bake, (B) Flood Expose and Bake the SU-8 post Exposure, (C) Deposit 100 nm of SiO <sub>2</sub> atop the Cross-linked SU-8 Structural Layer, (D) Spin Apply JSR NFR 016D2 Photoresist, (E) Expose the JSR NFR Photoresist through the Photomask with Design of the Flow-over Dam, (F) Bake and Develop the JSR NFR Post Exposure, (G) Dry Etch the SiO <sub>2</sub> Layer with a CF <sub>4</sub> /O <sub>2</sub> Plasma, (H) Dry Etch the SU-8 Layer with an O <sub>2</sub> Plasma, (I) Deposit 4 nm Ti, 250 nm Au, 4 nm Ti, and 100 nm SiO <sub>2</sub> . ....	124
Figure 5.3. (a) SEM image of nanoledge array with 600 nm of periodicity. (b) represent the FIB images of the nanoledge. ....	126
Figure 5.4. Represents the transmittance curve (smoothed in red color and unsmoothed in black color) of fabricated plasmonic chip without any modification. ....	128
Figure 5.5. Representation of peak shift for anti-insulin antibody (a) in buffer and (b) in human Serum; (c) and (d) show correlation of concentration of anti-insulin antibody with respect to wavelength peak shift, the straight line shows the linear fit. ....	131
Figure 5.6. Measured peak shift for BSA and EGF to test the specificity of the plasmonic nanoledge device. ....	132

## **CHAPTER I**

### **INTRODUCTION**

Metals especially gold and silver with dimensions in the nanometer scale shows very bright colors and amazed people for many centuries. They have tremendous significance in the history of Arts, even before scientists started showing interest in investigating their fascinating optical properties. The optical properties of metal nanostructures have been used by artists all around the world to generate brilliant colors in glass artefacts. The Lycurgus cup, collection of the British museum as shown in Figure 1.1 (a) looks green in reflected light and (b) red in transmitted light. The explanation for this phenomenon was not realized until 1990, when scientist analyzed the cup using Atomic Force microscopy (AFM) [1]. Scientist found that color is observed because of the presence of nanoparticles, silver 66.2%, 31.2% gold, and 2.6% copper, up to 100 nm in size, dispersed in a glass matrix [2].

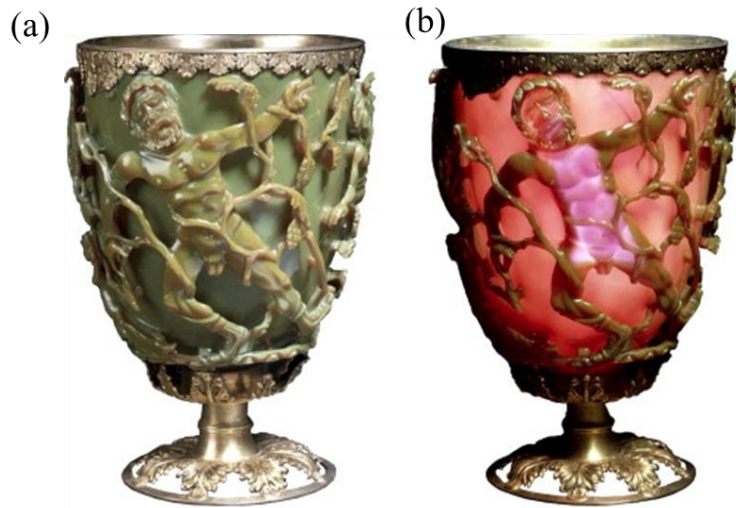


Figure 1.1. Showing change in the color of different traditional artefacts when metal nanoparticles were incorporated in the design [2].

Metal nanostructures show very complex and interesting optical properties. These amazing properties are due to the presence of free conduction electrons at their surface. The interaction of metal nanostructures with electromagnetic (EM) radiation is largely governed by these free conduction electrons. At optical frequencies, free electron gas of metals can generate plasmon polaritons which are sustained surface and volume charge density oscillations. Plasmons are the characteristic property of the nanostructured metals when they interact with light. Surface plasmons (SP) or plasmon polaritons at the interface of metal and dielectric medium can cause strongly enhanced spatially confined optical near-fields at the interface. The interest in plasmons is from the beginning of 20<sup>th</sup> century, but recent advances in structuring, manipulating, and observing nanometer scale objects have revitalized this field. Enhanced EM fields depend on the geometry of the metal as some geometries strengthen the field in the vicinity. The study of this optical

phenomenon of metals is termed as Plasmonics or nanoplasmonics. This is a rapidly growing field and many studies have been carried out to control the optical radiation at the sub-wavelength scale metallic structures. Many interesting concepts and innovative applications have been developed on metal optics in the last few years and the number of publications on Plasmonics also increasing tremendously year by year.

### ***Surface Plasmon Resonance***

SPs are the collective electron oscillations at the interface of a metal and a dielectric that are confined evanescently [3, 4]. Surface plasmon resonance (SPR) is the resonant oscillation of conduction/free electrons at the interface between metal and dielectric medium stimulated by incident light. Interaction of plasmons with EM field may result in surface plasmon excitation. When photons incident at a particular angle on the metal surface, where the projected wave vector of the incident light matches with wave vector of surface plasmons at metal-dielectric interface, it eventually leads to plasmon excitation, as shown in Figure 1.2. When there is no match between the wavevector of incident light with the wavevector of surface plasmon, there is no plasmon excitation as shown in Figure 1.2. Plasmon excitation also depends on the dielectric properties of the prism, the wavelength of light used, metal layer and on the surrounding medium.

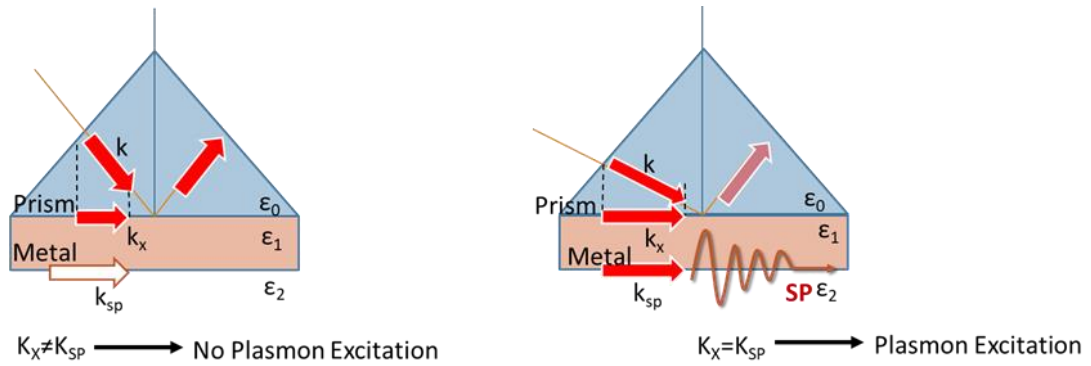


Figure 1.2. Schematic representation of the plasmon excitation phenomenon.

Dispersion relationship as shown in equation 1 gives the insight for plasmon excitation.

$$k_{sp} = \frac{\omega_{sp}}{c} \sqrt{\frac{\epsilon_m \epsilon_d}{\epsilon_m + \epsilon_d}} \quad \text{equation (1)}$$

Where  $\omega_{sp}$ , is the angular frequency,  $c$  the speed of light,  $\epsilon_d$  and  $\epsilon_m$  are the dielectric functions of the dielectric and metal, respectively.

Figure 1.3, showing plot, illustrate the dispersion relation for incident light (sky blue line) and surface plasmons (blue line). For a given frequency, there will be mismatch of momentum of incident light and surface plasmon, i.e., the wavenumber or momentum of surface plasmon is always greater than incident light.

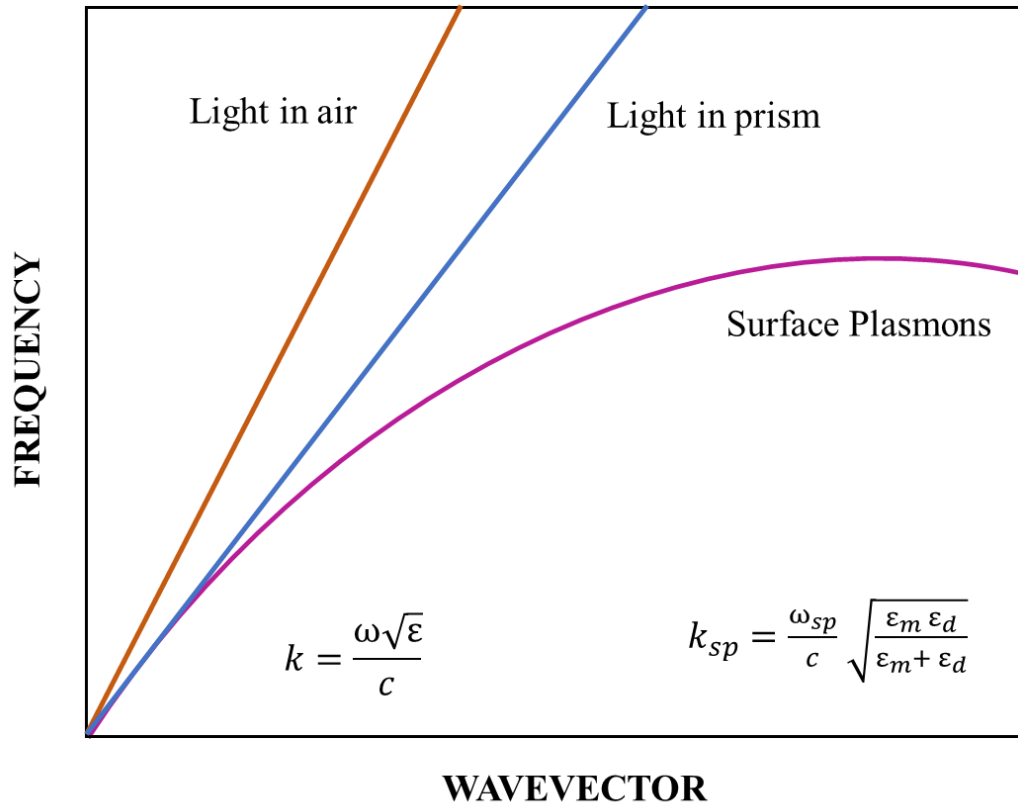


Figure 1.3. Plot between frequency and wave vector for dispersion relation of incident light (brown line) and surface plasmon (pink line).

By increasing the wavenumber or momentum of incident light, plasmons can be excited. This can be achieved either by placing the grating structure at the interface or passing the excitation light through high refractive index medium like prism. The latter case can be activated by Otto configuration as shown in Figure 1.4(a) or Kretschmann configuration as shown in Figure 1.4(b). In Otto configuration, light is illuminated on the glass substrate which results in evanescent wave at glass-air interface. This evanescent wave comes in contact with a metal-air interface and results in plasmon excitation. Plasmon excitation in Otto configuration, largely depends on the gap width between metal layer and glass substrate. In large gap width, the evanescent wave weakly

influenced by metal layer and for a small gap width, it results in inefficient excitation of plasmons [5].

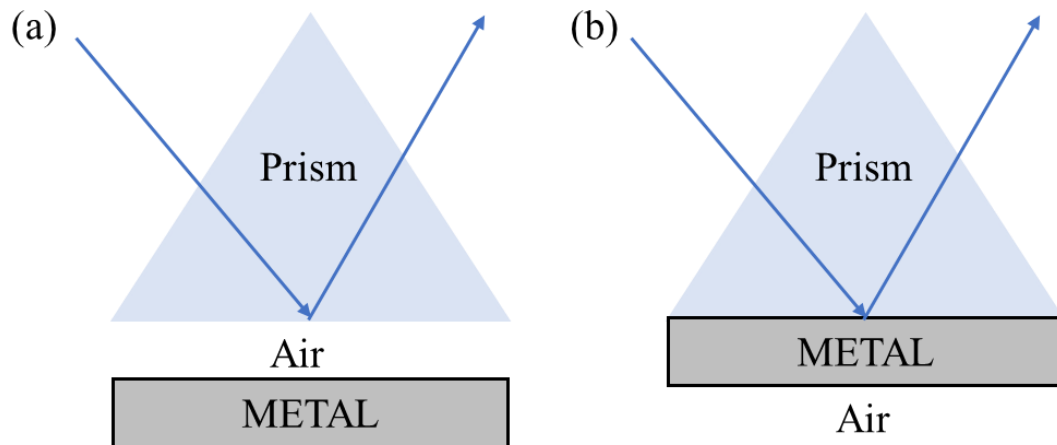


Figure 1.4. (a) Otto configuration; (b) Kretschmann configuration.

The Kretschmann configuration is the most common approach. In Kretschmann configuration, the metal layer is evaporated on the glass prism. The light is illuminated on the glass surface and evanescent wave is created at metal-glass interface. This evanescent wave then excites the plasmon at metal-air interface. For this configuration, thickness of metal layer plays an important role, thin metal layer results in damping of plasmons and if the metal layer is too thick then the plasmons will not be excited efficiently due to absorption of light by metal layer [5].

Excited SPs are of two types, propagating SPs (PSPs, Figure 1.5 (a)) and localized SPs (LSPs Figure 1.5(b)) [6]. LSPs are the spatially confined oscillations of electrons localized at the metal-dielectric interface like in nanoparticle or nanospheres and localized surface plasmon resonance (LSPR) is an optical phenomenon generated by

light. LSPR occurs when light interacts with conductive nanoparticles which are smaller than wavelength of incident light. LSPR results in an enhancement of the localized EM field, which is a fundamental basis for surface-enhanced spectroscopy [7, 8]. SPs, when coupled with photons, result in collective excitation of conduction electrons that propagate in a wave-like manner in x-y direction along an interface between a metal and a dielectric, known as SP polaritons (SPPs). SPPs are confined at the interface of metal and dielectric surface and propagate along the metal surface until the energy dissipates into free space, either by heat loss and/or by radiation [9].

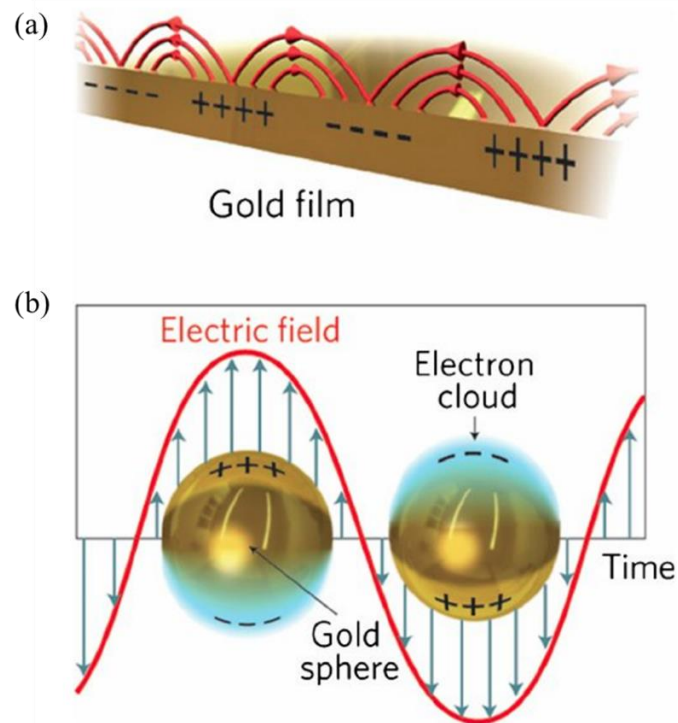


Figure 1.5. Schematic diagram showing Surface Plasmon Resonance at the interface of metal-dielectric (a) surface plasmon polariton (SPP) and (b) localized surface plasmon (LSP) [4].

Besides LSPR and SPP, there is another interesting phenomenon, plasmon-plasmon interaction[10, 11]. Plasmon-plasmon interaction, also called as plasmon-plasmon coupling or plasmon coupling, is the interaction of plasmons among nanostructure in close proximity. Coupling of plasmons results in more enhancement of localized EM field. The interaction between the metal nanostructures depends on the distance between them. When the distance is 10 nm or less, the interaction will be more and results in strong enhancement of local EM field in the vicinity[12, 13]. Plasmon coupling have enormous application including in the field of optoelectronics and biosensing [14]. Plasmon-plasmon interaction or plasmon coupling can be explained by simple oscillatory model. Surface plasmon oscillations of two nearby metallic nanostructures assumed to be represented as single classical oscillator with natural frequency of oscillation corresponding to their plasmon absorption peaks. Their natural frequency of oscillations is assigned as 'a' and 'b' separated by distance 'd' with their centers at  $X_0$ . They will start to oscillate upon external perturbation as shown in Figure 1.6. Their positions are defined as  $X_i$  and  $X_j$  respectively at any certain time. When these metal nanostructures are far apart, they will oscillate with their natural frequency and will not interact with each other. But when these metal nanostructures are at the distance of 10 nm or less, they will start to interact, and their oscillations also modifies upon external perturbation or field. Less the distance between them, more will be the interaction that results in more enhancement of electromagnetic field around them. These metal nanostructures are considered as charge particles and their interaction is defined by columbic interaction [15]. It was reported that interaction between the plasmons will be

more when the distance between metal nanostructures is 10 nm or less than 10 nm and results in strong EM field [12].

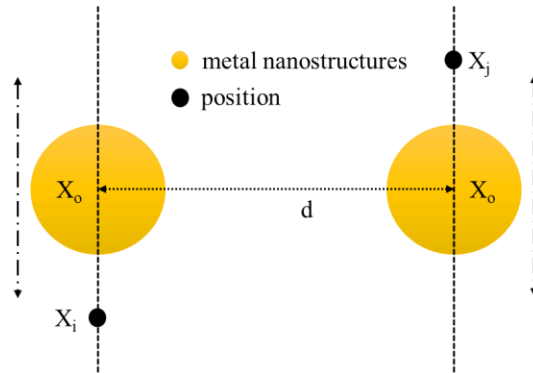


Figure 1.6. Schematic diagram showing oscillations of coupled plasmons of two nearby metallic nanostructures separated by distance ‘d’.

### ***Plasmon-exciton Coupling***

A complex system, having both plasmon and exciton excitation and their coupling, provides new and fascinating optical properties beyond that can be achieved using either of them. Exciton plays an important role in defining optical properties of molecule or semiconductor which are related to device applications and different physical phenomena. However, at nanometer scale, there is a mismatch between incident light wavelength and exciton, which results in weak light-matter interaction and impede the energy conversion efficiency. Plasmons, collective oscillation of electrons in material, annihilate the diffraction limit and couple with external field for near field enhancement. This enhanced field interacts with excitonic material, at the same time exciton presents in the plasmon near field modify the optical properties of plasmons. Therefore, coupling of

plasmon and exciton provides an ideal playground for exploration of exotic optical properties and new applications [16, 17] .

The concept of exciton was first proposed in 1931 by Frenkel [18]. When incident light is illuminated on the surface of solids , there is a formation of electron and hole [19] [20]. The electrons in the conduction band and the hole in the valence band bound by electrostatic coulomb interaction, form a new state which is called as exciton. An exciton is nothing but an electrically neutral quasi particle, stabilized by electrostatic coulomb force. Excitons have the property to transfer energy without transporting net electric charge [21, 22]. Excitons are found in semiconductors, insulators, and some liquids. The excitons are resonance stabilized by overlap of the hole and electron wavefunction, which results in increase in their lifetime and limit their decay. There has been an enormous study carried out on the interaction of exciton-plasmon coupling and their conversion to exciton-plasmon-photon [23-27]. When the resonant frequency of the SP matches with the frequency of the molecular energy level of the excitons, then there will be exchange of energy and this exchanged energy is an important factor affecting their interaction. The interaction between SP and excitons can be explained by perturbation. Perturbation is the most important method to solve the problems in quantum mechanics. It is used to compute the change in wavefunction and energy levels with the successive corrections to the zero field. Perturbation is the approach to find the approximate solution by starting with exact solution of related problem or simple problem. When the exciton molecule and the SPs are coupled into a hybrid state, there can be perturbation or no perturbation between wave functions. If there is perturbation between the wave functions of molecule

and SP, the coupling is referred to as strong coupling and when there is no perturbation then the coupling is referred to as weak coupling [28]. The interaction having perturbation in the wave functions i.e., the strong coupling, the resonance exchange energy occurs between upper and lower levels of the newly hybrid states called as Rabi oscillation. Strong coupling can be explained or proved by Rabi splitting [29] and the anticrossing phenomenon [30]. The interaction with no perturbation between wave functions defined as weak coupling results in absorption [31], SERS effects [32], fluorescence enhancement [33], and fluorescence quenching [34]. The weak coupling regime, includes well-known phenomenon like increased radiation rate, enhanced absorption cross-section and energy exchange between exciton and plasmon [35]. Several classical and quantum mechanical approaches were developed to describe plasmon-exciton system. Here, we are using Zubarev's Green Functions, to explain the plasmon-exciton coupling.

### ***Zubarev's Green Function***

Manjavacas et al. develops the quantum mechanical approach to describe the plasmon-exciton coupling [25]. The formalism is based on Zubarev's Green function and derived using Hamiltonian.

$$H_0 = \varepsilon_p d^+ d + \varepsilon_c c^+ c \quad \text{and} \quad H_{int} = -V_{pc} [d^+ c + c^+ d] \quad \text{equation (2)}$$

where  $\varepsilon_p$  is the energy of plasmon,  $\varepsilon_c$  is the energy of exciton,  $V_{pc}$  is the plasmon-exciton coupling,  $d$  and  $c$  ( $d^+$  and  $c^+$ ) are the annihilation operators for plasmon and electronic excited state in the excitonic material, respectively. Total Hamiltonian is

$$H = H_O + H_{int} + H_{decay} \quad \text{equation (3)}$$

$H_{decay}$  is the due to the dissipations of plasmon and exciton by coupling the hybrid system with a set of continuums distributed bosonic modes.

The excitation of exciton can be described as generation of electron in excited state, which is handled as fermion.

Equation for Green's function are derived as

$$(\hbar\omega - \epsilon_p + \delta\omega_p + i\frac{\Gamma_P}{2})G_{dd+} = 1 - V_{pc}G_{cd+} \quad \text{equation (4)}$$

and,

$$[\hbar\omega - \epsilon_p + (1 - 2n_c)(\delta\omega_c + i\frac{\Gamma_c}{2})]G_{cd+} = -V_{pc}(1 - 2n_c)G_{dd+} \quad \text{equation (5)}$$

they can give us Green's function  $G_{dd+}$ . Using the relation of absorption

$$\sigma = -\text{Im}G_{dd+} \quad \text{equation (6),}$$

the absorption spectrum of plasmon- exciton system is derived as

$$\sigma \propto \text{Im}[\hbar\omega - \epsilon_p + \delta\omega_p + i\frac{\Gamma_P}{2} - V_{pc}^2\alpha_c]^{-1} \quad \text{equation (7)}$$

where,

$$\alpha_c = \frac{(1-2n_c)}{\hbar\omega - \epsilon_c + (1-2n_c)(\delta\omega_c + i\frac{\Gamma_c}{2})} \quad \text{equation (8)}$$

$\alpha_c$  is the polarization of the exciton. This result indicates the plasmonic resonance modified by the interaction with the quantum emitter. The above equation can easily fit to the experimental absorption spectra and extract corresponding coupling strength. The result gives the absorption of the hybrid system as shown in Figure 1.7 [36]. When the energy detuning  $\Delta = \varepsilon_p - \varepsilon_c$  is large, the spectra show Fano asymmetric resonance around the exciton energy. When the detuning is small, the spectra show Fano dip feature, the depth of Fano dip can be controlled by plasmon-exciton coupling.

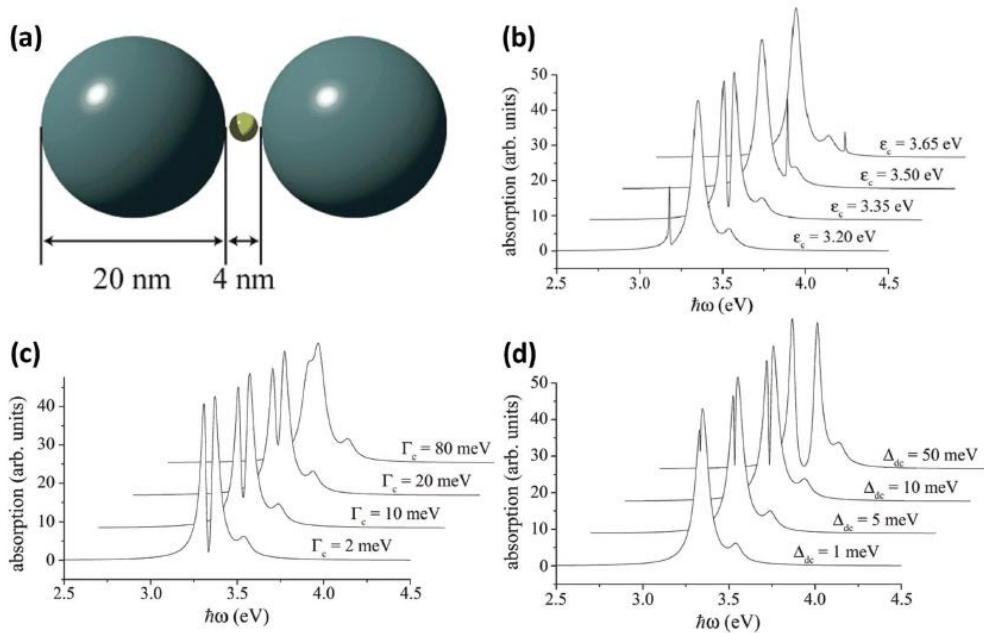


Figure 1.7. (a) Detail description of system used for study, (b) optical absorption spectrum for dimer quantum emitter system, calculated for different resonance energy (c) optical spectrum dependence on the quantum emitter resonance width (d) optical absorption spectrum dependence on the coupling strength between plasmon and quantum emitter [25] [36].

The enhanced EM field arises from the plasmon excitation and plasmon coupling can transfer their energy to the nearby attached molecule. There are three major

mechanisms of plasmonic energy transfer from a metal to any nearby attached molecule in plasmon-exciton coupling: light scattering/trapping, plasmon-induced resonance energy transfer (PIRET) and hot electron injection (also called direct electron transfer (DET) as shown in Figure 1.8 [37].

The *light scattering/trapping* process is dominant in the LSPR having metal particle typically of 50 nm in diameter [38]. When plasmonic metal nanostructure integrated with any molecule or material to form heterojunction, the incident light scattered by metal nanostructure penetrates the nearby material or molecule, which leads to increase in photon flux. This scattering effect enhances the light absorption in active material or molecule, so also called as light trapping. The light trapping event maximizes, when the plasmonic band overlap with the absorption band of the active material. This mechanism is observed both in LSPR and SPP mode. The light scattering highly depends on nanostructure shape, size and on dielectric properties of surrounding medium.

The non-radiative dissipation of plasmonic energy by metal nanostructures generates hot electrons which have high energy than the electron generated by thermal excitation. These electrons which have energy higher than the energy barrier at the interface (metal nanostructure-material/molecule), can be directly go the conduction band of the nearby material or molecule, so called as *hot electron injection*. These hot electrons have the energy higher than the conduction band and are stable and have more lifetime than the electrons generated by thermal excitation.

When the light incident on the metal nanostructures, it results in the excitation of the plasmons. Plasmon excitation generates strong dipole. The plasmonic energy from the

metal nanostructures can be transferred to the nearby molecule or material by dipole-dipole interaction. This results in generation of electron-hole pair in the nearby molecule or material. **PIRET** can occur even in the presence of insulating layer of ~25 nm between metal nanostructure and the nearby molecule or material. All these mechanisms are distance dependent. The PIRET efficiency depends on the distance between the metal nanostructure and nearby molecule or material and on the spectral overlap between the plasmonic band and absorption band of the molecule or material.

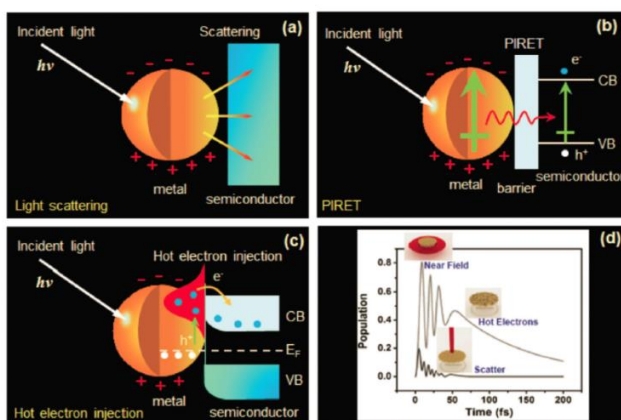


Figure 1.8. Major mechanisms of plasmonic energy transfer from a metal to any attached molecules or material [37].

### ***Application of Plasmon-Exciton Coupling***

Plasmon-exciton coupling have many amazing properties and applications. Few of the applications are discussed below.

### ***Surface enhanced fluorescence***

Lately, the use of metals to enhance the molecular fluorescence has become a hot topic of the research. Many scientists are studying the interaction between metal and

fluorescent materials to enhance their fluorescence and to get better understanding of the phenomenon [39, 40]. When light is irradiated on the surface of metal nanostructures, it creates an enhanced EM in their vicinity. This enhanced EM field absorbed by the fluorescent molecule by plasmon-exciton coupling results in increase in the luminous intensity as shown in Figure 1.9 [39, 41]. The cross section of the metal nanostructures is many times larger than the geometric scattering cross section which results in the enhancement of the local EM field when light incident on the surface of the metal nanostructures [42]. The interaction of the plasmons with the fluorescent molecule can improve the luminescence rate of the molecule, reduce the fluorescence lifetime, and improve the light stability of the luminescent molecule [33, 43, 44].

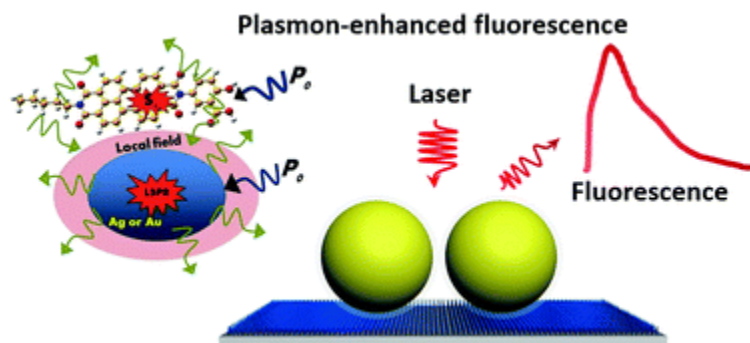


Figure 1.9. Schematic representation of the design used for fluorescence enhancement of the fluorophore molecule coupled with the nanostructures [39].

### *Solar cells*

Plasmonic nanostructures are widely used in solar cells design to convert solar energy into enhanced plasmonic energy. In solar cell design the plasmonic nanostructures used with semiconductor material as plasmonic-semiconductor heterojunction serves as light antenna to transfer enhanced plasmonic energy to semiconductor and hence,

enhance the photoconversion efficiency both above and below the band gap as shown in Figure 1.10 [45, 46].

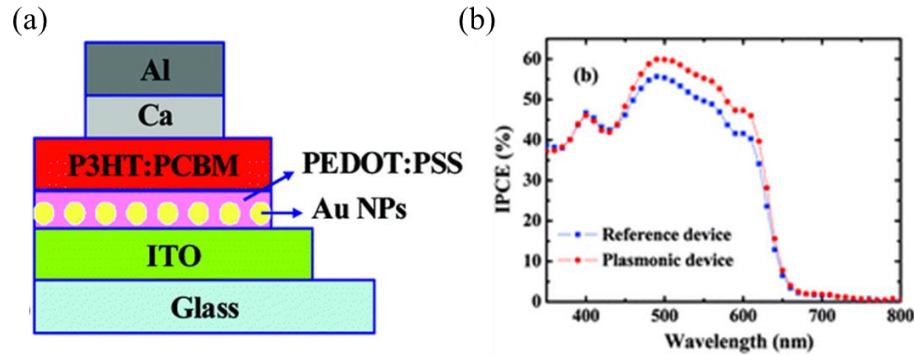


Figure 1.10. (a) Shows the device design of solar cells incorporating Au NPs (b) is the comparison between IPCE curves of the solar cell and the reference [46].

Many scientists used and proposed different design and different technologies to use plasmon excitation and light localization with SPR for the high and improved efficiency of solar cells. Plasmonic nanostructures can be used in at least three different configurations in the photovoltaic device as shown in Figure 1.11: on the surface of the device to capture incident light [47-50] embedded inside the active layer of the semiconductor to provide more light to the semiconductor by LSPR [51-54] or at the bottom interface between the semiconductor and the metal in the form of scattering nanoparticles [55, 56] or surface plasmonic gratings as shown in Figure 1.11 [57-60]. In each case the increase in efficiency is due to the different physical principle involved. When the plasmonic nanostructure is at the surface as shown in Figure 1.11 (a), more light is captured and trapped by the semiconductor due to multiple and high angle scattering, which results in increase in optical path length inside the device. When the

plasmonic nanostructures embedded inside the active layer as shown in Figure 1.11 (b), there is a strong localization and enhancement of the light within the proximity of the semiconductor which results in more or additional generation of electron-hole within the device. In the last device design as shown in Figure 1.11 (c) the use of metal gratings with periodic nanostructures array can be coupled with the light and results in surface plasmon polaritons (SPP), which propagates in the plane of the semiconductor layer and generate more electron-hole pairs [61].

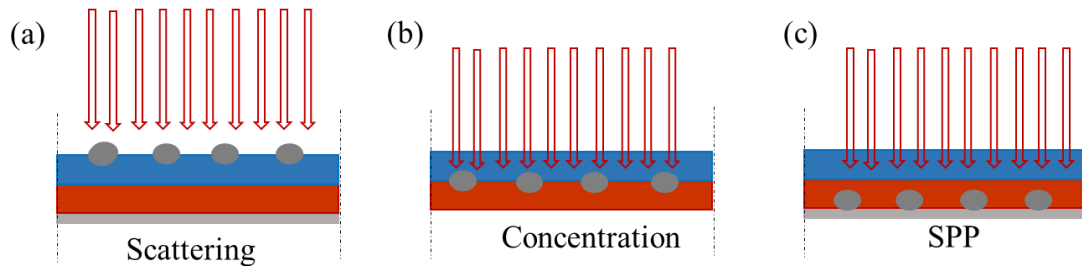


Figure 1.11. Representing the use of plasmonic nanostructures at different configuration for enhanced energy conversion [62].

### *Sensing*

This is well known fact that a vast majority of the electro-magnetic field of the surface plasmon wave (SPW) concentrate in the vicinity of the metal-dielectric interface. The propagation of the SPW is very sensitive to the refractive index of the surrounding medium. Change in refractive index of the medium cause change in the SPW and this property can be utilized as the principle of biosensing [63]. In the SPR biosensors, the biomolecules attached to the surface recognize and capture the analyte present in the fluid sample and change the refractive index of the surrounding medium at the metal surface as shown in Figure 1.12. As the thickness of the material/sample increases on the surface of

the metal, there will be a change in the refractive index and that will eventually change the SPW propagation constant along the metal surface and that can be easily determined experimentally or theoretically by wavelength shift [64, 65]. According to SPR sensing principle, there is a relationship between the wavelength shift and thickness of layer added as shown in equation [66]:

$$\Delta\lambda = m(n_A - n_B)\left[1 - \exp\left(-\frac{2d_E}{l_d}\right)\right] \quad \text{equation (9)}$$

where  $\Delta\lambda$  is the peak or wavelength shift,  $m$  is the Refractive Index Unit (RIU) sensitivity,  $n_A$  and  $n_B$  are the refractive index of the medium at the plasmonic sensing surfaces after and before the biological binding,  $d_E$  is the effective thickness of the added binding layer and,  $l_d$  is the decay length of surface plasmon mode. Addition of different concentration of analytes into the plasmonic sensor results in different layer thickness which changes the dielectric constant of the surrounding medium at the metal surfaces, eventually leading to peak shift. There is red shift with the more concentration of the analytes because more concentration means more binding and more peak shift[66].

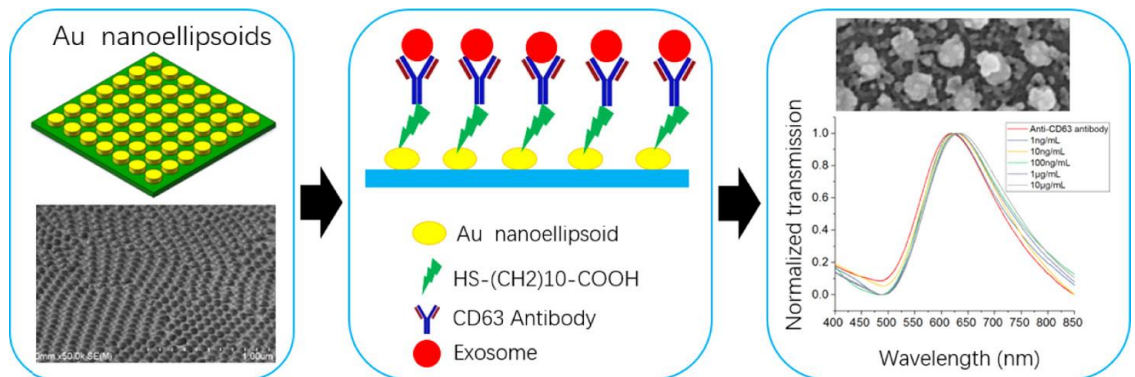


Figure 1.12. Illustration of the plasmonics based nano biosensing device used for the detection or sensing of cancer biomarkers [65].

### ***Background and Significance***

Based on above discussion, we get to know that plasmon coupling and plasmon-exciton coupling has amazing properties of light trapping and can be used for various applications. Here, we mainly focused on two applications: enhanced energy conversion and biosensing. Energy conversion devices has been a fascinating topic of research lately. Many researchers are working and trying to use natural resources like solar energy, wind energy to convert efficiently into other forms of energy, like electrical energy [67]. Similarly, in the health sector, there is ongoing research to make the immunoassays label free, sensitive, selective and cost effective. Plasmons, characteristic of metal nanostructure, with amazing properties can be applied in the field of opto-electronics and biosensing, bio-imaging, and environmental monitoring. Incorporating Plasmonics into existing energy conversion devices can increase their efficiency and yield[68]. Plasmonics and nanophotonics are considered the future of traditional light science. Nanophotonics is the combination of photonics and nanotechnology, where spatial confinement dominates light propagation and light-matter interaction. Plasmonics have the ability to control or modulate light at nanoscale level via surface plasmons. Plasmons, both LSPR and SPP, can control collective and coherent oscillation of dielectrically confined electrons, thus providing unique optical properties to metal nanostructures. Unique set of properties such as large absorption and scattering cross-section, high sensitivity to local environment and enhanced electromagnetic field at the surface, make plasmonic nanostructures as a significant material for enhanced energy conversion devices and biosensing device in future[69].

Here, in this research we worked on three systems based on Plasmon-exciton coupling: Plasmon exciton coupling for Light to enhanced light energy conversion (fluorescence enhancement of CNDs), plasmon-exciton coupling for Light to enhanced electrical energy conversion (photocurrent generation) and plasmon resonance for biosensing.

### ***Fluorescence Enhancement in complex plasmon-exciton system***

Absorption/scattering spectra of plasmon-exciton system has been investigated and studied quite well, but on the other hand the emitting properties are still far from being clear. The strong coupling between plasmon-excitonic material results in modification of fluorescence spectra of the emitting material. Plasmon-induced field enhance the fluorescence by manipulating the excitation rate  $\Gamma_{ex}$  and quantum yield  $Q$  of the emitter [70]. Along, with the increase in excitation rate, quantum yield can also be increased by optimizing the balance between radiative and non-radiative rates by adjusting the distance between metal nanostructures and the emitter. Some of the studies shows that with distance less than 2 nm, results in weak fluorescence intensity due to large non radiative transfer rate from exciton to plasmons while others show that fluorescence enhancement can be achieved by modify the emission wavelength with increase in emission intensity [71]. Fluorescence wavelength tuning, the emission shift of plasmon-exciton hybrids and modified fluorescence spectra are proportional to:

$$\chi_A(\lambda) = FL_0(\lambda) * A(\lambda) \quad \text{equation (10)}$$

where,  $FL_0(\lambda)$  is uncoupled fluorescence spectrum and  $A(\lambda)$  is extinction spectrum of plasmon [36, 72]. A study by Feng *et al.* showed enhanced fluorescence of lanthanide-

doped up conversion nanoparticles (UCNPs) using Au nanorods. They reported that fluorescence enhancement can be controlled by precisely tuning the distance between Au nanorods and UCNPs[73]. Another study shows that strong fluorescence enhancement of MoS<sub>2</sub> monolayer when coupled with Ag nanoparticles. Moreover, they observed the exciton induced dip that indicates the coherent dipole-dipole coupling between excitons of monolayer and LSP of Ag nanoparticles. Their results highlight that integration of semiconductors with plasmonic nanostructure results in strong light-matter interaction and enables their application in photonics [6]. In the metal -molecule hybrid system, Al nanoantenna and J-aggregate cyanine dye molecules were studied for fluorescence enhancement. Enhanced fluorescence was explained by enhanced absorption and increase in local density of states at the exciton-plasmon energies. This new findings will give an insight to allow hybrid state for different applications [74].While fluorescence enhancement by LSPR in various quantum dots or dyes molecule has been investigated, but data showing fluorescence enhancement using SPP still needs to be investigated. It would also be interesting to find out the relationship between the Surface Plasmon Generation (SPG) efficiency and the fluorescence enhancement.

***Photocurrent Generation in Complex plasmon-exciton system***

Coupling the semiconductor material with plasmonic nanostructures results in improved photo conversion efficiency (PCE) of photovoltaics or photocatalytic.

$$PCE = V_{OC} I_{SC} \frac{FF}{P_{in}} \quad \text{equation (11)}$$

Where,  $V_{oc}$  is open circuit voltage,  $I_{sc}$  is short circuit current, FF is fill factor, and  $P_{in}$  is input power.

Improvement in the photoconversion efficiency is due to (a) enhanced field created by LSP or SPP which results in better charge separation (b) increased absorption rate due to SPs and more light trapping (c) direct transfer of electron from plasmonic nanomaterial to excitonic material and, (d) electron storage effect that makes the fermi energy level more negative [75]. As noted earlier, the use of Plasmonics in energy conversion devices is not new, a lot of work has been carried out and investigated from last few years. To give a few examples, Wang *et al.* observed that embedding Ag nanoparticles into silicon solar cells enhances power conversion from 18.05% to 18.25% and also protects silicon solar cells from UV damage [76]. Zheng *et al.* fabricated a Photosystem I based biohybrid photoelectrochemical cell with Gold nanoslits and observed enhanced photocurrent generation with increase in SPG efficiency [77]. Plasmon-exciton coupling is a valuable means to enhance the photocurrent and improve the solar cell functionality. Though, some issue needs to be addressed before plasmonics can be applied to photovoltaics. First, the type of nanomaterial and geometry to use to attain optimal plasmonic functionality for practical applications. Second, type of solar cell to be fabricated to gain maximum improvement in efficiency by plasmon-exciton coupling. Third, to find the relationship between SPG efficiencies and photocurrent generation for optimizing the device parameters. Although, initial studies show the success of modulating energy conversion process using plasmon-exciton coupling, still

major breakthroughs yet to be come. Improvement in plasmonic solar cells technologies and new strategies will be helm of next generation solar cells.

### ***Plasmonics for Biosensing***

Due to ability of plasmonic materials to generate nanoscale hot spots close to size of biomolecules, plasmonics has been applied in biosensing with enhanced sensitivity for refractive index change. Plasmonic nanomaterials results increase field intensity which is most common way to improve plasmonic biosensing performance, but this can cause photodamage to biological samples as they are light sensitive. There are routes to increase the sensitive without photodamaging the sample like, the peak shift instead of reflectance intensities or by using quantum light source [63]. Improvement in plasmonic biosensing enables its use as point of care device in near future with various benefits including miniaturization, low sample volume, low cost, high sensitivity and specificity, simple fabrication method and less sample processing time. Initial studies show the promising results, but further investigation needs to be done to integrate the whole system as point of care device with high sensitivity levels. Some of the work which has been done in the area of SPR based biosensing device. Ayda *et al.* fabricated SPR based plastic optical fiber biosensor for the detection of C-reactive protein (CRP) in serum. The biosensor was integrated with microfluidic system for easy and stable detection. A working range of 0.006–70 mg L<sup>-1</sup> and a limit of detection of 0.009 mg L<sup>-1</sup> were achieved [78]. Ag nanoprism to round nanodiscs was used by kong *et al.* for the screening of an anti-diabetic drug, GAA inhibitor with the detection limit of 5nM [79]. Monteiro et al. built a SPR based microfluidic device using gold film for the

detection of human epidermal receptor protein-2 (HER2) antigen with the detection limit of 30 ng/mL [80]. You et al. recently developed a system with Pdots and Au nanorods for colorimetric and fluorescent readout abilities. They utilized this hybrid system for screening and for the quantitatively determination of prostate specific antigens (PSA). They observed that plasmon enhanced fluorescent Pdots possess much better detection sensitivity for PSA and can be used for on-site detection too [81].

However, the literature data in both the areas still shows very less efficiency improvement in order to be mass produced. We believe that it is essential to investigate a system that will not only improve the efficiency and sensitivity by a significant amount but also can be mass produced. Hence, we present here a new device design for all the systems for strong plasmon coupling and plasmon-exciton coupling which could overcome the challenges that we are facing now. This work provides an insight for the better understanding of the physics behind the plasmon generation efficiency and plasmonic field transfer which directly affects the energy conversion and sensing process. This new finding will facilitate the device designing that will provide the platform for fabrication of better biosensing devices and photoelectrochemical cells. To achieve the desired results, emphasis is given on the fabrication of the nanostructure films. Since nanostructured film has access to both LSPR and SPP. Patterned nanostructured film has displayed an enhanced specificity, selectivity and is cost effective.

### ***Nanostructured Substrate Designs***

One of the primary goals of the research was to vary and to investigate the nanostructure design, its composition and periodicity for enhanced EM field generation.

In order to study nanostructure geometries semi-analytical and numerical simulation was done. In the semi analytical model, the surface plasmon generation efficiency (SPG),  $\epsilon$ , defined as the rate of surface plasmon polaritons launching and scattering by matching the continuous electromagnetic field quantities at the interface, for the glass/Au interface at the bottom of the nanoslit aperture for one side of the aperture was calculated using the equations [82] discussed in chapter 2. SPG efficiency was calculated for the different width of the nanostructures design at different wavelength of light. Numerical simulations were conducted using the Finite Difference Time Domain (FDTD) method. For calculation of the electromagnetic field intensity profiles of the nanoslit a Lumerical FDTD method was used. FDTD is a versatile modeling technique that utilizes solution of Maxwell's equations to attain the plasmonic modes for SPR. FDTD, being a time-domain technique where a single simulation can provide results from a wide range of frequencies and wavelengths, is beneficial as the resonant frequency and primary SP peak are unknown when faced with many variables such as slit width, period, material composition etc. FDTD provides fundamental understanding of the EM waves and SP modes along with images and movies of how the EM modes evolve over time. Moreover, FDTD provides a quick method for the experimentalist to gain some insight into what devices need to be fabricated and further investigated [83]. Nanostructures of interest are the nanoslit, nanoslit array and the nanoledge array as shown in Figure 1.12. In chapter two and three, we will introduce nanoslit and nanoslit array design and their complete simulation for EM field intensity and SPG efficiency. In chapter four, we will introduce H-shape design with nanoslit for enhanced energy conversion. In chapter five, we will

introduce a novel design, a nanoledge array. This design, being a stair-step feature, has a large opening of 280 nm and an inner slit of 50 nm in width. The primary benefit of this design is in the fact that the large opening (280 nm in width) is large enough to easily allow the entry of charge analytes such as proteins in an aqueous solution. The 50 nm slit is required because researchers have found that slits with a width less than 100 nm provide strong SPR signals.

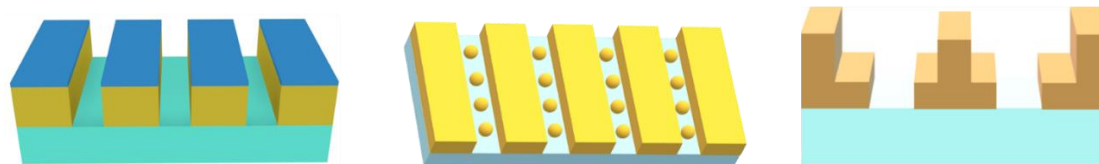


Figure 1.13. Different nanostructure design used: gold Nanoslit, gold nanoslit array and gold nanoledge array.

### ***Brief Introduction of all the chapters***

All the following chapters are in the area of plasmon-exciton coupling and micro-nanofabrication. A brief introduction of all the chapters is outlined below.

A nanoslit and nanoslit array design was fabricated in chapter II to examine its ability to enhance fluorescence of CNDs. Nanoslit and nanoslit array design of different nanoslit width was fabricated on glass substrate already coated with gold (Au) by Focused ion beam (FIB) lithography. A SiO<sub>2</sub> capping layer was introduced to promote binding of CNDs inside the nanoslit. CytoViva Hyperspectral imaging system and Axio Z2M microscope was used to investigate the enhanced fluorescence of CNDs.

Relationship between Surface plasmon generation efficiency (SPG) and enhanced fluorescence was established.

A coupled system with gold nanoslit and Au nanoparticles (Au NPs) to enhance the fluorescence of CNDs was studied in chapter III. Simulated 100 nm width nanoslit array was fabricated using e-beam lithography. The fluorescence of CNDs -Au NPs hybrid studied both in solution and inside the nanoslit array. CytoViva Hyperspectral imaging system and Axio Z2M microscope was used to investigate the fluorescence intensity. Enhanced fluorescence intensity was explained with the concept of plasmon coupling and plasmon-exciton coupling. Different size of Au NPs for the hybrid was also studied to examine the effect of size of Au NPs on the fluorescence of CNDs.

Chapter IV focused on the enhanced electric energy conversion. This chapter discussed on how plasmon exciton coupling between gold nanoslit and CNDs enhances the photocurrent generation efficiency. A device was fabricated using lithography and FIB technique. Then, the device was functionalized with CNDs and TiO<sub>2</sub> nanoparticles. Functionalized device with Methylene blue (MB) and KCl in PBS solution was used as photoelectrochemical cells. Solar simulator was used to take the i-v/p-v curve of the photoelectrochemical cell in light and dark condition. Effect of different concentration of MB on photocurrent generation was also studied. Control experiments were done on plain gold without any nanoslit to see the effect of plasmon energy on photocurrent generation and in nanoslit without CNDs to analyze the CNDs function as photosensitizer.

Biosensing for ant-insulin antibody of Type 1 diabetes, is investigated in Chapter V. The flow-over fluidic dams with nanoledge structures milled on the top was used as detection device. Plasmonic nanoledge device was functionalized with human insulin via SAM and different concentration of anti-insulin antibody was flown over the functionalized device. SPR resonant peak shifts were studied for binding reaction between human insulin and anti-insulin antibody. Control experiments were done using Epidermal growth factor (EGF) and Bovine serum albumin (BSA) to verify the selectivity and specificity of the device.

## REFERENCES

- [1] M. Loos, "Chapter 1 - Nanoscience and Nanotechnology," in *Carbon Nanotube Reinforced Composites*, M. Loos, Ed., ed Oxford: William Andrew Publishing, 2015, pp. 1-36.
- [2] I. Freestone, N. Meeks, M. Sax, and C. Higgitt, "The Lycurgus Cup — A Roman nanotechnology," *Gold Bulletin*, vol. 40, pp. 270-277, 2007/12/01 2007.
- [3] R. H. Ritchie, "Plasma Losses by Fast Electrons in Thin Films," *Physical Review*, vol. 106, pp. 874-881, 06/01/ 1957.
- [4] Z. Liang, J. Sun, Y. Jiang, L. Jiang, and X. Chen, "Plasmonic Enhanced Optoelectronic Devices," *Plasmonics*, vol. 9, pp. 859-866, 2014/08/01 2014.
- [5] E. K. Akowuah, T. Gorman, and S. Haxha, "Design and optimization of a novel surface plasmon resonance biosensor based on Otto configuration," *Optics Express*, vol. 17, pp. 23511-23521, 2009/12/21 2009.
- [6] W. Zhao, S. Wang, B. Liu, I. Verzhbitskiy, S. Li, F. Giustiniano, *et al.*, "Exciton–Plasmon Coupling and Electromagnetically Induced Transparency in Monolayer Semiconductors Hybridized with Ag Nanoparticles," *Advanced Materials*, vol. 28, pp. 2709-2715, 2016.
- [7] M. Moskovits, "Surface-enhanced spectroscopy," *Reviews of Modern Physics*, vol. 57, pp. 783-826, 07/01/ 1985.
- [8] C. Zong, M. Xu, L.-J. Xu, T. Wei, X. Ma, X.-S. Zheng, *et al.*, "Surface-Enhanced Raman Spectroscopy for Bioanalysis: Reliability and Challenges," *Chemical Reviews*, vol. 118, pp. 4946-4980, 2018/05/23 2018.
- [9] J. M. Brockman, B. P. Nelson, and R. M. Corn, "Surface Plasmon Resonance Imaging Measurements of Ultrathin Organic Films," *Annual Review of Physical Chemistry*, vol. 51, pp. 41-63, 2000.
- [10] S. L. Westcott, S. J. Oldenburg, T. R. Lee, and N. J. Halas, "Construction of simple gold nanoparticle aggregates with controlled plasmon–plasmon interactions," *Chemical Physics Letters*, vol. 300, pp. 651-655, 1999/02/12/ 1999.
- [11] A. Salmanogli, B. Nasserli, and E. Pişkin, "Plasmon-plasmon interaction effect on reproducible surface-enhanced Raman scattering for dye molecule detection," *Sensors and Actuators A: Physical*, vol. 262, pp. 87-98, 2017/08/01/ 2017.

- [12] C. Sönnichsen, B. M. Reinhard, J. Liphardt, and A. P. Alivisatos, "A molecular ruler based on plasmon coupling of single gold and silver nanoparticles," *Nature Biotechnology*, vol. 23, pp. 741-745, 2005/06/01 2005.
- [13] P. K. Jain, W. Huang, and M. A. El-Sayed, "On the Universal Scaling Behavior of the Distance Decay of Plasmon Coupling in Metal Nanoparticle Pairs: A Plasmon Ruler Equation," *Nano Letters*, vol. 7, pp. 2080-2088, 2007/07/01 2007.
- [14] M.-S. Hu, H.-L. Chen, C.-H. Shen, L.-S. Hong, B.-R. Huang, K.-H. Chen, *et al.*, "Photosensitive gold-nanoparticle-embedded dielectric nanowires," *Nature Materials*, vol. 5, pp. 102-106, 2006/02/01 2006.
- [15] A. Hazra, S. M. Hossain, A. K. Pramanick, and M. Ray, "Gold-silver nanostructures: Plasmon-plasmon interaction," *Vacuum*, vol. 146, pp. 437-443, 2017/12/01/ 2017.
- [16] J. M. Lee, J. Lim, N. Lee, H. I. Park, K. E. Lee, T. Jeon, *et al.*, "Synergistic Concurrent Enhancement of Charge Generation, Dissociation, and Transport in Organic Solar Cells with Plasmonic Metal–Carbon Nanotube Hybrids," *Advanced Materials*, vol. 27, pp. 1519-1525, 2015.
- [17] X. Luo, W. Lv, L. Du, F. Zhao, Y. Peng, Y. Wang, *et al.*, "Insight into trap state dynamics for exploiting current multiplication in organic photodetectors," *physica status solidi (RRL) – Rapid Research Letters*, vol. 10, pp. 485-492, 2016.
- [18] J. Frenkel, "On the Transformation of light into Heat in Solids. I," *Physical Review*, vol. 37, pp. 17-44, 01/01/ 1931.
- [19] J. Lagois and B. Fischer, "Experimental Observation of Surface Exciton Polaritons," *Physical Review Letters*, vol. 36, pp. 680-683, 03/22/ 1976.
- [20] F. Yang, J. R. Sambles, and G. W. Bradberry, "Long-range coupled surface exciton polaritons," *Physical Review Letters*, vol. 64, pp. 559-562, 01/29/ 1990.
- [21] E. Yablonovitch, "Inhibited Spontaneous Emission in Solid-State Physics and Electronics," *Physical Review Letters*, vol. 58, pp. 2059-2062, 05/18/ 1987.
- [22] G.-B. Liu, D. Xiao, Y. Yao, X. Xu, and W. Yao, "Electronic structures and theoretical modelling of two-dimensional group-VIB transition metal dichalcogenides," *Chemical Society Reviews*, vol. 44, pp. 2643-2663, 2015.
- [23] A. E. Schlather, N. Large, A. S. Urban, P. Nordlander, and N. J. Halas, "Near-Field Mediated Plexcitonic Coupling and Giant Rabi Splitting in Individual Metallic Dimers," *Nano Letters*, vol. 13, pp. 3281-3286, 2013/07/10 2013.

- [24] C. W. Cheng, E. J. Sie, B. Liu, C. H. A. Huan, T. C. Sum, H. D. Sun, *et al.*, "Surface plasmon enhanced band edge luminescence of ZnO nanorods by capping Au nanoparticles," *Applied Physics Letters*, vol. 96, p. 071107, 2010.
- [25] A. Manjavacas, F. J. García de Abajo, and P. Nordlander, "Quantum Plexcitonics: Strongly Interacting Plasmons and Excitons," *Nano Letters*, vol. 11, pp. 2318-2323, 2011/06/08 2011.
- [26] M. S. Tame, K. R. McEnery, Ş. K. Özdemir, J. Lee, S. A. Maier, and M. S. Kim, "Quantum plasmonics," *Nature Physics*, vol. 9, pp. 329-340, 2013/06/01 2013.
- [27] M. Sun, Z. Zhang, H. Zheng, and H. Xu, "In-situ plasmon-driven chemical reactions revealed by high vacuum tip-enhanced Raman spectroscopy," *Scientific Reports*, vol. 2, p. 647, 2012/09/11 2012.
- [28] Y. Sugawara, T. A. Kelf, J. J. Baumberg, M. E. Abdelsalam, and P. N. Bartlett, "Strong Coupling between Localized Plasmons and Organic Excitons in Metal Nanovoids," *Physical Review Letters*, vol. 97, p. 266808, 12/29/ 2006.
- [29] T. K. Hakala, J. J. Toppari, A. Kuzyk, M. Pettersson, H. Tikkanen, H. Kunttu, *et al.*, "Vacuum Rabi Splitting and Strong-Coupling Dynamics for Surface-Plasmon Polaritons and Rhodamine 6G Molecules," *Physical Review Letters*, vol. 103, p. 053602, 07/31/ 2009.
- [30] J. P. Reithmaier, G. Şek, A. Löffler, C. Hofmann, S. Kuhn, S. Reitzenstein, *et al.*, "Strong coupling in a single quantum dot–semiconductor microcavity system," *Nature*, vol. 432, pp. 197-200, 2004/11/01 2004.
- [31] I. Pockrand, J. D. Swalen, J. G. G. II, and M. R. Philpott, "Exciton–surface plasmon interactions," *The Journal of Chemical Physics*, vol. 70, pp. 3401-3408, 1979.
- [32] L. Cui, P. Wang, Y. Fang, Y. Li, and M. Sun, "A plasmon-driven selective surface catalytic reaction revealed by surface-enhanced Raman scattering in an electrochemical environment," *Scientific Reports*, vol. 5, p. 11920, 2015/07/06 2015.
- [33] B. Bagra, W. Zhang, Z. Zeng, T. Mabe, and J. Wei, "Plasmon-Enhanced Fluorescence of Carbon Nanodots in Gold Nanoslit Cavities," *Langmuir*, vol. 35, pp. 8903-8909, 2019/07/09 2019.
- [34] A. L. Rodarte and A. R. Tao, "Plasmon–Exciton Coupling between Metallic Nanoparticles and Dye Monomers," *The Journal of Physical Chemistry C*, vol. 121, pp. 3496-3502, 2017/02/16 2017.
- [35] E. Cao, W. Lin, M. Sun, W. Liang, and Y. Song, "Exciton-plasmon coupling interactions: from principle to applications," *Nanophotonics*, vol. 7, p. 145, 2018.

- [36] X. Li, L. Zhou, Z. Hao, and Q.-Q. Wang, "Plasmon–Exciton Coupling in Complex Systems," *Advanced Optical Materials*, vol. 6, p. 1800275, 2018.
- [37] N. Wu, "Plasmonic metal-semiconductor photocatalysts and photoelectrochemical cells: a review," *Nanoscale*, vol. 10, pp. 2679-2696, 2018.
- [38] N. Wu, "Plasmonic metal–semiconductor photocatalysts and photoelectrochemical cells: a review," *Nanoscale*, vol. 10, pp. 2679-2696, 2018.
- [39] J.-F. Li, C.-Y. Li, and R. F. Aroca, "Plasmon-enhanced fluorescence spectroscopy," *Chemical Society Reviews*, vol. 46, pp. 3962-3979, 2017.
- [40] E. Marlow, A. Murphy, and R. Pollard, *Investigating electromagnetic field enhancements from gold nanostructured arrays for plasmon enhanced fluorescence* vol. 11082: SPIE, 2019.
- [41] Z. Li, R. Xie, X. Li, E. Gu, L. Niu, and X. Sha, "Luminous enhancement of nitride light-emitting diodes by localized surface plasmon and triangular structure," *Superlattices and Microstructures*, vol. 120, pp. 127-135, 2018/08/01/ 2018.
- [42] R. Knoblauch and C. D. Geddes, "Review of Advances in Metal-Enhanced Fluorescence," in *Reviews in Plasmonics 2017*, C. D. Geddes, Ed., ed Cham: Springer International Publishing, 2019, pp. 253-283.
- [43] Y. Jeong, Y.-M. Kook, K. Lee, and W.-G. Koh, "Metal enhanced fluorescence (MEF) for biosensors: General approaches and a review of recent developments," *Biosensors and Bioelectronics*, vol. 111, pp. 102-116, 2018/07/15/ 2018.
- [44] P. P. Pompa, L. Martiradonna, A. D. Torre, F. D. Sala, L. Manna, M. De Vittorio, *et al.*, "Metal-enhanced fluorescence of colloidal nanocrystals with nanoscale control," *Nature Nanotechnology*, vol. 1, pp. 126-130, 2006/11/01 2006.
- [45] S. K. Cushing, A. D. Bristow, and N. Wu, "Theoretical maximum efficiency of solar energy conversion in plasmonic metal–semiconductor heterojunctions," *Physical Chemistry Chemical Physics*, vol. 17, pp. 30013-30022, 2015.
- [46] J.-L. Wu, F.-C. Chen, Y.-S. Hsiao, F.-C. Chien, P. Chen, C.-H. Kuo, *et al.*, "Surface Plasmonic Effects of Metallic Nanoparticles on the Performance of Polymer Bulk Heterojunction Solar Cells," *ACS Nano*, vol. 5, pp. 959-967, 2011/02/22 2011.
- [47] D. Zhang, X. Yang, X. Hong, Y. Liu, and J. Feng, "Aluminum nanoparticles enhanced light absorption in silicon solar cell by surface plasmon resonance," *Optical and Quantum Electronics*, vol. 47, pp. 1421-1427, 2015/06/01 2015.

- [48] A. Ono, Y. Enomoto, Y. Matsumura, H. Satoh, and H. Inokawa, "Broadband absorption enhancement of thin SOI photodiode with high-density gold nanoparticles," *Optical Materials Express*, vol. 4, pp. 725-732, 2014/04/01 2014.
- [49] T. L. Temple, G. D. K. Mahanama, H. S. Reehal, and D. M. Bagnall, "Influence of localized surface plasmon excitation in silver nanoparticles on the performance of silicon solar cells," *Solar Energy Materials and Solar Cells*, vol. 93, pp. 1978-1985, 2009/11/01/ 2009.
- [50] K. R. Catchpole and A. Polman, "Design principles for particle plasmon enhanced solar cells," *Applied Physics Letters*, vol. 93, p. 191113, 2008.
- [51] T. V. Pfeiffer, J. Ortiz-Gonzalez, R. Santbergen, H. Tan, A. S. Ott, M. Zeman, *et al.*, "Plasmonic Nanoparticle Films for Solar Cell Applications Fabricated by Size-selective Aerosol Deposition," *Energy Procedia*, vol. 60, pp. 3-12, 2014/01/01/ 2014.
- [52] P. Spinelli and A. Polman, "Prospects of near-field plasmonic absorption enhancement in semiconductor materials using embedded Ag nanoparticles," *Optics Express*, vol. 20, pp. A641-A654, 2012/09/10 2012.
- [53] J.-Y. Lee and P. Peumans, "The origin of enhanced optical absorption in solar cells with metal nanoparticles embedded in the active layer," *Optics Express*, vol. 18, pp. 10078-10087, 2010/05/10 2010.
- [54] F. Ye, M. Burns, and M. Naughton, *Embedded metallic nanopatterns for enhanced optical absorption* vol. 8111: SPIE, 2011.
- [55] M. J. Mendes, S. Morawiec, T. Mateus, A. Lyubchyk, H. Águas, I. Ferreira, *et al.*, "Broadband light trapping in thin film solar cells with self-organized plasmonic nanocolloids," *Nanotechnology*, vol. 26, p. 135202, 2015/03/11 2015.
- [56] E. Wang, T. P. White, and K. R. Catchpole, "Resonant enhancement of dielectric and metal nanoparticle arrays for light trapping in solar cells," *Optics Express*, vol. 20, pp. 13226-13237, 2012/06/04 2012.
- [57] M. R. M. Atalla, "Multiple excitations of surface-plasmon-polariton waves in an amorphous silicon p-i-n solar cell using Fourier harmonics and compound gratings," *Journal of the Optical Society of America B*, vol. 31, pp. 1906-1914, 2014/08/01 2014.
- [58] P. Prabhathan and V. M. Murukeshan, "Surface Plasmon Polariton-coupled Waveguide Back Reflector in Thin-film Silicon Solar Cell," *Plasmonics*, vol. 11, pp. 253-260, 2016/02/01 2016.

- [59] L. V. Mercaldo, I. Usatii, E. Bobeico, F. Russo, L. Lancellotti, and P. D. Veneri, "Optical Performance of Ag-based Back Reflectors with different Spacers in Thin Film Si Solar Cells," *Energy Procedia*, vol. 84, pp. 221-227, 2015/12/01/ 2015.
- [60] J. Chantana, Y. Yang, Y. Sobajima, C. Sada, A. Matsuda, and H. Okamoto, "Localized surface plasmon enhanced microcrystalline–silicon solar cells," *Journal of Non-Crystalline Solids*, vol. 358, pp. 2319-2323, 2012/09/01/ 2012.
- [61] F. Enrichi, A. Quandt, and G. C. Righini, "Plasmonic enhanced solar cells: Summary of possible strategies and recent results," *Renewable and Sustainable Energy Reviews*, vol. 82, pp. 2433-2439, 2018/02/01/ 2018.
- [62] P. Spinelli, V. E. Ferry, J. van de Groep, M. van Lare, M. A. Verschuuren, R. E. I. Schropp, *et al.*, "Plasmonic light trapping in thin-film Si solar cells," *Journal of Optics*, vol. 14, p. 024002, 2012/01/12 2012.
- [63] J. R. Mejía-Salazar and O. N. Oliveira, "Plasmonic Biosensing," *Chemical Reviews*, vol. 118, pp. 10617-10625, 2018/10/24 2018.
- [64] J. Castro Arias, A. Cattoni, D. Decanini, S. Collin, and A.-M. Haghiri-Gosnet, "Biosensing on a Chip: Study of Plasmonic Nanostructures Integrated in Microfluidic Devices," Dordrecht, 2017, pp. 491-492.
- [65] X. Lv, Z. Geng, Y. Su, Z. Fan, S. Wang, W. Fang, *et al.*, "Label-Free Exosome Detection Based on a Low-Cost Plasmonic Biosensor Array Integrated with Microfluidics," *Langmuir*, vol. 35, pp. 9816-9824, 2019/07/30 2019.
- [66] Z. Zeng, X. Shi, T. Mabe, S. Christie, G. Gilmore, A. W. Smith, *et al.*, "Protein Trapping in Plasmonic Nanoslit and Nanoledge Cavities: The Behavior and Sensing," *Analytical Chemistry*, vol. 89, pp. 5221-5229, 2017/05/16 2017.
- [67] S. V. Boriskina, H. Ghasemi, and G. Chen, "Plasmonic materials for energy: From physics to applications," *Materials Today*, vol. 16, pp. 375-386, 2013/10/01/ 2013.
- [68] N. Zhou, V. López-Puente, Q. Wang, L. Polavarapu, I. Pastoriza-Santos, and Q.-H. Xu, "Plasmon-enhanced light harvesting: applications in enhanced photocatalysis, photodynamic therapy and photovoltaics," *RSC Advances*, vol. 5, pp. 29076-29097, 2015.
- [69] H. Yu, Y. Peng, Y. Yang, and Z.-Y. Li, "Plasmon-enhanced light–matter interactions and applications," *npj Computational Materials*, vol. 5, p. 45, 2019/04/11 2019.
- [70] R. Liu, Z.-K. Zhou, Y.-C. Yu, T. Zhang, H. Wang, G. Liu, *et al.*, "Strong Light-Matter Interactions in Single Open Plasmonic Nanocavities at the Quantum Optics Limit," *Physical Review Letters*, vol. 118, p. 237401, 06/08/ 2017.

- [71] T. Ozel, P. L. Hernandez-Martinez, E. Mutlugun, O. Akin, S. Nizamoglu, I. O. Ozel, *et al.*, "Observation of Selective Plasmon-Exciton Coupling in Nonradiative Energy Transfer: Donor-Selective versus Acceptor-Selective Plexcitons," *Nano Letters*, vol. 13, pp. 3065-3072, 2013/07/10 2013.
- [72] M. Fang, Z. Huang, T. Koschny, and C. M. Soukoulis, "Electrodynamic Modeling of Quantum Dot Luminescence in Plasmonic Metamaterials," *ACS Photonics*, vol. 3, pp. 558-563, 2016/04/20 2016.
- [73] A. L. Feng, M. L. You, L. Tian, S. Singamaneni, M. Liu, Z. Duan, *et al.*, "Distance-Dependent Plasmon-Enhanced Fluorescence of Upconversion Nanoparticles using Polyelectrolyte Multilayers as Tunable Spacers," *Scientific Reports*, vol. 5, p. 7779, 01/14/online 2015.
- [74] E. Eizner, O. Avayu, R. Ditcovski, and T. Ellenbogen, "Aluminum Nanoantenna Complexes for Strong Coupling between Excitons and Localized Surface Plasmons," *Nano Letters*, vol. 15, pp. 6215-6221, 2015/09/09 2015.
- [75] P. V. Kamat, "Quantum Dot Solar Cells. The Next Big Thing in Photovoltaics," *The Journal of Physical Chemistry Letters*, vol. 4, pp. 908-918, 2013/03/21 2013.
- [76] T. Wang, S. Zou, J. Zhu, Z. Lu, H. Sun, X. Ye, *et al.*, "Enhancing power conversion efficiency of multicrystalline silicon solar cells by plasmonic effect of Ag nanoparticles embedded in SiNx layer," *AIP Advances*, vol. 9, p. 025218, 2019.
- [77] Z. Zeng, T. Mabe, W. Zhang, B. Bagra, Z. Ji, Z. Yin, *et al.*, "Plasmon-exciton Coupling in Photosystem I Based Biohybrid Photoelectrochemical Cells," *ACS Applied Bio Materials*, 2018/08/15 2018.
- [78] A. Aray, F. Chiavaioli, M. Arjmand, C. Trono, S. Tombelli, A. Giannetti, *et al.*, "SPR-based plastic optical fibre biosensor for the detection of C-reactive protein in serum," *Journal of Biophotonics*, vol. 9, pp. 1077-1084, 2016.
- [79] W. Kong, D. Wu, N. Hu, N. Li, C. Dai, X. Chen, *et al.*, "Robust hybrid enzyme nanoreactor mediated plasmonic sensing strategy for ultrasensitive screening of anti-diabetic drug," *Biosensors and Bioelectronics*, vol. 99, pp. 653-659, 2018/01/15/ 2018.
- [80] J. P. Monteiro, J. H. de Oliveira, E. Radovanovic, A. G. Brolo, and E. M. Girotto, "Microfluidic Plasmonic Biosensor for Breast Cancer Antigen Detection," *Plasmonics*, vol. 11, pp. 45-51, 2016/02/01 2016.
- [81] P.-Y. You, F.-C. Li, M.-H. Liu, and Y.-H. Chan, "Colorimetric and Fluorescent Dual-Mode Immunoassay Based on Plasmon-Enhanced Fluorescence of Polymer Dots for Detection of PSA in Whole Blood," *ACS Applied Materials & Interfaces*, vol. 11, pp. 9841-9849, 2019/03/13 2019.

[82] P. Lalanne, J. P. Hugonin, and J. C. Rodier, "Theory of Surface Plasmon Generation at Nanoslit Apertures," *Physical Review Letters*, vol. 95, p. 263902, 12/28/2005.

[83] Z. Zeng, M. N. Mendis, D. H. Waldeck, and J. Wei, "A semi-analytical decomposition analysis of surface plasmon generation and the optimal nanoledge plasmonic device," *RSC Advances*, vol. 6, pp. 17196-17203, 2016.

## **CHAPTER II**

### **PLASMON-ENHANCED FLUORESCENCE OF CARBON NANODOTS IN GOLD NANOSLIT CAVITIES**

This chapter has been published as: Bagra, B., Zhang, W., Zeng, Z., Mabe, T., Wei, J. (2019). Plasmon-Enhanced Fluorescence of Carbon Nanodots in Gold Nanoslit Cavities. *Langmuir* 2019, 35, 27, 8903–8909.

#### **Overview**

Carbon nanodots (CNDs) are featured with wide range of light absorption and excitation dependent fluorescence. The emission enhancement of CNDs is of great interest for development of nanophotonics. While the phenomenon of plasmon-enhanced fluorescence for quantum dots and molecular dyes has been well investigated, rarely has it been reported for CNDs. In this work, a series of plasmonic nanoslit designs were fabricated and utilized for immobilization of carbon nanodots (CNDs) in nanoslit and examination of the best match for plasmonic fluorescence enhancement of CNDs. In concert, to better understand the plasmon effect on the enhancement, surface optical field is measured with or without CNDs immobilization using a hyperspectral imaging system as a comparison, and a semi-analytical model is conducted for a quantitative analysis of surface plasmon generation (SPG) under the plane-wave illumination. Both the fluorescence and surface reflection light intensity enhancement demonstrate as a function of nanoslit width and are maximized at the 100 nm nanoslit width. The analysis of surface plasmon-exciton coupling of CNDs in the nanoslit area suggests the enhancement

is primarily due to plasmonic light trapping for increased electromagnetic field and plasmon-induced resonance energy transfer. This study suggests that incorporating CNDs in the plasmonic nanoslits may provide a largely enhanced CNDs-based photoemission system for optical applications.

## **Introduction**

Fluorescence is one of the most utilized phenomena in various fields like optical devices, microscopy imaging, biology, medical research, and diagnosis. For many of these applications, it is desirable to enhance the fluorescence to obtain greater signal from less sample. Surface plasmons (SPs)[1, 2] on subwavelength nanostructured surfaces were found to be capable of fluorescence enhancement.[3] The optical phenomena of SPs lies in considerably the conductive surfaces through manipulating the geometry of subwavelength apertures with a periodic structure.[4, 5] The plasmonic enhanced fluorescence results in a variety of applications, such as bio-detection and biosensing schemes.[6, 7] Specifically, many cancer biomarkers, hormones, allergens, and proteins have been detected by SPR biosensors with high accuracy and sensitivity.[8] Nevertheless, improving fluorescence sensitivity for single molecular detection is still undertaken for the development of the next generation fluorescent systems.[9-12]

Propagating or localized surface plasmons can couple to incident photons, resulting in a confinement of the electromagnetic field. This interaction is associated with large enhancement of the field and local optical density of states. When a fluorophore is coupled to the plasmonic-coupling surface, the enhanced field can be utilized to increase excitation rate, thus enhancing and controlling far field angular distribution of

fluorescence.[13] Further, due to their high sensitivity to geometry and surroundings, SPs can concentrate light within sub-wavelength volumes.[14, 15] Lately, plasmon coupling interaction has been used to increase light absorption and fluorescence of CNDs based on coupling to a localized surface Plasmon resonance (LSPR) of metallic nanoparticles.[16, 17]

Carbon nanodots (CNDs) have attracted great attention because of their promising characteristics like having strong, tuneable photoluminescence and good opto-electronic properties.[18, 19] The fluorescence in CNDs is due to bandgap transitions, but the nature of the transitions is not fully understood.[20-23] These transitions could arise from conjugated  $\pi$ -domains, bond disorder induced energy gaps,[24, 25] and/or giant red-edge effects that give rise to fluorescence depending on strong excitation wavelength.[26, 27] Light emission has also been attributed to quantum confinement effects,[28] size dependent optical properties,[29] surface-related defect sites,[30] and radiative recombination of excited surface states.[31]

While plasmonic enhancement of fluorescence from quantum dots (QDs) or dye molecules has been investigated,[13, 32-34] research of plasmonic effect on the fluorescence of CNDs is rare, especially CNDs on nanostructured conductors. Instead, CNDs were reported to have plasmonic effect to increase the fluorescence of ZnO QDs.[35] Over the past few years, a significant amount of work has been done to enhance the fluorescence of CNDs by working on tuning their structure. It has been noticed recently that fluorescence of CNDs can be enhanced on the gold films when CNDs were labelled on bacteria cells.[36]

Considering that the fluorescence properties of CNDs could be modulated by the enhanced fields derived from the spatially confined surface plasmons corresponding to the optical excitation at or near the resonant energies, there are few findings on the localized SPR (LSPR) and/or Surface Plasmon Polariton (SPP) effect and how it helps in enhancement of fluorescence of CNDs. It also would be interesting to find out the fundamental relationship between the fluorescence enhancement and the surface plasmon generation (SPG) efficiency. Here the SPG is described as the rate of SPP launching, propagation and scattering by matching the continuous electromagnetic fields quantities at the dielectric-metallic interface.[37, 38] Recently, we observed the plasmon-exciton coupling effect on light energy conversion to photocurrent by a system where photosystem I is embedded in plasmonic nanoslits and correlation to the SPG efficiency of the nanoslits-based photoelectrochemical cell.[39]

In this study, a nanoslit design for fluorescence enhancement setup is used and fluorescence enhancement of CNDs in these plasmonic nanoslits is observed. The CNDs are immobilized in a nanoscale slit and the nanoslit is illuminated with a light source for spectral and fluorescent imaging measurements (table 2.1). The nanoslit arrays used in this study have slit widths of 50, 100, 200, 300, 400, or 500 nm. The present work demonstrates that tuning the width of nanoslit provides a good match for CNDs excitation and induces fluorescence enhancement from the CNDs immobilized in nanoslit arrays. The fluorescence enhancement correlates to the nanoslit width-dependent SPG efficiencies. In concert, the near-field light intensity spectra are measured in a reflection mode upon an incident white light as a comparison to the fluorescence enhancement. The

mechanisms for the optical enhancement are discussed on the basis of plasmonic-exciton coupling interaction in the nanoslit gap.

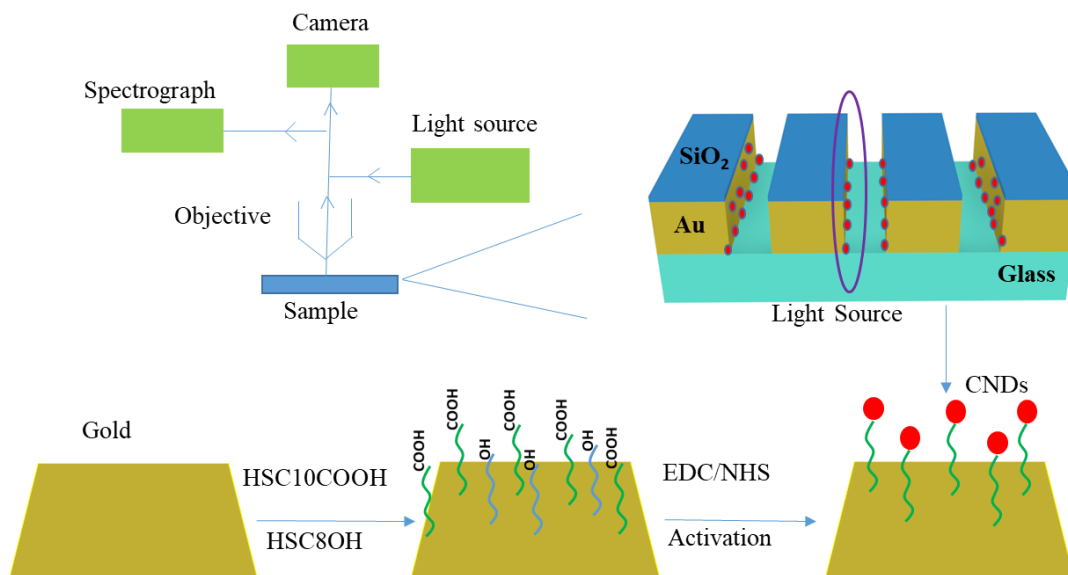


Figure 2.1. A schematic view of the setup used for the light intensity measurements (top) and illustration of the protocol for the self-assembled monolayer (SAM) formation and CND immobilization on the gold nanoslit surfaces (bottom).

## Experimental Section

### *Synthesis and Characterization of CNDs*

CNDs were synthesized from urea and citric acid using a previously reported microwave-assisted procedure.[19, 40]. Briefly, citric acid (1.0 g, 99%, ACROS Organics) and urea (1.0 g, 99.5%, Aldrich) were simultaneously added to 1.0 mL deionized water forming a homogenous solution. Then, a microwave synthesizer (CEM Corp 908005) was used to heat the solution (300 W for 18 minutes). Next, to remove aggregated and large particles, the cooled down aqueous reaction solution was purified using a centrifuge (Solvall Legend XFR Floor Model Centrifuge) for 20 minutes at 3500

rpm. The sample was dialyzed for 24 hours (1000 MWCO, Fisher Scientific) against deionized water (three times) to purify the dark-brown solution. Lastly, a freeze-dryer (FreeZone 6, Labconco) was used to dry the resultant solution for 24 hours to obtain the solid sample.

Atomic force microscopy (5600LS AFM, Agilent) was used to test the size of the purified CNDs on a freshly cleaved mica surface. To study the chemical structure and elemental content of the CNDs, Fourier transform infrared spectroscopy (670 FTIR, Varian) was used. UV-vis spectroscopy (Cary 6000i, Agilent) and fluorescence spectroscopy (Cary Eclipse, Agilent) were used to study the optical properties of the CNDs. Both UV-Vis and fluorescence were obtained using CNDs dissolved in DI water at a concentration of 0.05 mg/mL.

### ***Fabrication of device***

Glass cover slips were used as substrates and were cleaned in a piranha bath (3:1 H<sub>2</sub>SO<sub>4</sub>/H<sub>2</sub>O<sub>2</sub>), rinsed with DI water, dried with a nitrogen stream, and cleaned in an oxygen plasma (200 W, 2 min). The substrates were then dehydrated on a hot plate at 180 °C. Metal deposition was performed by e<sup>-</sup>-beam evaporation (Kurt Lesker PVD75 e<sup>-</sup>-beam evaporator). After reaching a base pressure of  $1.4 \times 10^{-6}$  Torr, Ti was evaporated at a rate of 0.3 Å/s to a thickness of 2.2 nm, Au was evaporated at a rate of 1.2 Å/s to a thickness of 150.3 nm, then Ti was evaporated at a rate of 0.4 Å/s to a thickness of 2.4 nm. SiO<sub>2</sub> was used as a capping layer and 10.2 nm was deposited atop the final Ti layer at a rate of 0.8 Å/s. Nanoslits were milled in the center of each substrate with focused ion beam milling using a 30kV;50pA probe and a dose of 0.250-0.400 nc/μm<sup>2</sup>. (Zeiss

Auriga). Each device was milled to have either one slit (with a slit width of 50, 100, 200, 300, 400, or 500 nm) at the center (Figure S 2.1) or an array of nanoslits of different width (50, 100, 200, 300, or 400 nm) with periodicity of 500 nm (Figure S 2.2). As a control, a burn box was made by completely milling an area the same size as the nanoslit arrays.

### ***Preparation of immobilized CNDs onto the gold electrode surface***

Gold-coated cover slips with individual or arrayed nanoslits were first cleaned with O<sub>2</sub> plasma (South Bay Technologies PC2000 Plasma Cleaner) for 10 minutes. The coverslips were then incubated in a mixture of 11-mercaptopundecanoic acid (HS(CH<sub>2</sub>)<sub>10</sub>COOH, Sigma Aldrich) and 8-mercapto-octanol (HS(CH<sub>2</sub>)<sub>8</sub>OH, Sigma Aldrich) in an absolute ethanol solution (ACROS Organics) with a 1:2 mole ratio for 24 hours to form a self-assembled monolayer (SAM). After SAM formation, the gold slides were incubated in 0.5 mM 1-(3-dimethylaminopropyl)-3-ethylcarbodiimide hydrochloride (EDC, TCI)/ N-hydroxysuccinimide (NHS, Sigma Aldrich) for 2 hours to activate the carboxylic acid groups. Next, the gold slide was rinsed with deionized water and immediately moved to a freshly prepared 10 mL solution containing 0.05 mg/mL of CNDs for 2 hours. The gold cover slips were rinsed with deionized water and dried before experiment.

### ***Fluorescence imaging and intensity***

Fluorescence measurements were carried out using Axio Z2M microscope in reflection mode. Axio Z2M microscope is an optical microscope with different filters (blue, green, red). For fluorescence measurements in reflection mode, images were

acquired using a 20X objective lens, 9.25 s exposure time, and one of two filters: 430 nm (395-440 nm) or 480 nm (450-490nm). These fluorescent images of the nanoslits were converted into gray scale images by MATLAB program and then ImageJ software were used to calculate the fluorescence intensity.

### ***Reflection Intensity measurement***

In addition to the Axio Z2M microscope, intensity measurements were also carried out using hyperspectral imaging (CytoViva). The CytoViva hyperspectral imaging system has both an optical imaging mode and a hyperspectral imaging mode. Hyperspectral imaging technology is specifically developed for spectral characterization and spectral mapping of nanoscale samples. The optical imaging system equipped with a 100X objective lens and white light source (400-1000 nm) was used to focus the sample, allowing the hyperspectral image to be taken. Three measurements were taken for each device before the deposition of CNDs and 9 measurements for each device after deposition of nanodots.

## **Results**

### ***CNDs synthesis and characterization***

AFM (Figure 2.2a) with associated height profile analysis (Figure S 2.1) indicates that the CNDs have an average size of about 2-3 nm. Note that some of them are as large as about 5 nm as the orange circle shows. As a note; since the radius of curvature for the AFM probe is larger than the CNDs, the x and y data does not accurately represent the size of the particles, however the height data can be used to accurately determine the particle size. According to the FTIR spectra (Figure 2.2b),  $\nu(\text{N-H})$  and  $\nu(\text{O-H})$  are

observed according to the presence of broad bands (from 3100  $\text{cm}^{-1}$  to 3400  $\text{cm}^{-1}$ ), which suggests that the CNDs are hydrophilic and stable in aqueous solution.[19] The FTIR signals at 765 (C-C), 1182 (C-O), 1418 (C=C) and 1563 (C=O)  $\text{cm}^{-1}$  are assigned respectively.[40, 41] UV-Vis absorption (Figure 2c) shows two main features; the  $n-\pi^*$  transition of the C=O moieties can be detected at about 330 nm,[20] and the feature between 400 nm and 500 nm is attributed to transition of surface states.[42] No absorption features can be found above 700 nm. CNDs have been used as a fluorescent dye in bioimaging applications because of their excitation-dependent photoluminescence.[43] Figure 2.2d shows the fluorescence emission spectra of CNDs in deionized water (0.05 mg/mL) under different excitation conditions ( $\lambda_{\text{ex}}$  ranging from 330 to 510 nm). The longer excitation wavelength induced an obvious red-shift in the fluorescence emission spectra. At an excitation wavelength of 360 nm, a maximum peak emission presents at 435 nm. Hence, the CNDs are characterized with a diameter of ~2-3 nm sphere, possess surface functionalities (e.g. carboxylates and amines/amides), and display absorbance signals below 700 nm and excitation-dependent fluorescence properties.

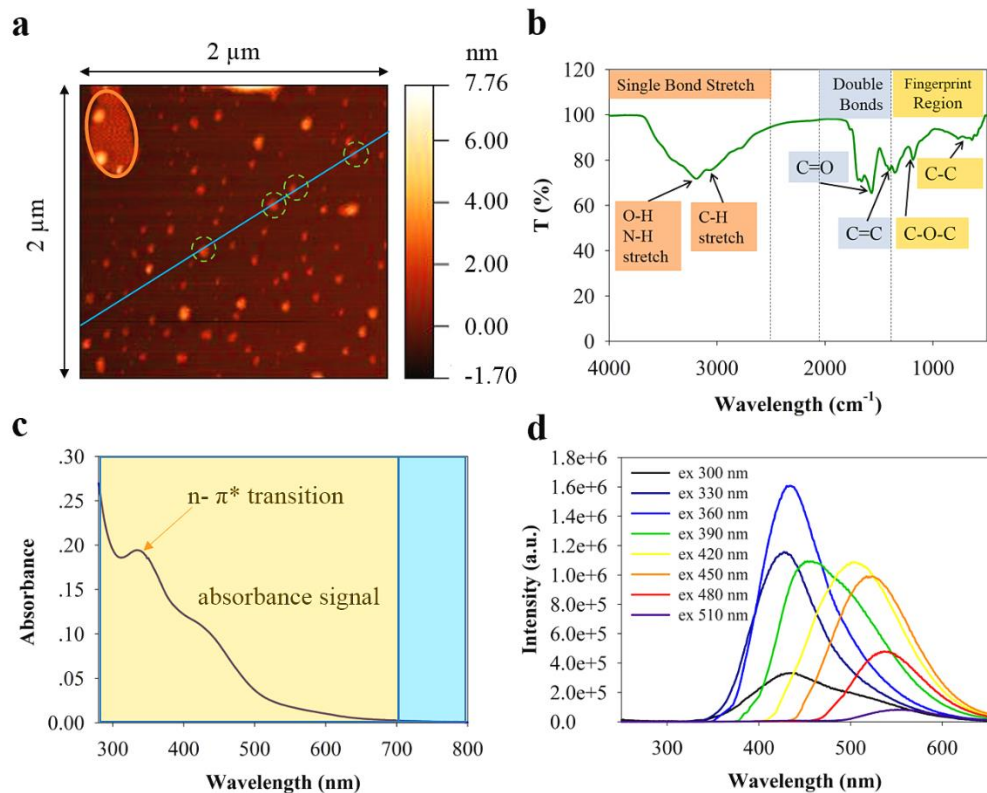


Figure 2.2. Characterization of the CNDs by different techniques: a) AFM topography image, b) FTIR spectra, c) UV-vis absorption spectra, and d) fluorescence emission spectra.

### ***Metallic Nanoslit Fabrication and CNDs Immobilization***

Metallic nanoslit films of Au were designed and fabricated to conduct the fluorescence and light illumination experiments. Representative SEM images of the nanoslit arrays at slit width at 50, 100, 200, 300, 400 nm and individual nanoslits are shown in Figures S 2.2, S 2.3. The SEM images clearly show straight nanoslits or nanoslit arrays in metallic films. To study the fluorescence and light intensity signals, CNDs were immobilized on both sides of the nanoslit area with a self-assembly monolayer (SAM) formation using 11-mercaptodecanoic acid and 8-mercapto-

octanol.[19] The SAM bridge makes the distance between the CNDs and gold surfaces around 1 nm.

### ***Fluorescence Imaging and Intensity***

Fluorescence measurements were taken using Axio Z2M microscope. The slit arrays of different width (Figure S 2.2) were used in this measurement, since a single nanoslit was invisible under the Axio Z2M microscope. CNDs were immobilized in nanoslit arrays and burn box (control) with a self-assembly method. Figure 2.3 (a,b) shows the optical fluorescence images and grey scale images of different width nanoslit arrays under the two excitation wavelengths after deposition of CNDs. There was no fluorescence in the nanoslit array before deposition of CNDs, but after deposition of CNDs, strong fluorescence images of the nanoslit arrays were obtained. No or little fluorescence was observed inside the burn box.

The fluorescence images were converted to grayscale using the MATLAB image processing tool without changing the original intensity. Then ImageJ software was used to calculate the integrated intensity of each nanoslit array using the same area. Figure 2.3(c) shows the calculated intensity of the two different filters used for fluorescent imaging (Table S 2.1, S 2.2). The resulting intensity distribution of the nanoslit arrays is similar upon two different excitation lights, but slightly higher when using longer excitation wavelength. Regardless of the excitation wavelength, maximum intensity is observed for the 100 nm width nanoslit array and minimum for the burn box.

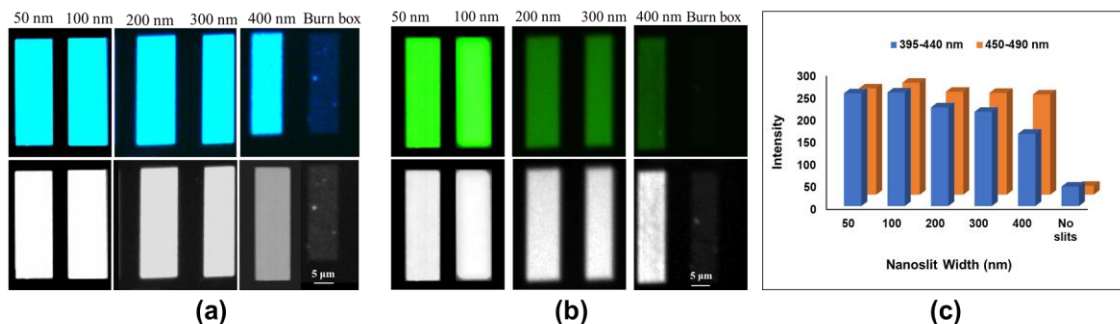


Figure 2.3. Fluorescence images of different width Nanoslit arrays with Axio Z2M microscope. (a) upper panel are images taken using 395-440 nm filter light source, lower panel are the same fluorescent images when converted to grey scale images; (b) Fluorescence images (upper panel) taken using 450-490 nm filter and converted gray scale images (lower panel); and (c) A graphic plot showing the fluorescence intensity measured with different filters corresponding to different nanoslit width arrays.

### ***Reflection Light Intensity and Spectra***

The reflective light intensity spectra of the immobilized CNDs were obtained by the CytoViva hyperspectral microscope in a reflection mode (Figure S 2.4, S 2.5). Figure 2.4a shows representative net intensity spectra measured for different nanoslits after deposition of CNDs by subtracting the background intensity of nanoslit only. Figure 2.4b presents the averaged peak intensity of the net light intensity spectra as a function of the nanoslit width (data see Table S 2.3, S 2.4). Note that the average value of the net light intensity was obtained from nine measurements (3 measurements from 3 devices) for each nanoslit width. The highest light intensity both with and without CNDs was observed when using 100 nm width slits, and this device also presented the highest net intensity. In contrast, the reflective intensity of burned box is very small and insignificant, and peak intensity less than 500 a.u. for CNDs on plane gold substrate vs ~10,000 a.u. in 100 nm nanoslit. The intensity increases indicate the near field

electromagnetic (EM) field enhancement by the plasmonic nanoslits. The results from this experiment and the fluorescence show similar trends with respect to nanoslit width, suggesting a strong plasmon-exciton coupling effect on the EM field enhancement which promotes the fluorescence enhancement of CNDs.

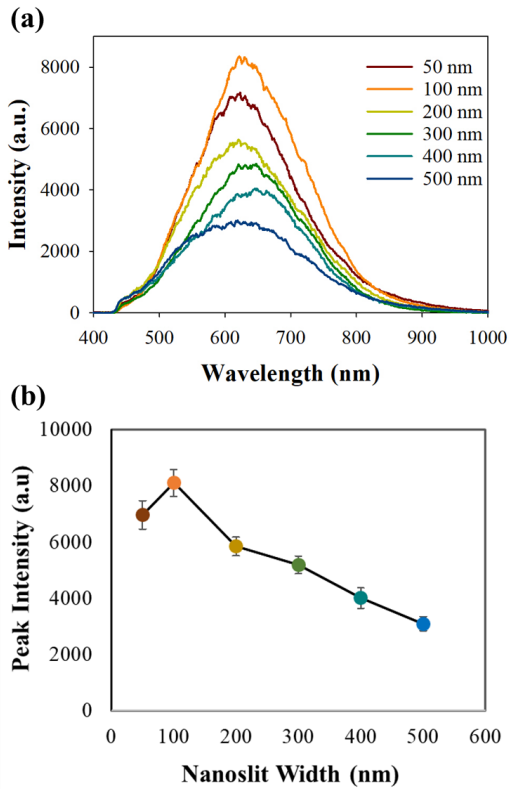


Figure 2.4. Light intensity spectra. (a) Representative net light intensity spectra of CNDs at different nanoslits after subtracting the light intensity of nanoslits before deposition of CNDs; (b) Net peak light intensity for different nanoslits with immobilized CNDs plotted as function of nanoslit width.

### *Surface Plasmon Resonance (SPR) analysis of Gold Nanoslit*

To investigate the effect of plasmon-exciton coupling on the fluorescence enhancement, the SPR of various metallic nanoslit structures with respect to the light source was examined. A mechanistic description of the SPP scattering coefficients and

efficiencies at the slit apertures is needed regarding the geometric diffraction with the bounded SPP modes launching on the flat interfaces surrounding the slits.[37, 38, 44, 45] The scheme in Figure S 2.7(a) shows the various parameters of the nanoslit structure to calculate SPG efficiencies “ $e$ ” by a plane wave at normal incidence. The SPG efficiency at one side of nanoslit aperture is calculated according to a semi-analytical mode reported earlier.[38, 39] The results of SPG analysis are shown in Figure S 2.7b and Table S 2.5, S 2.6 which are used in following discussion as a comparison with experimental results (Figure 2.5). The surface plasmon excitation is efficient at visible frequencies while “ $e$ ” decreases rapidly with increase in wavelength. The “ $e$ ” value from a 100 nm nanoslit is the highest when the wavelength of incident light is longer than 600 nm, however decreasing nanoslit width increases the “ $e$ ” value with incident light below 600 nm.

## **Discussion**

Surface-attached molecular fluorescence signal enhancement depends on the local EM intensity to the molecules, quantum yield, and the energy transfer process.[6, 46-48] Assuming the same quantum yield of CND fluorescence at gold surfaces in different slits, the fluorescence enhancement of CNDs is arising from the local EM field enhancement, and/or energy transfer. Since the nanoslit structure generates both LSPR and SPP, SP-induced trapping/scattering of incident light in nanoslit cavities containing CNDs will lead to exciton-plasmon coupling effect, dominating the enhancement of the fluorescence.[47] Hence, it is expected a mechanism of SP-coupled emission enhancement and/or excitation enhancement.[6] Namely, there should be some overlap of the SP-induced EM field with the wavelength of photoemission or absorption of CNDs.

The reflection spectra show SP-induced light wavelength ranging from 450-900 nm (Figure S 2.4, Figure 2.4) which has some overlap with the absorption band of CNDs (Figure 2.2c) (see Figure S 2.8). The fluorescence by two excitation wavelengths at 395-440 nm and 450-490 nm produces emission spectra from 400 nm up to 650 nm (Figure 2.2d), and these spectra overlap with the SP-induced EM field as well. It is interesting to observe that there is more emission overlap at the longer excitation wavelength with the local EM field at excitation light of 450-490 nm. This may be one of the factors that the longer excitation light (450-490 nm) has higher enhancement especially at larger nanoslit width than that of excitation light at 395-440 nm.

One concern is that why the fluorescence of the immobilized CNDs would not be quenched by the gold surfaces. While fluorescence of a chromophore can be quenched by closely linked gold nanostructures, the quenched fluorescence can be enhanced by a paired plasmonic noble metal nanostructures if there are plasmon coupling interactions. Recently, Zhu et al reported that fluorescence of a cyanine probe is quenched by a linked gold nanoparticle, but its fluorescence can be turned on when the immobilized probe is put into the gap region of coupled gold nanoparticles.[49] In this work, the CNDs are immobilized in one side of the nanoslit surface and located in the gap of the nanoslit. It is believed that the plasmon exciton coupling effect in nanoslits is the origin of the fluorescence enhancement. A further analysis is discussed below.

The SPG efficiency is a good parameter to further examine the relative strength of the plasmon-exciton coupling-induced EM field in the nanoslits of different width and the effect on fluorescence enhancement. For a comparison, Figure 2.5 presents a plot of

normalized values of averaged fluorescence, reflected light peak intensities, and the SPG efficiency “ $\epsilon$ ” versus the width of nanoslits. Note that the SPG was analyzed without immobilization of CNDs, representing the SP field strength in the nanoslit cavities. Both the fluorescence and reflection light intensities follow the same order of  $L_{100} > L_{50} > L_{200} > L_{300} > L_{400}$  (the subscripted number represents the nanoslit width in nm). In other words, the 100 nm nanoslit provides the strongest local field in terms of the enhancement of fluorescence and reflected light intensity, which is reasonably consistent with the calculated SPG efficiency. This suggests that the fluorescence property of CNDs is strongly influenced by the increase in localized EM field which results from the excitation of the plasmon resonance near the gold nanoslits. A previous report on EM field modeled using a finite-difference time-domain (FDTD) simulation (Figure S 2.9) demonstrated the same order of EM field strength and surface light intensity measurement.[39]

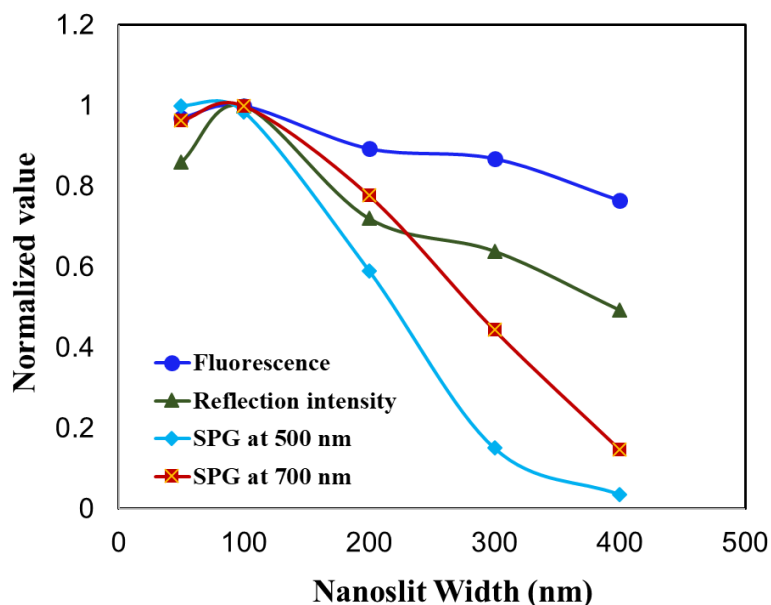


Figure 2.5. A plot of normalized values of fluorescence and reflection light intensity of CNDs deposited in nanoslits, and the SPG efficiencies “e” at 500 nm and 700 nm incident light vs. the width of nanoslits.

The difference of the fluorescence enhancement from the reflection light and the SPG efficiencies suggests additional energy transfer process contributing to the fluorescence enhancement. Other than the aforementioned light trapping, there are a few energy transfer mechanisms proposed for plasmonic enhancement, including fluorescence resonance energy transfer (FRET),<sup>[50]</sup> hot electron injection (direct electron transfer), and plasmon-induced resonance energy transfer (PIRET).<sup>[51, 52]</sup> The small distance (< 10 nm) and absorption overlap between the CNDs and the gold surface makes plasmonic FRET possible, but efficiency is expected to be low due to Stoke’s shift energy transfer from the metal nanoslit structure to the CNDs.<sup>[50]</sup> Meanwhile, the hot electron injection is minimized due to the interfacial barrier and low efficiency (< 1%).<sup>[53]</sup> Considering the lifetime of plasmon, near-field coherent PIRET would be an

alternative process for the efficient plasmonic energy transfer between the gold film in nanoslits and the attached CNDs while the plasmon still maintains excited.[54]

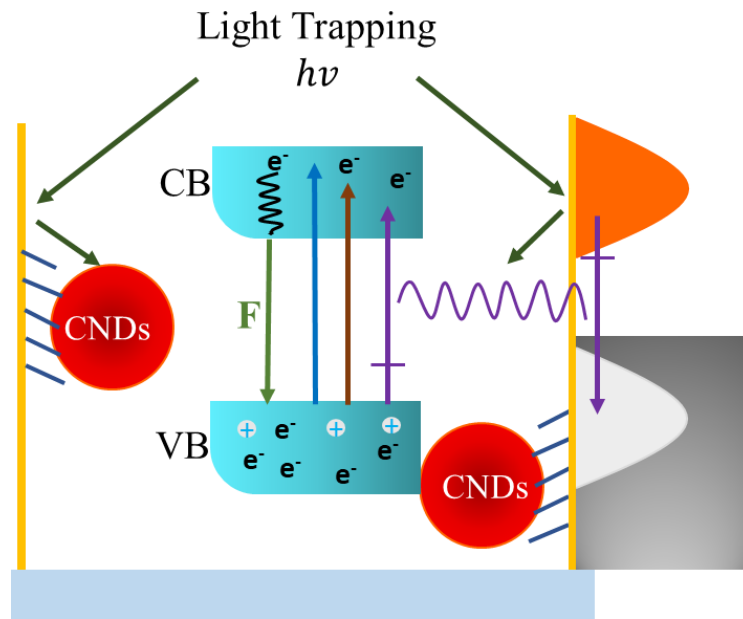


Figure 2.6. Schematic diagram illustrating the proposed process of fluorescence enhancement of CNDs because of SPR generation and energy transfer in a gold nanoslit.

Figure 2.6 depicts a schematic illustration of plasmon-exciton coupling effect on fluorescence enhancement of CND immobilized in the metallic nanoslit surface. For this hybrid metal-CNDs system, the plasmonic light trapping and the PIRET between gold nanoslit and CNDs play major roles in the enhanced fluorescence generation. Firstly, the enhanced field by light concentration in the nanoslit presents an overlap with the absorption and emission spectra of CNDs. Secondly, due to the existence of multiple interband transition dipoles in the CNDs,[19] first order dipole-dipole coupling between the plasmon in gold, and resonance dipoles in CNDs (purple color array in Figure 2.6), a resonance energy transfer from the metal film to the CNDs occurs, via the PIRET

process.[52] It is expected as well that higher SPG efficiency would provide increased dipole-dipole coupling, thus increasing energy transfer rate. Both the light trapping and PIRET enables generation of more energetic electrons in CNDs, causing increased populations in the conduction band (CB) from the valence band (VB). As a result, more electrons at the higher energy levels of conduction band of the CNDs may lead to enhanced photoemission. Furthermore, increased energetic electron generation in the conduction band potentially speeds the kinetics of relaxation to the VB, resulting in more emission per unit time. In this case, the fluorescence quantum yield increases. The above discussion conforms the effective fluorescence enhancement of the CNDs with the SPG efficiency of the plasmonic setup with nanoslit width dependence and maximized enhancement at 100 nm slit width in this work.

## **Conclusion**

In this report, we demonstrate the influence of SPR on fluorescence intensity of the CNDs by immobilizing the CNDs on gold surface in nanoslits. The fluorescence intensity is greatly enhanced, which corresponds to the calculated surface plasmon generation (SPG) efficiency by comparing the experimental results to a semi-analytical analysis of the SPG efficiency. Among the studied width of nanoslits at 50, 100, 200, 300, 400, 500 nm, respectively, the 100 nm width nanoslit presents the highest fluorescence enhancement of ~10x demonstrating an excitation wavelength dependence. The surface optical field measured as a reflection light intensity under a broad-spectrum incident light increases to ~ 6x when CNDs is deposited. The results are discussed using the phenomenon of plasmon-exciton coupling focusing on increase in the local EM field

surrounding the nanoslit and plasmon induced resonance energy transfer. These factors correspond to the enhancement in excitation and modification of emission rate of CNDs that ultimately enhance the fluorescence intensity of CNDs. This study offers promise for the development of a new CNDs-plasmon-based platform which can be used in optical biosensors and nanoscale optical devices.

## REFERENCES

- [1] H. Raether, *Surface Plasmons on Smooth and Rough Surfaces and on Gratings*: Springer, Berlin, 1988.
- [2] H. Qi, Y. Fei, Y. Yin, S. Lifang, L. Kailin, X. Zhongdang, *et al.*, "Tunable fluorescence from patterned silver nano-island arrays for sensitive sub-cell imaging," *Journal of Physics D: Applied Physics*, vol. 46, p. 495302, 2013.
- [3] H. Ditlbacher, J. R. Krenn, N. Felidj, B. Lamprecht, G. Schider, M. Salerno, *et al.*, "Fluorescence imaging of surface plasmon fields," *Applied Physics Letters*, vol. 80, pp. 404-406, 2002/01/21 2002.
- [4] W. L. Barnes, A. Dereux, and T. W. Ebbesen, "Surface plasmon subwavelength optics," *Nature*, vol. 424, p. 824, 08/14/online 2003.
- [5] M. Taylor, Z. Zheng, B. Bhawna, R. James, and J. Wei, "Surface Plasmon Resonance of A Bimetallic Nanostructured Film for Enhanced Optical Sensitivity," *ChemistrySelect*, vol. 3, pp. 3018-3023, 2018.
- [6] M. Li, S. K. Cushing, and N. Wu, "Plasmon-enhanced optical sensors: a review," *Analyst*, vol. 140, pp. 386-406, 2015.
- [7] M. Bauch, K. Toma, M. Toma, Q. Zhang, and J. Dostalek, "Plasmon-Enhanced Fluorescence Biosensors: a Review," *Plasmonics*, vol. 9, pp. 781-799, August 01 2014.
- [8] J. Homola, "Surface Plasmon Resonance Sensors for Detection of Chemical and Biological Species," *Chemical Reviews*, vol. 108, pp. 462-493, 2008/02/01 2008.
- [9] S. M. J. L. van den Wildenberg, B. Prevo, and E. J. G. Peterman, "A Brief Introduction to Single-Molecule Fluorescence Methods," in *Single Molecule Analysis: Methods and Protocols*, E. J. G. Peterman, Ed., ed New York, NY: Springer New York, 2018, pp. 93-113.
- [10] F. Emmanuel and G. Samuel, "Surface enhanced fluorescence," *Journal of Physics D: Applied Physics*, vol. 41, p. 013001, 2008.
- [11] X. Li, Y. He, and L. Que, "Fluorescence Detection and Imaging of Biomolecules Using the Micropatterned Nanostructured Aluminum Oxide," *Langmuir*, vol. 29, pp. 2439-2445, 2013/02/19 2013.

- [12] Y. Fu, J. Zhang, and J. R. Lakowicz, "Largely Enhanced Single-Molecule Fluorescence in Plasmonic Nanogaps Formed by Hybrid Silver Nanostructures," *Langmuir*, vol. 29, pp. 2731-2738, 2013/02/26 2013.
- [13] F. Tam, G. P. Goodrich, B. R. Johnson, and N. J. Halas, "Plasmonic Enhancement of Molecular Fluorescence," *Nano Letters*, vol. 7, pp. 496-501, 2007/02/01 2007.
- [14] P. Pattnaik, "Surface plasmon resonance," *Applied Biochemistry and Biotechnology*, vol. 126, pp. 79-92, August 01 2005.
- [15] J. Homola, S. S. Yee, and G. Gauglitz, "Surface plasmon resonance sensors: review," *Sensors and Actuators B: Chemical*, vol. 54, pp. 3-15, 1999/01/25/ 1999.
- [16] D.-D. Xu, C. Liu, C.-Y. Li, C.-Y. Song, Y.-F. Kang, C.-B. Qi, *et al.*, "Dual Amplification Fluorescence Assay for Alpha Fetal Protein Utilizing Immunohybridization Chain Reaction and Metal-Enhanced Fluorescence of Carbon Nanodots," *ACS Applied Materials & Interfaces*, vol. 9, pp. 37606-37614, 2017/11/01 2017.
- [17] Y. Zhang, J. Zhang, J. Zhang, S. Lin, Y. Huang, R. Yuan, *et al.*, "Intense enhancement of yellow luminescent carbon dots coupled with gold nanoparticles toward white LED," *Dyes and Pigments*, vol. 140, pp. 122-130, 2017/05/01/ 2017.
- [18] P. Miao, K. Han, Y. Tang, B. Wang, T. Lin, and W. Cheng, "Recent advances in carbon nanodots: synthesis, properties and biomedical applications," *Nanoscale*, vol. 7, pp. 1586-1595, 2015.
- [19] Z. Zeng, W. Zhang, D. M. Arvapalli, B. Bloom, A. Sheardy, T. Mabe, *et al.*, "A fluorescence-electrochemical study of carbon nanodots (CNDs) in bio- and photoelectronic applications and energy gap investigation," *Physical Chemistry Chemical Physics*, vol. 19, pp. 20101-20109, 2017.
- [20] L. Wang, S.-J. Zhu, H.-Y. Wang, S.-N. Qu, Y.-L. Zhang, J.-H. Zhang, *et al.*, "Common Origin of Green Luminescence in Carbon Nanodots and Graphene Quantum Dots," *ACS Nano*, vol. 8, pp. 2541-2547, 2014/03/25 2014.
- [21] K. Hola, A. B. Bourlinos, O. Kozak, K. Berka, K. M. Siskova, M. Havrdova, *et al.*, "Photoluminescence effects of graphitic core size and surface functional groups in carbon dots: COO<sup>-</sup> induced red-shift emission," *Carbon*, vol. 70, pp. 279-286, 2014/04/01/ 2014.
- [22] F. Nicoli, D. Verschueren, M. Klein, C. Dekker, and M. P. Jonsson, "DNA Translocations through Solid-State Plasmonic Nanopores," *Nano Letters*, vol. 14, pp. 6917-6925, 2014/12/10 2014.

- [23] P. Chen, M. T. Chung, W. McHugh, R. Nidetz, Y. Li, J. Fu, *et al.*, "Multiplex Serum Cytokine Immunoassay Using Nanoplasmonic Biosensor Microarrays," *ACS nano*, vol. 9, pp. 4173-4181, 03/23 2015.
- [24] Z. Luo, P. M. Vora, E. J. Mele, A. T. C. Johnson, and J. M. Kikkawa, "Photoluminescence and band gap modulation in graphene oxide," *Applied Physics Letters*, vol. 94, p. 111909, 2009/03/16 2009.
- [25] S. N. Baker and G. A. Baker, "Luminescent Carbon Nanodots: Emergent Nanolights," *Angewandte Chemie International Edition*, vol. 49, pp. 6726-6744, 2010.
- [26] S. K. Cushing, M. Li, F. Huang, and N. Wu, "Origin of Strong Excitation Wavelength Dependent Fluorescence of Graphene Oxide," *ACS Nano*, vol. 8, pp. 1002-1013, 2014/01/28 2014.
- [27] S. Zhu, J. Shao, Y. Song, X. Zhao, J. Du, L. Wang, *et al.*, "Investigating the surface state of graphene quantum dots," *Nanoscale*, vol. 7, pp. 7927-7933, 2015.
- [28] H. Li, X. He, Z. Kang, H. Huang, Y. Liu, J. Liu, *et al.*, "Water-Soluble Fluorescent Carbon Quantum Dots and Photocatalyst Design," *Angewandte Chemie International Edition*, vol. 49, pp. 4430-4434, 2010.
- [29] Y.-P. Sun, B. Zhou, Y. Lin, W. Wang, K. A. S. Fernando, P. Pathak, *et al.*, "Quantum-Sized Carbon Dots for Bright and Colorful Photoluminescence," *Journal of the American Chemical Society*, vol. 128, pp. 7756-7757, 2006/06/01 2006.
- [30] L. Cao, M. J. Meziari, S. Sahu, and Y.-P. Sun, "Photoluminescence Properties of Graphene versus Other Carbon Nanomaterials," *Accounts of Chemical Research*, vol. 46, pp. 171-180, 2013/01/15 2013.
- [31] R. Liu, D. Wu, S. Liu, K. Koynov, W. Knoll, and Q. Li, "An Aqueous Route to Multicolor Photoluminescent Carbon Dots Using Silica Spheres as Carriers," *Angewandte Chemie International Edition*, vol. 48, pp. 4598-4601, 2009.
- [32] L. Zhang, Y. Song, T. Fujita, Y. Zhang, M. Chen, and T.-H. Wang, "Large Enhancement of Quantum Dot Fluorescence by Highly Scalable Nanoporous Gold," *Advanced Materials*, vol. 26, pp. 1289-1294, 2014/02/01 2013.
- [33] T. Ming, H. Chen, R. Jiang, Q. Li, and J. Wang, "Plasmon-Controlled Fluorescence: Beyond the Intensity Enhancement," *The Journal of Physical Chemistry Letters*, vol. 3, pp. 191-202, 2012/01/19 2012.
- [34] R. I. Nooney, O. Stranik, C. McDonagh, and B. D. MacCraith, "Optimization of Plasmonic Enhancement of Fluorescence on Plastic Substrates," *Langmuir*, vol. 24, pp. 11261-11267, 2008/10/07 2008.

- [35] D.-Y. Guo, C.-X. Shan, K.-K. Liu, Q. Lou, and D.-Z. Shen, "Surface plasmon effect of carbon nanodots," *Nanoscale*, vol. 7, pp. 18908-18913, 2015.
- [36] R. Bukasov, O. Filchakova, K. Gudun, and M. Bouhrara, "Strong Surface Enhanced Florescence of Carbon Dot Labeled Bacteria Cells Observed with High Contrast on Gold Film," *Journal of Fluorescence*, vol. 28, pp. 1-4, 2018/01/01 2018.
- [37] P. Lalanne, J. P. Hugonin, and J. C. Rodier, "Theory of Surface Plasmon Generation at Nanoslit Apertures," *Physical Review Letters*, vol. 95, p. 263902, 12/28/2005.
- [38] Z. Zeng, M. N. Mendis, D. H. Waldeck, and J. Wei, "A semi-analytical decomposition analysis of surface plasmon generation and the optimal nanolegged plasmonic device," *RSC advances*, vol. 6, pp. 17196-17203, 02/03 2016.
- [39] Z. Zeng, T. Mabe, W. Zhang, B. Bagra, Z. Ji, Z. Yin, *et al.*, "Plasmon-exciton Coupling in Photosystem I Based Biohybrid Photoelectrochemical Cells," *ACS Applied Bio Materials*, 2018/08/15 2018.
- [40] W. Zhang, Z. Zeng, and J. Wei, "Electrochemical Study of DPPH Radical Scavenging for Evaluating the Antioxidant Capacity of Carbon Nanodots," *The Journal of Physical Chemistry C*, vol. 121, pp. 18635-18642, 2017/08/31 2017.
- [41] L. Wei, Z. Zehui, K. Biao, F. Shanshan, W. Jinxiu, W. Lingzhi, *et al.*, "Simple and Green Synthesis of Nitrogen-Doped Photoluminescent Carbonaceous Nanospheres for Bioimaging," *Angewandte Chemie International Edition*, vol. 52, pp. 8151-8155, 2013.
- [42] S. Zhu, Y. Song, X. Zhao, J. Shao, J. Zhang, and B. Yang, "The photoluminescence mechanism in carbon dots (graphene quantum dots, carbon nanodots, and polymer dots): current state and future perspective," *Nano Research*, vol. 8, pp. 355-381, February 01 2015.
- [43] V. Georgakilas, J. A. Perman, J. Tucek, and R. Zboril, "Broad Family of Carbon Nanoallotropes: Classification, Chemistry, and Applications of Fullerenes, Carbon Dots, Nanotubes, Graphene, Nanodiamonds, and Combined Superstructures," *Chemical Reviews*, vol. 115, pp. 4744-4822, 2015/06/10 2015.
- [44] P. Lalanne, J. P. Hugonin, and J. C. Rodier, "Approximate model for surface-plasmon generation at slit apertures," *Journal of the Optical Society of America A*, vol. 23, pp. 1608-1615, 2006/07/01 2006.
- [45] Z. Zeng, Y. Liu, and J. Wei, "Recent advances in surface-enhanced raman spectroscopy (SERS): Finite-difference time-domain (FDTD) method for SERS and

sensing applications," *TrAC Trends in Analytical Chemistry*, vol. 75, pp. 162-173, 2016/01/01/ 2016.

[46] P. Anger, P. Bharadwaj, and L. Novotny, "Enhancement and Quenching of Single-Molecule Fluorescence," *Physical Review Letters*, vol. 96, p. 113002, 03/21/ 2006.

[47] E. Cao, W. Lin, M. Sun, W. Liang, and Y. Song, "Exciton-plasmon coupling interactions: from principle to applications," in *Nanophotonics* vol. 7, ed, 2018, p. 145.

[48] N. Wu, "Plasmonic metal-semiconductor photocatalysts and photoelectrochemical cells: a review," *Nanoscale*, vol. 10, pp. 2679-2696, 2018.

[49] Z. Zhu, P. Yuan, S. Li, M. Garai, M. Hong, and Q.-H. Xu, "Plasmon-Enhanced Fluorescence in Coupled Nanostructures and Applications in DNA Detection," *ACS Applied Bio Materials*, vol. 1, pp. 118-124, 2018/07/16 2018.

[50] J. R. Lakowicz, K. Ray, M. Chowdhury, H. Szmecinski, Y. Fu, J. Zhang, *et al.*, "Plasmon-controlled fluorescence: a new paradigm in fluorescence spectroscopy," *Analyst*, vol. 133, pp. 1308-1346, 2008.

[51] S. K. Cushing, J. Li, F. Meng, T. R. Senty, S. Suri, M. Zhi, *et al.*, "Photocatalytic Activity Enhanced by Plasmonic Resonant Energy Transfer from Metal to Semiconductor," *Journal of the American Chemical Society*, vol. 134, pp. 15033-15041, 2012/09/12 2012.

[52] J. Li, S. K. Cushing, F. Meng, T. R. Senty, A. D. Bristow, and N. Wu, "Plasmon-induced resonance energy transfer for solar energy conversion," *Nature Photonics*, vol. 9, p. 601, 08/10/online 2015.

[53] A. J. Leenheer, P. Narang, N. S. Lewis, and H. A. Atwater, "Solar energy conversion via hot electron internal photoemission in metallic nanostructures: Efficiency estimates," *Journal of Applied Physics*, vol. 115, p. 134301, 2014/04/07 2014.

[54] S. K. Cushing and N. Wu, "Progress and Perspectives of Plasmon-Enhanced Solar Energy Conversion," *The Journal of Physical Chemistry Letters*, vol. 7, pp. 666-675, 2016/02/18 2016.

## **CHAPTER III**

### **DYADS OF AU NANOPARTICLES AND CARBON NANODOTS CONFINED IN PLASMONIC NANOSLITS FOR OPTICAL ENHANCEMENT**

#### **Overview**

Many efforts have been carried out to enhance the fluorescence of Carbon Nanodots (CNDs) by engineering their surface or by surface functionalization. But all these methods change their properties and characteristics. Here, we offer a simple method to enhance fluorescence of CNDs, by immobilizing the hybrid of CNDs and gold nanoparticles (Au NPs) system inside gold (Au) nanoslit array. For better understanding of the plasmonic effect, the Finite difference time domain (FDTD) simulation was done for different sizes of Au NPs inside the Au nanoslit. The light intensity measurements and fluorescence measurements correlates with the simulation results and shows enhanced fluorescence of hybrid when immobilized inside the nanoslit. Enhanced fluorescence explained based on plasmon-plasmon and plasmon-exciton coupling. This new study offers promising ways for improvement in the areas of optics for optical devices and biosensing for biomedical application.

#### **Introduction**

Metallic nanoparticle has the special property called Surface plasmon resonance (SPR) which is due to presence of free electrons on their surface [1, 2]. Surface Plasmons (SPs) are the free oscillating electrons at the interface of metallic surface and a dielectric.

When these electrons are optically excited, the phenomenon is called SPR. SPR can be localized SPR (LSPR) or surface plasmon polariton (SPP) [3]. Both the SPRs have the ability to confine electro-magnetic (EM) field in their vicinity [3] and this makes them useful in different applications like analytical technologies [4, 5], photo-catalysis [6, 7], opto-electronic devices [8-12], fluorescence or optical enhancement [13, 14], and for amplifying spectroscopic signals in surface-enhanced Raman scattering (SERS) [4, 15, 16]. Besides, these, another phenomenon plasmon-plasmon coupling further results in EM field enhancement. In plasmon-plasmon coupling, when two or more metallic nanostructures separated by only a nanoscale gap, their individual plasmons can couple and leads to the further enhancement of either reflected, trapped or transmitted light.[17] [18-20] . If the gap width is 10 nm or less then there is exponential increase in enhancement [21-24] . Hence, devices based on plasmonic coupling with sub-10 nm gaps hold as promising technology in photovoltaics, SERS, biosensors, and other spectroscopies that utilizes enhanced optical capabilities. The enhancement is due to the hybridization of the plasmonic modes between the two metallic structures present in the proximity of sub-10 nm gap [21, 25] .

Optical Enhancement is one of the promising phenomena and widely used technology in various areas like in opto-electronics, microscopy, and biosensors in health care sector for qualitative or quantitative detection of biomolecules. For optical enhancement and its use in practical application, there should be increase in signal to noise ratio (SNR) [26, 27]. To increase the SNR, various systems have been introduced such as plasmonic nanostructures [28, 29], photonic crystals [30, 31] and alumina

nanopores [32, 33]. It has been reported that optical enhancement with photonic porous structures like in silica [34] and in metal organic framework [35] is 7- to 10-fold, with optical interference mirrors (about 40-fold) [36], with metallic nanoparticles (6- to 25-fold) [37-39], and by the prism-based surface plasmon resonance (SPR) (10- to 47-fold [40]). Therefore, for high SNR or to increase the enhancement, one of the best and efficient solutions is to use metallic plasmonic nanostructures. When metallic nanostructures were brought in proximity of a fluorescent molecule or dye, there is increase in optical enhancement. This increased optical enhancement results in enhanced fluorescence of fluorescent molecule or dye called as metal enhanced fluorescence [41-44]. The enhancement from emitters can be achieved when there is a coupling or overlap between the excitation wavelength ( $\lambda_{ex}$ ) of the emitter with the SPs transitions. The SP will enhance the local field around the emitter which results in more SP-driven excitation rate [13]. Various metallic structures have been studied and used for fluorescence enhancement by coupling the absorption of emitter with the SPs transition including metallic thin films [45], and metallic nanostructures such as nanocubes [46], nanoholes [47, 48], nanorods [49, 50], nanodisks [51], core-shell nanoparticles [52, 53], DNA-assembled nanoparticles [54], antennas-in-box [55] and nanoantenna [56]. The enhanced and amplified signals have applications in various areas including, biosensing or biodetection [5, 57] with high sensitivity and limit of detection reaching femtomolar of concentration [58, 59].

Absorption/scattering spectra of plasmon-emitter system has been investigated and studied quite well, but on the other hand their emitting properties are still far from being clear. The strong coupling between plasmon and nearby emitter material results in

modification of fluorescence spectra of the emitting material. Plasmon-induced field enhance the fluorescence by manipulating the excitation rate  $\Gamma_{ex}$  and quantum yield  $Q$  of the emitter [60]. Along, with the increase in excitation rate, quantum yield can also be increased by optimizing the balance between radiative and non-radiative rates by adjusting the distance between metal nanostructures and the emitter. Fluorescence wavelength tuning, the emission shift of plasmon-emitter hybrids and modified fluorescence spectra are proportional to  $\chi_A(\lambda) = FL_0(\lambda) \times A(\lambda)$ , where,  $FL_0(\lambda)$  [61, 62] is uncoupled fluorescence spectrum and  $A(\lambda)$  is extinction spectrum of plasmon. While fluorescence enhancement by LSPR in various quantum dots or dyes molecule has been investigated, but data showing fluorescence enhancement using SPP and plasmon coupling still needs to be studied. It would also be interesting to find out the relationship between the enhanced EM field intensity and the fluorescence enhancement. These new findings will help in building the exotic optical property of material with novel applications.

CNDs have attracted very much attention because of their amazing properties like small size, biocompatibility, strong and tunable photoluminescence and good optoelectronics properties [13, 63]. It was reported that fluorescence properties of CNDs is due to the band gap transition[63] but it has not been explored fully yet. A lot of work has been done to improve the fluorescence property of CNDs by changing their structure, functional groups and size. Lately, enhanced field from plasmonic metal was investigated to improve CNDs fluorescence without changing their properties and structure. Some of the recent Studies shows the enhanced fluorescence of CNDs can be achieved using Au

NPs [64-66]. Much of the studies were carried out to enhance the fluorescence using LSPR. A very less data showing the enhanced fluorescence using SPP and plasmon-plasmon coupling. It would also be interesting to understand the underlying mechanism of enhanced fluorescence of CNDs due to plasmonic effect.

In this work we are presenting a system as shown in Figure 3.1, which leads to optical enhancement and eventually the enhanced fluorescence of CNDs immobilized inside the nanoslit with the different size Au NPs. The SPR can enhance or generate the strong EM field around the CNDs which can result in the modulation of the fluorescence properties of the CNDs. Our recently published study shows that SPR enhances the photocurrent generation from photosystem I protein [67] and enhanced fluorescence of CNDs when immobilized in Au nanoslit [13]. Building on these findings, we hereby, presents a new coupled system with Au nanoslit and Au NPs. Our focus is to study how this new coupled system helps in modulating and enhancing the fluorescence properties of CNDs. Here, we fabricated 100 nm width of Au nanoslits array and in the nanoslit array we immobilized CNDs functionalized with different size Au NPs. Then, CNDs functionalized Au NPs hybrid (CNDs-Au) system in the nanoslit and without nanoslit was illuminated with white light source for light intensity and fluorescence measurements. This system will explain how the coupled plasmons (Au nanoslit- Au NPs) enhances the localized and propagating field and enhance the fluorescence of the CNDs. In addition, Finite difference time domain (FDTD) was done for coupled system with difference sizes of Au NPs to optimize the system by calculating the EM field intensity in the coupled system as a function of Au NPs size. We then further assessed

how this particle size variation impacts the fluorescence of CNDs. The mechanism for the fluorescence enhancement of CNDs with coupled system discussed on the basis of plasmon-plasmon and plasmon-exciton coupling.

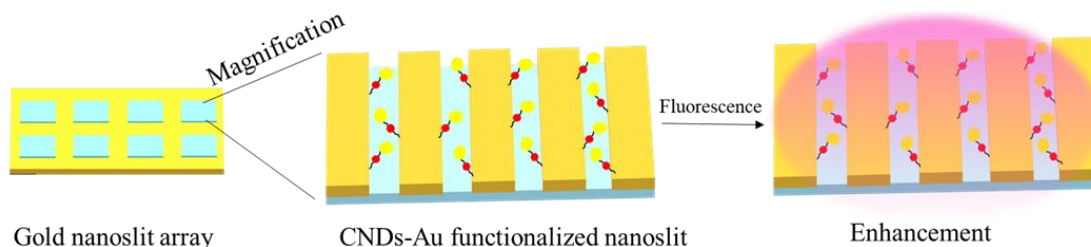


Figure 3.1. Schematic illustration showing the overall design used for fluorescence enhancement of the CNDs.

## Experimental Section

### *Synthesis and Characterization of CNDs*

CNDs were synthesized using Microwave -assisted synthesis procedure reported previously [13, 63, 68]. Citric acid (0.96 g, 99%, ACROS Organics) and ethylenediamine (1mL, 99%, Alfa Aesar) were mixed in 1.0 mL deionized water to form a homogenous solution. Microwave synthesizer (CEM Corp 908005) was used to heat the solution with 300 W for 15 minutes. Further, a dialysis membrane (1000 MWCO, Fisher Scientific) was used against the deionized water to purify the reddish-brown solution for 24 h. To get uniform particle size and remove the larger particles, dialysis water was changed three times. At last, freeze-dryer (FreeZone 6, Labconco) was used to dry the resultant solution for 24 h to obtain the solid sample. Further, the solid sample obtained were characterized by the different techniques. Transmission electron microscopy (TEM) was used to examine the size distribution and uniformity of the purified CNDs. Fourier

transform infrared spectroscopy (670 FTIR, Varian) was done to study functional groups or elemental contents and to know the chemical structure of the CNDs. UV-vis spectroscopy (Cary 6000i, Agilent) was used to know the absorption peak and fluorescence spectroscopy (Cary Eclipse, Agilent) was used to study the emission spectra of the CNDs at different wavelength of light. Both UV-vis and fluorescence spectroscopy techniques gives information about the sample's optical properties. For both UV-Vis and fluorescence spectra, the samples were prepared by dissolving the CNDs in water at a concentration of 0.05 mg/mL.

#### ***Synthesis and Characterization of CNDs-Au hybrid***

Au NPs of different sizes 5 nm, 10 nm and 20 nm were purchased from Ted Pella Inc. The Au NPs were monodispersed, water soluble and citrate stabilized with negative surface charge. The negative surface charge of Au NPs made them easy to conjugate with amine stabilized CNDs (FTIR spectra shows the presence of -NH group on the surface of CNDs). To make CNDs- Au NPs hybrid, the solution having same number of molecules of CNDs and Au NPs was used and stirred at the temp of 80°C for 5 mins. During the reaction, the solution changes color from reddish pink to dark blue which indicates the formation of CNDs-Au hybrid. After 5 mins, a dispersed solution was obtained having CNDs-Au hybrid nanoparticles. Transmission electron microscope (TEM) was used to image the hybrids. Optical properties were studied by UV-vis spectroscopy and fluorescence spectroscopy. For the UV-vis spectra and fluorescence spectra the 0.05 mg/mL concentration of the sample was used.

### ***Fabrication Of device***

Device design as shown in Figure S3.1 with 100 nm of nanoslit array and 600 nm of periodicity was fabricated by E-beam lithography as shown in Figure S3.2. Our previous study shows that 100 nm of nanoslit have the maximum Surface Plasmon Generation (SPG) efficiency[12, 13]. ITO coated glass substrate, 25 x 25 mm, 0.7 mm thick, resistivity < 10  $\Omega$ /sq, TECHINSTRO, product code TIXZ 001 were used for the fabrication. Multi-step cleaning and surface treatment was done. Firstly, ITO coated glass substrate was ultrasonicated and rinsed in acetone, methanol, isopropanol for 15 minutes for each step and blow-dry with nitrogen. Further, substrate was treated with oxygen plasma (e.g. 100 mT, 100 W, 40 sccm O<sub>2</sub>, 4 min, Vision RIE) to make the salinization more effective. Now, the substrate surface becomes hydrophilic. To make the substrate surface hydrophobic, 30 mL ethanol mixed with 150  $\mu$ l of 3-(trimethoxysilyl) propyl methacrylate and submerge the substrates in the prepared ethanol/3-(trimethoxysilyl)propyl methacrylate solution overnight. Rinse the substrate with acetone and distilled/deionized water afterwards. The surface should now be hydrophobic. Hence, the water should run off easily. Blow dry with nitrogen and bake at 90°C for 5 minutes to dry and then cool briefly. For patterning the nanoslit array, spin coat maN-2403 resist with SCS spin coater, step 1: 500 RPM, 1 sec ramp, 5 sec dwell, step 2: 4000 RPM, 3 s ramp, with 60 sec dwells. Further, soft bake at 90° C on hot plate for 1 minute. ELS-G100 100 kV EBL system was used to pattern the substrate with 1 nA beam current, dose varies 184 – 258  $\mu$ C/cm<sup>2</sup> for pattern. After patterning, the Ti/Au was deposited on the pattern using Electron Beam Evaporation Denton Explorer, 40 Å Ti, with the rate of 1.0

Å/sec and 1200 Å Au with the rate of 1.0 Å/sec. The rate was monitored with the help of QCM. Further, the lift off was carried out to get the desired pattern using 1165 (1-methyl-2-pyrrolidinone). Finally, submerge the substrate into 1165 at 70° C, for 1 hour and then ultrasonicate for 15 mins to get 100 nm of nanoslit array with 600 nm of periodicity. The Figure S3.1 (b) and S3.1 (c) shows the optical images of the final device design.

***Preparation of immobilized CNDs- Au NPs into the Au nanoslit array electrode surface***

Firstly, the Au nanoslit array of 100 nm width substrate was cleaned with ethanol, DI water and N<sub>2</sub> dried. Then, it was treated with O<sub>2</sub> plasma (South Bay Technologies PC2000 Plasma Cleaner) for 10 mins to thoroughly clean the surface. For formation of self-assembly monolayer (SAM) formation, 11-mercaptoundecanoic acid (HS(CH<sub>2</sub>)<sub>10</sub>COOH, Sigma Aldrich) and 8-mercapto-octanol (HS(CH<sub>2</sub>)<sub>8</sub>OH, Sigma Aldrich) were used. 11-mercaptoundecanoic acid and 8-mercapto-octanol were dissolved in 1:2 mole ratio, in absolute ethanol and substrate was incubated into this solution for 24 hrs. Once the SAM is formed, then to activate the carboxylic acid groups 1-(3-dimethylaminopropyl)-3-ethylcarbodiimide hydrochloride (EDC, TCI) and N-hydroxysuccinimide (NHS, Sigma Aldrich) were used. Substrate with SAM was put in 0.5 mM solution of EDC and NHS dissolved in water for 2 hours. Then, the substrate was cleaned with DI water and immediately transferred to freshly prepared solution of CNDs-Au hybrid for 2 hours to immobilize the hybrid into the Au nanoslit array. The 0.05 mg/mL concentration of CNDs-Au hybrid was used for the immobilization. Lastly, the substrate was cleaned, dried, and used further for measurements. Note that, for the

fluorescence measurements and light intensity measurements, hybrid solution without nanoslit and hybrid in nanoslit were used.

### ***Finite Difference Time Domain (FDTD) of the Nanoslit array with or without Au NPs***

The EM field intensity profile of the nanoslit array with or without Au NPs was measured by Lumerical FDTD software [69]. The model used for EM field intensity calculation was Au nanoslits array of 100 nm width, 600 nm pitch with different size of Au NPs inside the nanoslits as shown in Figure S3.3. During the simulation, the refractive index of air was assumed 1.0 in the total mesh area. Perfectly matched layer (PML) was applied for the boundary conditions. EM field distribution was calculated for 100 nm width nanoslit array with or without Au NPs using Drude-Lorentz model. Note that 5 nm, 10 nm and 20 nm Au NPs was used during simulation. The transverse electric/magnetic (TE/TM) equation was obtained by Fourier transform of the polarization [70].

### ***Fluorescence imaging and intensity***

Fluorescence measurement for both the system, CNDs-Au NPs hybrid solution and hybrid into the Au nanoslit array were taken. For the measurements, the hybrid solution was drop casted on the glass coverslip and dried overnight. AxioZ2M microscope was used in reflection mode to take the fluorescent measurements. This microscope is the simple optical microscope with different filters like blue, red and green for the fluorescence measurements. Firstly, the images for the substrate were taken using the objective lens and then the filters were used to take the fluorescence images. We used 20X objective lens to capture the image and two filters: 395-440 nm and 450-480 nm were used for fluorescence images. The captured images were changed into the grey scale

images using MATLAB program without changing the intensity. Then, to measure the fluorescence intensity ImageJ software was used.

### ***Reflection Light Intensity Measurement***

CytoViva Hyperspectral Imaging microscope was used to measure the reflected light intensity of different systems. CytoViva Hyperspectral Imaging microscope is the advanced microscope which have both optical imaging and hyperspectral imaging built in same system. For the light intensity measurements, the optical images were taken with 50X objective lens using white light source of wavelength ranging from 400-1000 nm and exposure time of 0.5s. Then those optical images were converted into hyperspectral images using ENVI software which not only gives the pixel by pixel image but also give the intensity spectra corresponding to the image. Hyperspectral imaging technology is specifically known for its capability for spectral characterization and spectral mapping of the samples that too in nanometer range.

## **Results**

### ***CNDs Synthesis and Characterization***

CNDs were synthesized by microwave assisted technique discussed above and then characterized by different techniques. The FTIR spectra as shown in Figure 3.2(a) show broad absorption bands at 3000-3500  $\text{cm}^{-1}$  which corresponds to the stretching vibrations of O-H and N-H and assigned to the carboxylic acid and amine groups, respectively. The bands at 1538, 1432, and 1375  $\text{cm}^{-1}$  of the E-CNDs can be assigned to the bending vibrations of N-H, C-N, and C-H, respectively [71, 72]. The presence of amino, carboxyl and hydroxyl groups on the surface of the CNDs were confirmed by

FTIR, shows the hydrophilic nature of the CNDs, that they are stable in aqueous solution. The Figure 3.3(a) shows the absorption spectra of the CNDs with the absorption band at 350 nm. The Figure 3.2(b) shows fluorescence emission spectra of CNDs taken in DI water (0.05 mg/mL) under different excitation wavelength ( $\lambda_{\text{ex}}$  ranging from 340 to 500 nm). As the wavelength increase there was the red shift in the fluorescence emission of the CNDs. Maximum emission was observed at the 360 nm of excitation wavelength. At the longer wavelength too, they have some emission. TEM image in Figure 3.2(c) confirms the  $\sim 5$  nm of particle size and shows that CNDs particles were monodispersed and spherical in shape.

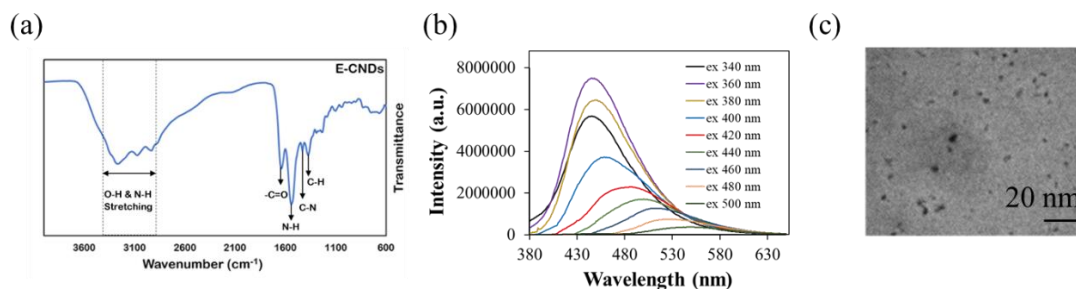


Figure 3.2. Characterization of the CNDs by different techniques (a) FTIR spectra (b) Fluorescence emission spectra (c) TEM image of the CNDs.

### ***CNDs-Au Characterization***

CNDs-Au hybrids were characterized by different techniques. UV-vis in Figure 3.3(a) shows the absorbance band of the hybrid. The CNDs-Au have two absorption band, one is at 350 nm and another broad band around 575 nm confirm the formation of hybrid. Figure S3.4(a) shows the absorption spectra for different size of Au NPs and Figure S3.4(b) shows the absorption spectra for CNDs-Au hybrid with different size of

Au NPs. There was red shift in absorbance spectra with increase in size of Au nanoparticles. Figure 3.3(b) shows the emission spectra of the hybrid for different wavelengths of light. The maximum emission noticed at 400 nm and as the wavelength of light increases there was red shift. Hybrids have emission at longer wavelength of light too as shown in Figure S3.5. Both the UV-vis and emission spectra defines the optical properties of the hybrid. Figure 3.3(c) and (d) shows the TEM images of the CNDs-Au hybrid. TEM images show that particles are bonded together and of size ~15 nm, spherical and uniformly distributed. Note: All the characterization shown in Figure 3.3 were done for CNDs-Au hybrid, used 10 nm of Au NPs.

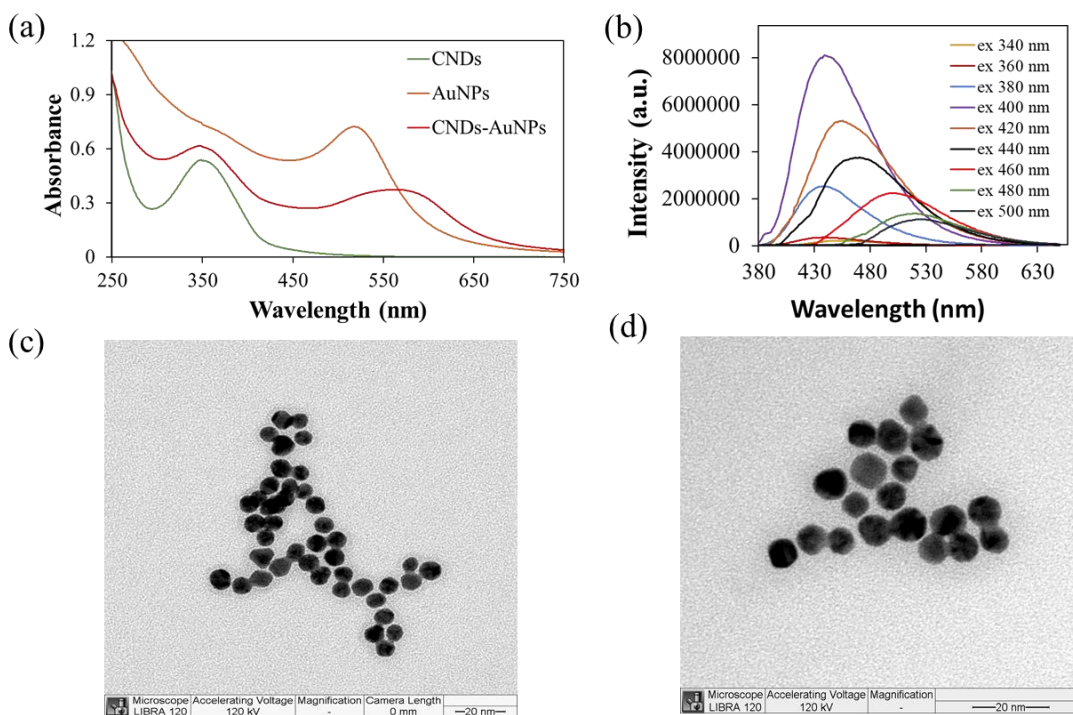


Figure 3.3. Characterization of the CNDs-Au hybrid by different techniques (a) UV-vis spectra (b) Fluorescence emission spectra (c) TEM images of the hybrid showing 1:1 interaction. Note: All characterization in above Figure 3.3 for hybrid was done using 10 nm Au NPs, for all other sizes, data is shown in supplementary information.

### *Au nanoslit array fabrication and immobilization*

Au nanoslit array of 100 nm width fabricated by E-beam lithography. Scanning electron microscopy (SEM) shows the 100 nm width of nanoslit array with 600 nm of periodicity. The array was made onto the 500  $\mu\text{m}$  X 500  $\mu\text{m}$  area of the substrate. SEM images in Figure 3.4(a) and 3.4(b) shows the straight nanoslit array with the constant periodicity of 600 nm between the nanoslits.

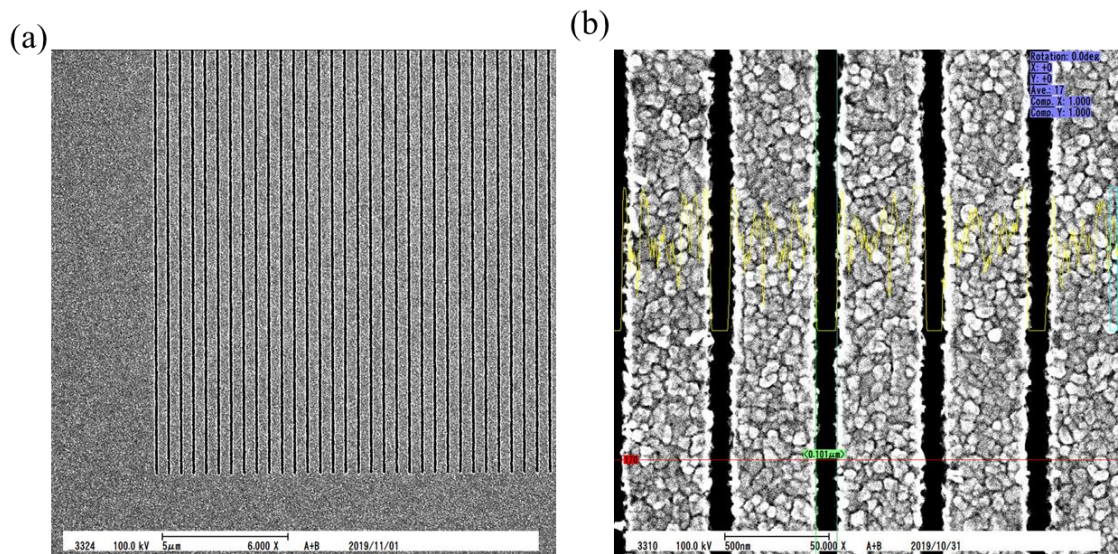


Figure 3.4. SEM images of the 100 nm width of nanoslit array fabricated by E-beam lithography. (a) shows the straight line of 100 nm width, (b) is the enlarged version of the 100 nm width nanoslit array.

Immobilization of CNDs-Au inside the nanoslit array was done using the SAM formation for the fluorescence and light illumination measurements [13]. SAM results in the gap of around 1 nm between the Au nanoslit and CNDs-Au attached to it.

### ***Fluorescence Light intensity and Images***

Fluorescence light intensity were measured by Axio Z2M microscope. Fluorescence images and intensity spectra were taken for CNDs-Au NPs hybrid with different sizes of Au NPs inside the nanoslit and without the nanoslits. For the measurements two filters 395-440 nm and 450-490 nm were used. Once the images were taken with both filters, fluorescence images were converted into grey scale images using MATLAB code without changing the intensity. Then, the intensity was measured using the ImageJ software for each image with the same area. The Figure 3.5 shows the fluorescence light intensity measurement for the CNDs-Au hybrid system for different sizes of Au NPs (5nm, 10nm or 20 nm). The Figure 3.5 shows that the Au NPs without any CNDs have very negligible intensity while there is very slight difference in the fluorescence intensity when different size of Au NPs were used with CNDs. The CNDs shows increased in fluorescence intensity when used with Au NPs in compare when used alone.

Figure S3.6 shows the fluorescence images and Figure 3.5 shows intensity graph when CNDs-Au hybrid used inside the 100 nm width array of nanoslit. The Figure S3.6 (a) shows the fluorescence images and grey scale images taken using 395-440 nm filter, S3.6 (b) shows the fluorescence images and grey scale images taken using 450-490 nm filter and Figure 3.5(a) (b) shows the corresponding intensity. The fluorescence intensity of CNDs-Au hybrid increased when they were placed inside the nanoslit. Nanoslit array did not show any fluorescence without the CNDs or the CNDs-Au hybrid. The difference in fluorescence intensity of CNDs-Au hybrid inside the nanoslit for different size of Au

NPs shows very slight difference, the fluorescence intensity is slightly maximum when 20 nm of Au NPs was used. It was observed that fluorescence intensity was more when 450-490nm excitation wavelength used in compare to 395-440 nm of wavelength. The table S3.1 and S3.2 shows the intensity values calculated for all the images of CNDs-Au hybrid inside the nanoslit and without the nanoslit with the same area for different filters or different excitation light wavelength.

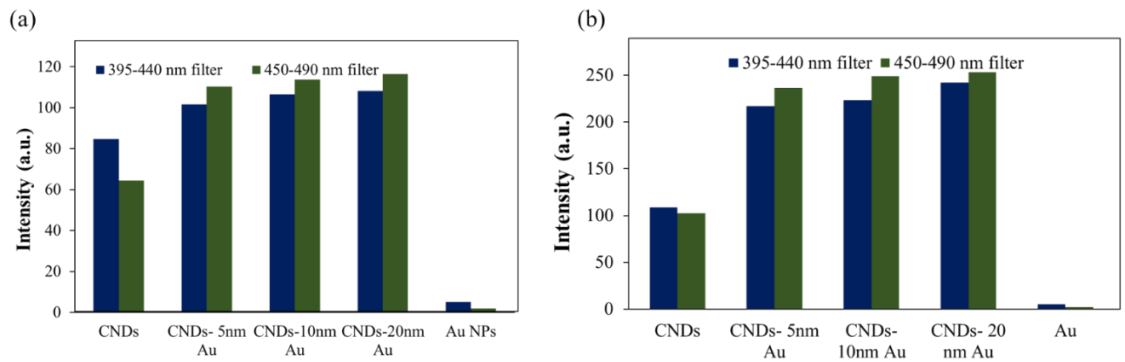


Figure 3.5. Fluorescence intensity spectra. (a) shows the fluorescence intensity spectra for CNDs-Au hybrid with different size of Au NPs without the nanoslit array, (b) graphical plot showing the fluorescence intensity measured with different filters corresponding to different size of Au NPs in CNDs-Au hybrid inside the nanoslit array.

### ***Reflection Light intensity spectra***

The reflective light intensity spectra were taken for the CNDs-Au NPs hybrids inside the nanoslit and without the nanoslit by CytoViva Hyperspectral microscope in the reflection mode. The Figure 3.6(a) shows the reflection light intensity spectra for CNDs-Au NPs hybrid for different size of Au NPs without nanoslit. Figure 3.6(b) shows the light intensity spectra for CNDs-Au NPs hybrid inside the nanoslits. Figure S3.7 and S3.8 shows the normalized light intensity spectrum for the CNDs-Au NPs hybrid inside the

nanoslit and without the nanoslit. Each light intensity spectrum is the average of 9 measurements. The intensity graphs show that reflective light intensity increased when the hybrid CNDs-Au were placed inside the nanoslit. The intensity spectra for the hybrid without nanoslit and inside nanoslit follow the same trend i.e., it is maximum when the CNDs attached to 20 nm of Au NPs and minimum for 5 nm of Au NPs. The difference in intensity is very less but can be seen. The reflection light intensity measurements and fluorescence intensity measurements follow the same trend which can be explained based on coupling of plasmons which enhances the local EM field intensity.

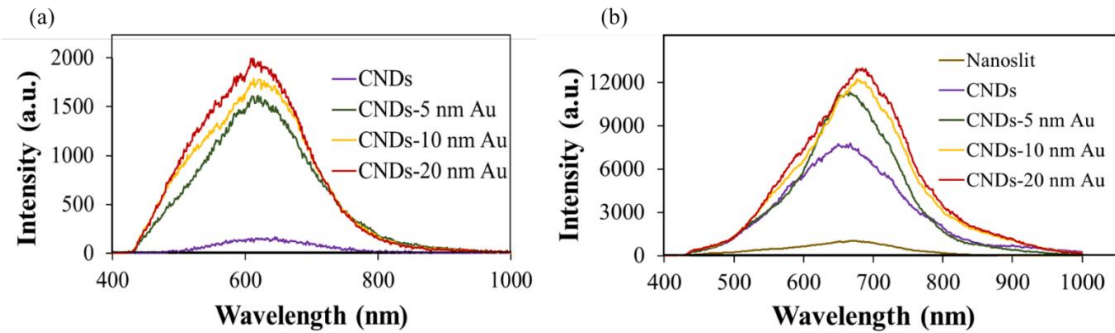


Figure 3.6. Representative net light intensity spectra of CNDs-Au NPs hybrid with different size of Au nanoparticles (a) without nanoslit and (b) inside the nanoslit.

### ***Finite Difference Time Domain (FDTD) of the Nanoslit array with or without Au nanoparticles***

The EM field distribution for 100 nm width nanoslit array with or without Au NPs calculated using FDTD as shown in Figure S3.9. TE/TM equation was obtained for all the models using Fourier transform polarization. The EM field distribution shows the plasmonic intensity at the Au-glass interface which is due to the coupling of Au nanoslit-Au NPs with different size of Au NPs. The trend for the EM distribution for different size

of Au NPs inside the nanoslit is almost the same with slight difference and is as follows:  $EM_{Au20nm} > EM_{Au10nm} > EM_{Au5nm} > EM$ . The FDTD results for all the models were compared with the light intensity spectra and fluorescence intensity. It has been seen that the simulation results agree well with experimental results, which explains that enhanced EM field intensity results in enhance fluorescence.

### **Discussion**

The optical enhancement of CNDs occurs when they were combined with Au NPs and placed inside the nanoslit which is having exposed gold on both the side. The optical enhancement here can be explained by two phenomena: plasmon-plasmon coupling and plasmon-exciton coupling. Plasmon-plasmon coupling between Au nanoslit and Au NPs enhances the optical field intensity which eventually increases the fluorescence of CNDs by plasmon-exciton coupling. It was observed that unlike the single nanostructure, plasmon coupling increases the overlapping field strength with the increase in size of the nanoparticle and with decreasing the distance between them. Less the distance between the nanostructures more will be the intensity of EM field around them [73]. In our study, the distance between the Au NPs and Au nanoslit was constant for different size of Au NPs, the enhanced fluorescence in 20 nm of Au NPs was observed because of its large size which results in more coupling then other size Au NPs. Experimental results for enhanced fluorescence intensity were consistent with the FDTD simulation results and both follow the same trend, maximum for 20 nm of CNDs-Au NPs hybrid in nanoslit and minimum for 5 nm of CNDs-Au NPs hybrid in nanoslit.

Fluorescence signal enhancement for CNDs depend on the intensity of EM field and energy transfer process. Au nanoslit cavities containing CNDs with AuNPs generates both LSPR and SPP, results in SP-induced light trapping/scattering of incident light that leads to plasmon-exciton coupling effect, influencing the fluorescence of CNDs. Moreover, Au NPs and Au nanoslit have plasmon-plasmon coupling too to further enhance the local EM field intensity to enhance the signal intensity.

Plasmon-plasmon coupling between Au nanoslit and Au NPs, can be investigated by simple classical oscillatory model. Both the metallic structures (Au nanoslits and Au NPs) have natural frequency of oscillation corresponding to the plasmons separated by some distance. When these metallic structures are apart (more than 10 nm) they will not interact with each other and keep oscillating with their natural frequencies. Upon external perturbation or external field, Au nanoslit and Au NPs start to oscillate in different direction. They both are in close proximity to each other, so they start affecting each other and modify their oscillation in response to external field. These oscillation interaction increases as the gap between these structures decreases[74]. Here, the gap between Au nanoslit and Au NPs is ~7nm which leads to strong oscillations and enhances the local EM field around CNDs. Few energy-transfer mechanisms were proposed to transfer this enhanced local EM field including Hot electron injection, plasmon-induced resonance energy transfer (PIRET) and light scattering/trapping. Here, because of the interfacial barrier hot electron injection is minimized. PIRET and light trapping/scattering are other efficient energy transfer process between Au nanoslit - CNDs -Au NPs.

Here, two systems were studied: CNDs-Au NPs hybrid placed in between the Au nanoslit cavities and CNDs-Au NPs hybrid without nanoslit as shown in Figure 3.7. Figure 3.7 (a) and (b) illustrates the plasmon-plasmon coupling and plasmon-exciton coupling effect on fluorescence of CNDs. In case of CNDs-Au NPs hybrid immobilized inside the Au nanoslit light trapping, PIRET and plasmon-plasmon coupling plays a major role in fluorescence signal enhancement. , First, the enhanced field by light trapping in Au nanoslit presents overlap with emission and absorption spectrum of CNDs. Second, because of the coupling between plasmons in gold and resonance dipole of CNDs, a resonance energy transfer from metal film and metal nanoparticle to CNDs. Third, plasmon-plasmon coupling between Au NPs and Au nanoslit enhance the local EM field intensity around the CNDs. Light trapping, PIRET and plasmon coupling generates more energetic electrons in conduction band (CB) of CNDs from valence band (VB), resulting in high population of electrons in CB. More number of electrons in CB increases the relaxation per unit time, which results in more and enhanced emission per unit time and contributes to more fluorescence quantum yield

In CND-Au hybrid case, only light trapping and PIRET process involved for signal enhancement, so the local EM field intensity will be less compared to the Au nanoslit-CND-Au NPs system which have plasmon-plasmon coupling too. Both PIRET and light trapping generates energetic electrons in CB, but they will be less compared to above mentioned system, which results in less enhancement of fluorescence.

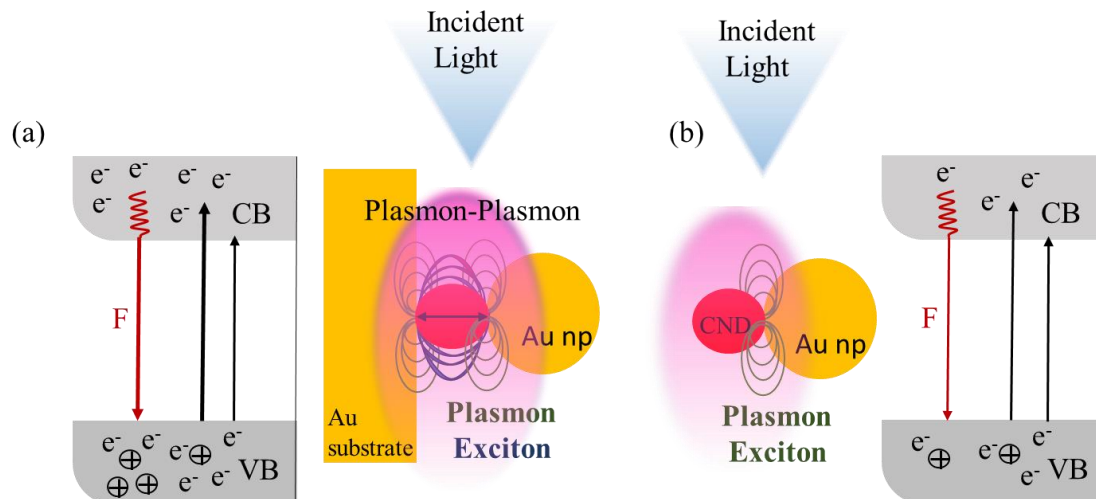


Figure 3.7. Schematic illustration of the mechanism proposed for enhanced fluorescence of CNDs in two systems, (a) CNDs immobilized in between the Au nanoslit Au NPs, (b) CNDs with Au NPs without Au nanoslit.

## Conclusion

In this work, we reported the influence of plasmon-plasmon coupling and plasmon-exciton coupling on the optical enhancement of the CNDs. Here we studied the effect of SPR on fluorescence of two systems, CNDs with Au NPs and CNDs with Au NPs immobilized inside Au nanoslit. The fluorescence intensity is greatly enhanced in both the cases, but it is more when hybrid immobilized inside the nanoslit because of the coupling effect of both the Au NPs and Au nanoslits that have both LSPR and SPP, respectively. 100 nm width of nanoslit array was chosen as it has maximum SPG efficiency. FDTD simulation was done for the different sizes of Au NPs (5nm, 10 nm, and 20 nm) inside the Au nanoslit, to get the EM field intensity. The light intensity spectra show the approx. 4X increased intensity when the hybrid used inside the nanoslits. The results were discussed based on plasmon-plasmon and plasmon-exciton coupling.

Plasmon-plasmon coupling corresponds to enhance EM field and plasmon-exciton coupling leads to exchange of EM fields which results in enhanced excitation and emission rate of CNDs. This study offers a new platform for development of optical devices and optical biosensors.

## REFERENCES

- [1] T. Klar, M. Perner, S. Grosse, G. von Plessen, W. Spirkl, and J. Feldmann, "Surface-Plasmon Resonances in Single Metallic Nanoparticles," *Physical Review Letters*, vol. 80, pp. 4249-4252, 05/11/ 1998.
- [2] V. Amendola, R. Pilot, M. Frasconi, O. M. Maragò, and M. A. Iatì, "Surface plasmon resonance in gold nanoparticles: a review," *Journal of Physics: Condensed Matter*, vol. 29, p. 203002, 2017/04/20 2017.
- [3] M. Xia, P. Zhang, K. Qiao, Y. Bai, and Y.-H. Xie, "Coupling SPP with LSPR for Enhanced Field Confinement: A Simulation Study," *The Journal of Physical Chemistry C*, vol. 120, pp. 527-533, 2016/01/14 2016.
- [4] A. Castro-Grijalba, V. Montes-García, M. J. Cordero-Ferradás, E. Coronado, J. Pérez-Juste, and I. Pastoriza-Santos, "SERS-Based Molecularly Imprinted Plasmonic Sensor for Highly Sensitive PAH Detection," *ACS Sensors*, vol. 5, pp. 693-702, 2020/03/27 2020.
- [5] B. Bagra, T. Mabe, F. Tukur, and J. Wei, "A plasmonic nanoledge array sensor for detection of anti-insulin antibodies of type 1 diabetes biomarker," *Nanotechnology*, vol. 31, p. 325503, 2020/05/28 2020.
- [6] S. Linic, P. Christopher, and D. B. Ingram, "Plasmonic-metal nanostructures for efficient conversion of solar to chemical energy," *Nature Materials*, vol. 10, pp. 911-921, 2011/12/01 2011.
- [7] S. Mukherjee, F. Libisch, N. Large, O. Neumann, L. V. Brown, J. Cheng, *et al.*, "Hot Electrons Do the Impossible: Plasmon-Induced Dissociation of H<sub>2</sub> on Au," *Nano Letters*, vol. 13, pp. 240-247, 2013/01/09 2013.
- [8] M. W. Knight, H. Sobhani, P. Nordlander, and N. J. Halas, "Photodetection with Active Optical Antennas," *Science*, vol. 332, pp. 702-704, 2011.
- [9] W. Cai, A. P. Vasudev, and M. L. Brongersma, "Electrically Controlled Nonlinear Generation of Light with Plasmonics," *Science*, vol. 333, pp. 1720-1723, 2011.
- [10] Q. Gan, F. J. Bartoli, and Z. H. Kafafi, "Plasmonic-Enhanced Organic Photovoltaics: Breaking the 10% Efficiency Barrier," *Advanced Materials*, vol. 25, pp. 2385-2396, 2013.

- [11] N. Liu, F. Wen, Y. Zhao, Y. Wang, P. Nordlander, N. J. Halas, *et al.*, "Individual Nanoantennas Loaded with Three-Dimensional Optical Nanocircuits," *Nano Letters*, vol. 13, pp. 142-147, 2013/01/09 2013.
- [12] Z. Zeng, T. Mabe, W. Zhang, B. Bagra, Z. Ji, Z. Yin, *et al.*, "Plasmon-exciton Coupling in Photosystem I Based Biohybrid Photoelectrochemical Cells," *ACS Applied Bio Materials*, 2018/08/15 2018.
- [13] B. Bagra, W. Zhang, Z. Zeng, T. Mabe, and J. Wei, "Plasmon-Enhanced Fluorescence of Carbon Nanodots in Gold Nanoslit Cavities," *Langmuir*, vol. 35, pp. 8903-8909, 2019/07/09 2019.
- [14] G. Lin and M. Lewandowska, "Plasmon-enhanced fluorescence provided by silver nanoprisms for sensitive detection of sulfide," *Sensors and Actuators B: Chemical*, vol. 292, pp. 241-246, 2019/08/01/ 2019.
- [15] D. Song, R. Yang, C. Wang, R. Xiao, and F. Long, "Reusable nanosilver-coated magnetic particles for ultrasensitive SERS-based detection of malachite green in water samples," *Scientific Reports*, vol. 6, p. 22870, 2016/03/11 2016.
- [16] O. Guselnikova, P. Postnikov, M. Erzina, Y. Kalachyova, V. Švorčík, and O. Lyutakov, "Pretreatment-free selective and reproducible SERS-based detection of heavy metal ions on DTPA functionalized plasmonic platform," *Sensors and Actuators B: Chemical*, vol. 253, pp. 830-838, 2017/12/01/ 2017.
- [17] A. A. Darweesh, S. J. Bauman, and J. B. Herzog, "Improved optical enhancement using double-width plasmonic gratings with nanogaps," *Photonics Research*, vol. 4, pp. 173-180, 2016/10/01 2016.
- [18] X. Chen, C. Ciraci, D. R. Smith, and S.-H. Oh, "Nanogap-Enhanced Infrared Spectroscopy with Template-Stripped Wafer-Scale Arrays of Buried Plasmonic Cavities," *Nano Letters*, vol. 15, pp. 107-113, 2015/01/14 2015.
- [19] C. Lumdee, B. Yun, and P. G. Kik, "Gap-Plasmon Enhanced Gold Nanoparticle Photoluminescence," *ACS Photonics*, vol. 1, pp. 1224-1230, 2014/11/19 2014.
- [20] X. Chen, H.-R. Park, M. Pelton, X. Piao, N. C. Lindquist, H. Im, *et al.*, "Atomic layer lithography of wafer-scale nanogap arrays for extreme confinement of electromagnetic waves," *Nature Communications*, vol. 4, p. 2361, 2013/09/03 2013.
- [21] S. Bauman, D. Debu, A. Hill, E. Novak, D. Natelson, and J. Herzog, *Optical nanogap matrices for plasmonic enhancement applications* vol. 9163: SPIE, 2014.

- [22] D. R. Ward, F. Hüser, F. Pauly, J. C. Cuevas, and D. Natelson, "Optical rectification and field enhancement in a plasmonic nanogap," *Nature Nanotechnology*, vol. 5, pp. 732-736, 2010/10/01 2010.
- [23] H. Im, K. C. Bantz, N. C. Lindquist, C. L. Haynes, and S.-H. Oh, "Vertically Oriented Sub-10-nm Plasmonic Nanogap Arrays," *Nano Letters*, vol. 10, pp. 2231-2236, 2010/06/09 2010.
- [24] T. Kawawaki, Y. Takahashi, and T. Tatsuma, "Enhancement of Dye-Sensitized Photocurrents by Gold Nanoparticles: Effects of Plasmon Coupling," *The Journal of Physical Chemistry C*, vol. 117, pp. 5901-5907, 2013/03/21 2013.
- [25] K. Li, K. Jiang, L. Zhang, Y. Wang, L. Mao, J. Zeng, *et al.*, "Raman scattering enhanced within the plasmonic gap between an isolated Ag triangular nanoplate and Ag film," *Nanotechnology*, vol. 27, p. 165401, 2016/03/04 2016.
- [26] B. Demirdjian, F. Bedu, A. Ranguis, I. Ozerov, and C. R. Henry, "Water Adsorption by a Sensitive Calibrated Gold Plasmonic Nanosensor," *Langmuir*, vol. 34, pp. 5381-5385, 2018/05/15 2018.
- [27] N. H. T. Tran, K. T. L. Trinh, J.-H. Lee, W. J. Yoon, and H. Ju, "Fluorescence Enhancement Using Bimetal Surface Plasmon-Coupled Emission from 5-Carboxyfluorescein (FAM)," *Micromachines*, vol. 9, p. 460, 2018.
- [28] H. Chen, L. Su, M. Jiang, and X. Fang, "Highly Desirable Photodetectors Derived from Versatile Plasmonic Nanostructures," *Advanced Functional Materials*, vol. 27, p. 1704181, 2017.
- [29] P. Ran, L. Jiang, X. Li, B. Li, P. Zuo, and Y. Lu, "Femtosecond Photon-Mediated Plasma Enhances Photosynthesis of Plasmonic Nanostructures and Their SERS Applications," *Small*, vol. 15, p. 1804899, 2019.
- [30] M. Zhang, X. Zhong, W. Zheng, S. Ruan, B. Du, P. Yan, *et al.*, "Widely tunable, high optical signal-to-noise ratio erbium-doped photonic crystal fiber laser suitable for acetylene sensing," *Optics & Laser Technology*, vol. 109, pp. 525-533, 2019/01/01/ 2019.
- [31] X. Yang, Y. Lu, B. Liu, and J. Yao, "Fiber Ring Laser Temperature Sensor Based on Liquid-Filled Photonic Crystal Fiber," *IEEE Sensors Journal*, vol. 17, pp. 6948-6952, 2017.
- [32] P. Chaturvedi, S. D. Rodriguez, I. Vlassioux, I. A. Hansen, and S. N. Smirnov, "Simple and Versatile Detection of Viruses Using Anodized Alumina Membranes," *ACS Sensors*, vol. 1, pp. 488-492, 2016/05/27 2016.

- [33] J.-j. Zhu, X. Meng, C. Zhang, J. Bian, Z. Lu, Y. Liu, *et al.*, "Tailoring a nanostructured plasmonic absorber for high efficiency surface-assisted laser desorption/ionization," *Physical Chemistry Chemical Physics*, vol. 20, pp. 3424-3429, 2018.
- [34] S. Arshavsky-Graham, N. Massad-Ivanir, E. Segal, and S. Weiss, "Porous Silicon-Based Photonic Biosensors: Current Status and Emerging Applications," *Analytical Chemistry*, vol. 91, pp. 441-467, 2019/01/02 2019.
- [35] S. Gao, W. Cen, Q. Li, J. Li, Y. Lu, H. Wang, *et al.*, "A mild one-step method for enhancing optical absorption of amine-functionalized metal-organic frameworks," *Applied Catalysis B: Environmental*, vol. 227, pp. 190-197, 2018/07/05/ 2018.
- [36] J. Wirth, K. K. Green, M. O'Connor, and S. F. Lim, "Enhancement of Upconverted Fluorescence by Interference Layers," *Small*, vol. 13, p. 1602846, 2017.
- [37] A. López-Ortega, M. Takahashi, S. Maenosono, and P. Vavassori, "Plasmon induced magneto-optical enhancement in metallic Ag/FeCo core/shell nanoparticles synthesized by colloidal chemistry," *Nanoscale*, vol. 10, pp. 18672-18679, 2018.
- [38] B. L. Darby, B. Auguié, M. Meyer, A. E. Pantoja, and E. C. Le Ru, "Modified optical absorption of molecules on metallic nanoparticles at sub-monolayer coverage," *Nature Photonics*, vol. 10, pp. 40-45, 2016/01/01 2016.
- [39] N. Nwaji, J. Mack, and T. Nyokong, "Enhanced nonlinear optical response of benzothiazole substituted ball-type phthalocyanines in the presence of metallic nanoparticles," *Optical Materials*, vol. 82, pp. 93-103, 2018/08/01/ 2018.
- [40] E. Klantsataya, A. François, H. Ebendorff-Heidepriem, B. Sciacca, A. Zuber, and T. M. Monro, "Effect of surface roughness on metal enhanced fluorescence in planar substrates and optical fibers," *Optical Materials Express*, vol. 6, pp. 2128-2138, 2016/06/01 2016.
- [41] Y. Jeong, Y.-M. Kook, K. Lee, and W.-G. Koh, "Metal enhanced fluorescence (MEF) for biosensors: General approaches and a review of recent developments," *Biosensors and Bioelectronics*, vol. 111, pp. 102-116, 2018/07/15/ 2018.
- [42] S. M. Fothergill, C. Joyce, and F. Xie, "Metal enhanced fluorescence biosensing: from ultra-violet towards second near-infrared window," *Nanoscale*, vol. 10, pp. 20914-20929, 2018.
- [43] M. Zheng, Y. Kang, D. Liu, C. Li, B. Zheng, and H. Tang, "Detection of ATP from "fluorescence" to "enhanced fluorescence" based on metal-enhanced fluorescence triggered by aptamer nanoswitch," *Sensors and Actuators B: Chemical*, vol. 319, p. 128263, 2020/09/15/ 2020.

- [44] D.-D. Xu, C. Liu, C.-Y. Li, C.-Y. Song, Y.-F. Kang, C.-B. Qi, *et al.*, "Dual Amplification Fluorescence Assay for Alpha Fetal Protein Utilizing Immunohybridization Chain Reaction and Metal-Enhanced Fluorescence of Carbon Nanodots," *ACS Applied Materials & Interfaces*, vol. 9, pp. 37606-37614, 2017/11/01 2017.
- [45] J. Lee, J. Song, D. Lee, and Y. Pang, "Metal-enhanced fluorescence and excited state dynamics of carotenoids in thin polymer films," *Scientific Reports*, vol. 9, p. 3551, 2019/03/05 2019.
- [46] G. M. Akselrod, C. Argyropoulos, T. B. Hoang, C. Ciraci, C. Fang, J. Huang, *et al.*, "Probing the mechanisms of large Purcell enhancement in plasmonic nanoantennas," *Nature Photonics*, vol. 8, pp. 835-840, 2014/11/01 2014.
- [47] Q. Zhang, L. Wu, T. I. Wong, J. Zhang, X. Liu, X. Zhou, *et al.*, "Surface plasmon-enhanced fluorescence on Au nanohole array for prostate-specific antigen detection," *International journal of nanomedicine*, vol. 12, pp. 2307-2314, 2017.
- [48] V. E. Bochenkov, A. M. Shakhov, A. A. Astafiev, and V. A. Timoshenko, "Immobilization and plasmon-enhanced fluorescence of EGFP on Al nanohole arrays," *Journal of Physics: Conference Series*, vol. 1461, p. 012016, 2020/03 2020.
- [49] M. A. Badshah, J. Ju, X. Lu, N. Abbas, and S.-m. Kim, "Enhancing the sensitivity of DNA microarrays by metal-enhanced fluorescence using vertical nanorod structures," *Sensors and Actuators B: Chemical*, vol. 274, pp. 451-457, 2018/11/20/ 2018.
- [50] J. Sun, Z. Li, Y. Sun, L. Zhong, J. Huang, J. Zhang, *et al.*, "Uniform and reproducible plasmon-enhanced fluorescence substrate based on PMMA-coated, large-area Au@Ag nanorod arrays," *Nano Research*, vol. 11, pp. 953-965, 2018/02/01 2018.
- [51] M. Bauch and J. Dostalek, "Collective localized surface plasmons for high performance fluorescence biosensing," *Optics Express*, vol. 21, pp. 20470-20483, 2013/08/26 2013.
- [52] R. Bardhan, N. K. Grady, J. R. Cole, A. Joshi, and N. J. Halas, "Fluorescence Enhancement by Au Nanostructures: Nanoshells and Nanorods," *ACS Nano*, vol. 3, pp. 744-752, 2009/03/24 2009.
- [53] K. Sugawa, T. Tamura, H. Tahara, D. Yamaguchi, T. Akiyama, J. Otsuki, *et al.*, "Metal-Enhanced Fluorescence Platforms Based on Plasmonic Ordered Copper Arrays: Wavelength Dependence of Quenching and Enhancement Effects," *ACS Nano*, vol. 7, pp. 9997-10010, 2013/11/26 2013.

- [54] G. P. Acuna, F. M. Möller, P. Holzmeister, S. Beater, B. Lalkens, and P. Tinnefeld, "Fluorescence Enhancement at Docking Sites of DNA-Directed Self-Assembled Nanoantennas," *Science*, vol. 338, pp. 506-510, 2012.
- [55] D. Punj, M. Mivelle, S. B. Moparthy, T. S. van Zanten, H. Rigneault, N. F. van Hulst, *et al.*, "A plasmonic 'antenna-in-box' platform for enhanced single-molecule analysis at micromolar concentrations," *Nature Nanotechnology*, vol. 8, pp. 512-516, 2013/07/01 2013.
- [56] S. Sun, T. Zhang, Q. Liu, L. Ma, Q. Du, and H. Duan, "Enhanced Directional Fluorescence Emission of Randomly Oriented Emitters via a Metal–Dielectric Hybrid Nanoantenna," *The Journal of Physical Chemistry C*, vol. 123, pp. 21150-21160, 2019/08/29 2019.
- [57] M. Sanders, Y. Lin, J. Wei, T. Bono, and R. G. Lindquist, "An enhanced LSPR fiber-optic nanoprobe for ultrasensitive detection of protein biomarkers," *Biosensors and Bioelectronics*, vol. 61, pp. 95-101, 2014/11/15/ 2014.
- [58] F. Fathi, M.-R. Rashidi, and Y. Omid, "Ultra-sensitive detection by metal nanoparticles-mediated enhanced SPR biosensors," *Talanta*, vol. 192, pp. 118-127, 2019/01/15/ 2019.
- [59] J. Huang, Y. Zhang, Z. Lin, W. Liu, X. Chen, Y. Liu, *et al.*, "Femtomolar detection of nucleic acid based on functionalized gold nanoparticles," in *Nanophotonics* vol. 8, ed, 2019, p. 1495.
- [60] R. Liu, Z.-K. Zhou, Y.-C. Yu, T. Zhang, H. Wang, G. Liu, *et al.*, "Strong Light-Matter Interactions in Single Open Plasmonic Nanocavities at the Quantum Optics Limit," *Physical Review Letters*, vol. 118, p. 237401, 06/08/ 2017.
- [61] M. Fang, Z. Huang, T. Koschny, and C. M. Soukoulis, "Electrodynamic Modeling of Quantum Dot Luminescence in Plasmonic Metamaterials," *ACS Photonics*, vol. 3, pp. 558-563, 2016/04/20 2016.
- [62] X. Li, L. Zhou, Z. Hao, and Q.-Q. Wang, "Plasmon–Exciton Coupling in Complex Systems," *Advanced Optical Materials*, vol. 6, p. 1800275, 2018.
- [63] Z. Zeng, W. Zhang, D. M. Arvapalli, B. Bloom, A. Sheardy, T. Mabe, *et al.*, "A fluorescence-electrochemical study of carbon nanodots (CNDs) in bio- and photoelectronic applications and energy gap investigation," *Physical Chemistry Chemical Physics*, vol. 19, pp. 20101-20109, 2017.
- [64] J. Jana, T. Aditya, M. Ganguly, S. K. Mehetor, and T. Pal, "Fluorescence enhancement via varied long-chain thiol stabilized gold nanoparticles: A study of far-

field effect," *Spectrochimica Acta Part A: Molecular and Biomolecular Spectroscopy*, vol. 188, pp. 551-560, 2018/01/05/ 2018.

[65] I. Matai, A. Sachdev, and P. Gopinath, "Self-Assembled Hybrids of Fluorescent Carbon Dots and PAMAM Dendrimers for Epirubicin Delivery and Intracellular Imaging," *ACS Applied Materials & Interfaces*, vol. 7, pp. 11423-11435, 2015/06/03 2015.

[66] Y. Zhang, J. Zhang, J. Zhang, S. Lin, Y. Huang, R. Yuan, *et al.*, "Intense enhancement of yellow luminescent carbon dots coupled with gold nanoparticles toward white LED," *Dyes and Pigments*, vol. 140, pp. 122-130, 2017/05/01/ 2017.

[67] Z. Zeng, T. Mabe, W. Zhang, B. Bagra, Z. Ji, Z. Yin, *et al.*, "Plasmon–Exciton Coupling in Photosystem I Based Biohybrid Photoelectrochemical Cells," *ACS Applied Bio Materials*, vol. 1, pp. 802-807, 2018/09/17 2018.

[68] W. Zhang, Z. Zeng, and J. Wei, "Electrochemical Study of DPPH Radical Scavenging for Evaluating the Antioxidant Capacity of Carbon Nanodots," *The Journal of Physical Chemistry C*, vol. 121, pp. 18635-18642, 2017/08/31 2017.

[69] Z. Zeng, M. N. Mendis, D. H. Waldeck, and J. Wei, "A semi-analytical decomposition analysis of surface plasmon generation and the optimal nanoledge plasmonic device," *RSC Advances*, vol. 6, pp. 17196-17203, 2016.

[70] Z. Zeng, Y. Liu, and J. Wei, "Recent advances in surface-enhanced raman spectroscopy (SERS): Finite-difference time-domain (FDTD) method for SERS and sensing applications," *TrAC Trends in Analytical Chemistry*, vol. 75, pp. 162-173, 2016/01/01/ 2016.

[71] D. M. Arvapalli, A. T. Sheardy, K. C. Alapati, and J. Wei, "High Quantum Yield Fluorescent Carbon Nanodots for detection of Fe (III) Ions and Electrochemical Study of Quenching Mechanism," *Talanta*, vol. 209, p. 120538, 2020/03/01/ 2020.

[72] W. Li, Z. Zhang, B. Kong, S. Feng, J. Wang, L. Wang, *et al.*, "Simple and Green Synthesis of Nitrogen-Doped Photoluminescent Carbonaceous Nanospheres for Bioimaging," *Angewandte Chemie International Edition*, vol. 52, pp. 8151-8155, 2013.

[73] C. Tabor, R. Murali, M. Mahmoud, and M. A. El-Sayed, "On the Use of Plasmonic Nanoparticle Pairs As a Plasmon Ruler: The Dependence of the Near-Field Dipole Plasmon Coupling on Nanoparticle Size and Shape," *The Journal of Physical Chemistry A*, vol. 113, pp. 1946-1953, 2009/03/12 2009.

[74] A. Hazra, S. M. Hossain, A. K. Pramanick, and M. Ray, "Gold-silver nanostructures: Plasmon-plasmon interaction," *Vacuum*, vol. 146, pp. 437-443, 2017/12/01/ 2017.

## **CHAPTER IV**

### **PLASMON ENHANCED PERFORMANCE OF CARBON NANODOTS BASED PHOTOELECTROCHEMICAL CELL USING GOLD NANOSLIT CAVITIES**

#### **Overview**

Plasmonic nanostructures have the property of light manipulation at the sub-wavelength scale which has been utilized to improve/enhance the efficiency of the photoelectrochemical cell. The device performance is measured by its ability to absorb light and light conversion ability. Incorporation of the Plasmonic metallic nanostructures boost both these properties by concentrating the light into active region. In this perspective, we developed a new device design where we fabricated gold nanoslit electrode and immobilize the electrode with Carbon nanodots (CNDs) and titanium dioxide (TiO<sub>2</sub>) nanoparticles to evaluate the photocurrent generation efficiency. This current model provides a framework for the performance enhancement of the photoelectrochemical cells when plasmonic nanostructures used with active materials. Furthermore, intersection between Plasmonics and photovoltaics offers an outlook on the future high efficiency solar cells.

#### **Introduction**

Sunlight is one of the abundant natural resources and can be used to meet the requirements of the future energy needs. Use of solar energy to fabricate photoelectrochemical cell has the potential to overcome the energy crisis, environmental

problems and to make a great contribution in the large portion of energy. Recently, the use of solar energy for photoelectrochemical cell fabrication has attracted a lot of attention due to its better energy conversion efficiency and low fabrication cost. Most of the research carried out to replace the traditional organic dyes with the nanostructures to improve the Power conversion efficiencies (PCE). Recently, above 22% of PCE was reported in last seven years from 2009 when nanostructures used as sensitizers in device designing [1-4]. The most important key factor that determine the performance of any photoelectrochemical cell is its capability to absorb the light and its capability to extract the generated charge carriers [5]. Light absorption or trapping can be enhanced by engineering the device designing and fabrication process. Number of promising approaches has been identified to enhance the light absorption [6-11], among them, one of the approaches is to use plasmonic nanostructures in the device. Plasmonic nanostructures have Localized Surface Plasmons or propagating surface plasmons, that can couple with incident photons, resulting into confinement of the electromagnetic (EM) field. This localized EM field maximize the absorption of incident light and improved the efficiency [12-14]. Other key factor to improve performance and cost reduction of the photovoltaic device performance is efficient light management by minimize the reflection and scattering of the upcoming light and to enhance the optical absorption [15, 16]. Use of nanostructure with graded refractive index [17-20] and plasmonic structures and layers [21-25] can be used as antireflection coatings which offer great potential for light absorption enhancement [9]. Plasmonics structure offers a most promising and significant potential application [26], in the field of the photovoltaics [27-30]. Many

scientists used and proposed different designing and different technologies to use plasmon excitation and light localization with surface plasmon resonance (SPR) for the high and improved efficiency. Plasmonic nanostructures can be used in at least three different configurations in the photovoltaic device as shown in Figure 4.1 : on the surface of the device to capture incident light [31-34], embedded inside the active layer of the semiconductor to provide more light to the semiconductor by localized surface plasmon resonance (LSPR) [35-38] or at the bottom, interface between the semiconductor and the metal in the form of scattering nanoparticles [39, 40] or as surface plasmonic gratings [41-44]. In each case the increase in efficiency is due to the different physical principle involved. When the plasmonic nanostructure is at the surface as shown in Figure 4.1 (a), more light is captured and trapped by the semiconductor due to multiple and high angle scattering, which results in increase in optical path length inside the device. When the plasmonic nanostructures embedded inside the active layer as shown in Figure 4.1 (b), there is a strong localization and enhancement of the light within the proximity of the semiconductor which results in more or additional generation of electron-hole pair within the device. In the last device design as shown in Figure 4.1(c) and (d) the use of metal gratings with periodic nanostructures array can be coupled with the light and results in surface plasmon polaritons (SPP), which propagate in the plane of the semiconductor layer and generate more electron-hole pairs [5].

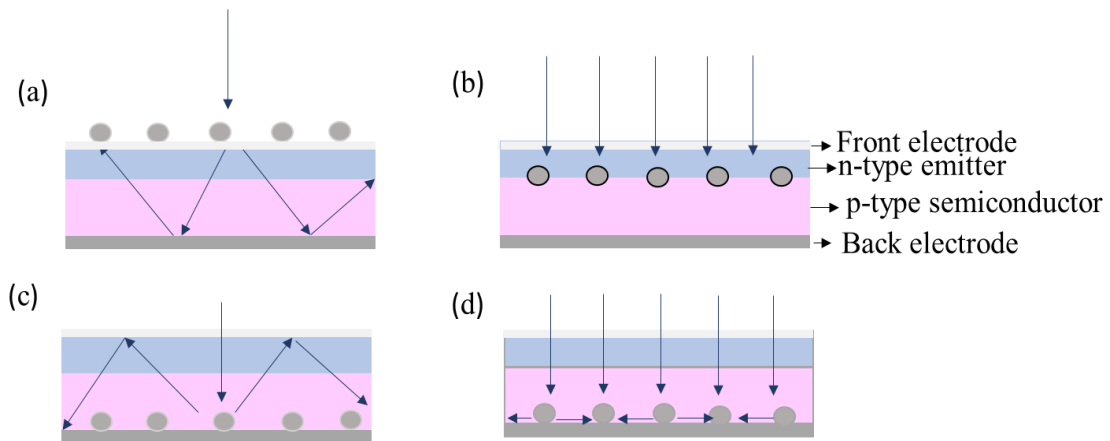


Figure 4.1. Light trapping or absorption by plasmonic nanostructures in device structure when used in different configurations (a) on the surface, (b) inside the active layer, or (c) and (d) as periodic arrays at metal-semiconductor interface.

Many studies have been carried out where researchers used  $\text{TiO}_2$  or  $\text{ZnO}$  nanostructures with low band gap semiconductor Quantum dots (QDs) such as  $\text{CdS}$ ,  $\text{CdSe}$ ,  $\text{PbS}$ ,  $\text{PbSe}$  etc[45-47] to increase the efficiency of the photoelectrochemical cell. But recently, graphene quantum dots (GQDs), carbon quantum dots (CQDs) and carbon nanodots (CNDs) received much more attention due to their amazing properties. These particles have small size and their optical properties like absorption and emission can be tuned with the size [48]. CNDs or CQDs have received extensive attention because they are spherical shape with less than 10 nm of size, and have amazing properties like photoluminescent (PL), easy preparation, cost effective synthesis, tunable PL properties [49]. More importantly they are biocompatible and nontoxic for the environment and the biological system which is very advantageous. Few of the research work where scientist used CQDs or CNDs in their design to improve the PCE. Mirtchev et al. observed the PCE of 0.13% when they used  $\text{TiO}_2$  photoanode with CQDs which is synthesized by

using acid dehydration of  $\gamma$ -butyrolactone [50]. Like Mirtchev et al., Zhang et al. reported the same PCE that is 0.13% by fabricating photoelectrochemical cell using N-doped CQDs as photosensitizers [51]. Briscoe et al. synthesized the three different types of biomass-derived CQDs and used them as photosensitizers. He used these photosensitizers with ZnO as photoanodes and observed the PCE of 0.077% [52]. Recently, Margraf et al. reported the PCE of 0.24% where he used CQD in their device design [53]. Wang et al. also construct the photoelectrochemical cell with CQD by integrating CQDs and TiO<sub>2</sub> photoanodes in acetone and a PCE of 0.79% was obtained [54]. Zhang et al. fabricated the device using hybridized CQDs/TiO<sub>2</sub> as photoanode and observed the improved PCE of 0.87%, which is higher than all of the reported CQD cells adopting the simple post-adsorption method [55].

Considering the above studies shows that, use of CQDs or CNDs in photoelectrochemical cell to increase PCE has been investigated, but the research of the plasmonic effect on the CNDs to increase PCE is very rare and needs to be explored. Considering that, here, in this work we are presenting a plasmonically enhanced photoelectrochemical device with nanoslit design. Optimized 100 nm of nanoslit design immobilized with CNDs and TiO<sub>2</sub> nanoparticles was used as a working electrode. Here, we investigated the enhanced electron transfer interaction between CNDs, TiO<sub>2</sub> and gold electrode due to plasmonic effect. The efficiency and fill factor were measured for the plasmonic device design in light and dark condition. The results will offer a new way to develop the photovoltaic device for enhancing the efficiency and photocurrent generation using the plasmonic nanostructures.

## Experimental Section

### *Fabrication of device*

We used simple photolithography technique with FIB for the fabrication of device as shown in fig 4.3. A high resolution transparent dark -field photomask was developed by AutoCAD using 25400 DPI printer as shown in Figure 4.2.

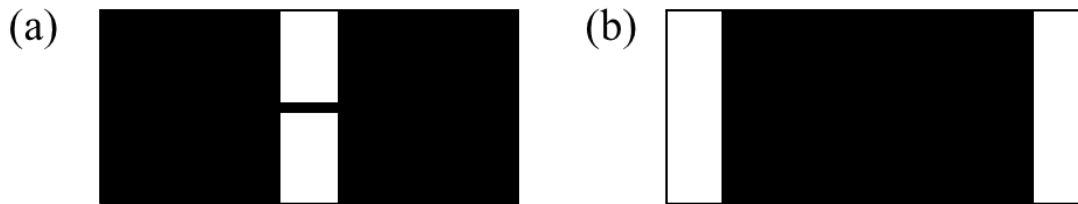


Figure 4.2. Dark field mask prepared by AutoCAD used during photolithography for the fabrication of device, (a) is the mask used for first step of lithography, (b) showing the mask used for second step of lithography.

Globe diamond white glass slide were used as substrates. Glass substrates were first treated with piranha solution, then cleaned with DI water and N<sub>2</sub> dried. Further substrates were exposed to oxygen plasma at 200 W, for 2 min for proper cleaning and then they were dehydrated on hot plate at 180°C. JSR NFR 016 D2 negative photoresist was spin applied on the cleaned substrates with the thickness of 3.5 μm, and then soft baked on hot plate for 90s at 90°C. After that, they were exposed for 6s by OAI mask aligner for the patterning and post baked at 90°C for 90s. Then, the resist was developed in PD523AD for 60s at room temperature. At each process steps, microscopy images and profilometry measurements were taken. Once patterned was developed all the substrate moved for metal deposition to evaporation chamber (Kurt Lesker PVD 75 e-beam evaporator). Ti/Au/Ti/SiO<sub>2</sub> was deposited on the patterned surface once the base pressure

of evaporator reached to  $2.7 \times 10^{-6}$ . 4.4 nm thickness of Ti was deposited at the rate of 0.5 Å/s, 225.4 nm of Au was deposited at the rate of 3.5 Å/s, 4.6 nm of Ti was deposited at the rate of 0.4 Å/s and the 26.7 nm SiO<sub>2</sub> was deposited at the rate of 1.5 Å/s. Ti was used as adhesive layer and SiO<sub>2</sub> was used as a capping layer to protect the device from wear and tear. Once the metal deposition was done, then we did the lift-off of the metal using acetone bath with sonication for 5 mins. To make the electrodes on the device, second lithography step was performed. For the second photolithography step, photoresist Shipley1827 with HMDS was spin coated on the patterned device and exposed to the second photomask for 26s using OAI mask aligner. Next step was to etch the SiO<sub>2</sub> capping layer with the reactive ion etching tool (LAM Rainbow 4400). CF<sub>4</sub> at 45 sccm and O<sub>2</sub> were used at 5 sccm were used at 40mT of etch pressure to etch. Afterwards, the positive resist S1827 was stripped using 1165 to make the pattern on the device. A 100 nm width of nanoslit was milled at the center of each device with focused ion beam milling (Zeiss Auriga) to get the final device.

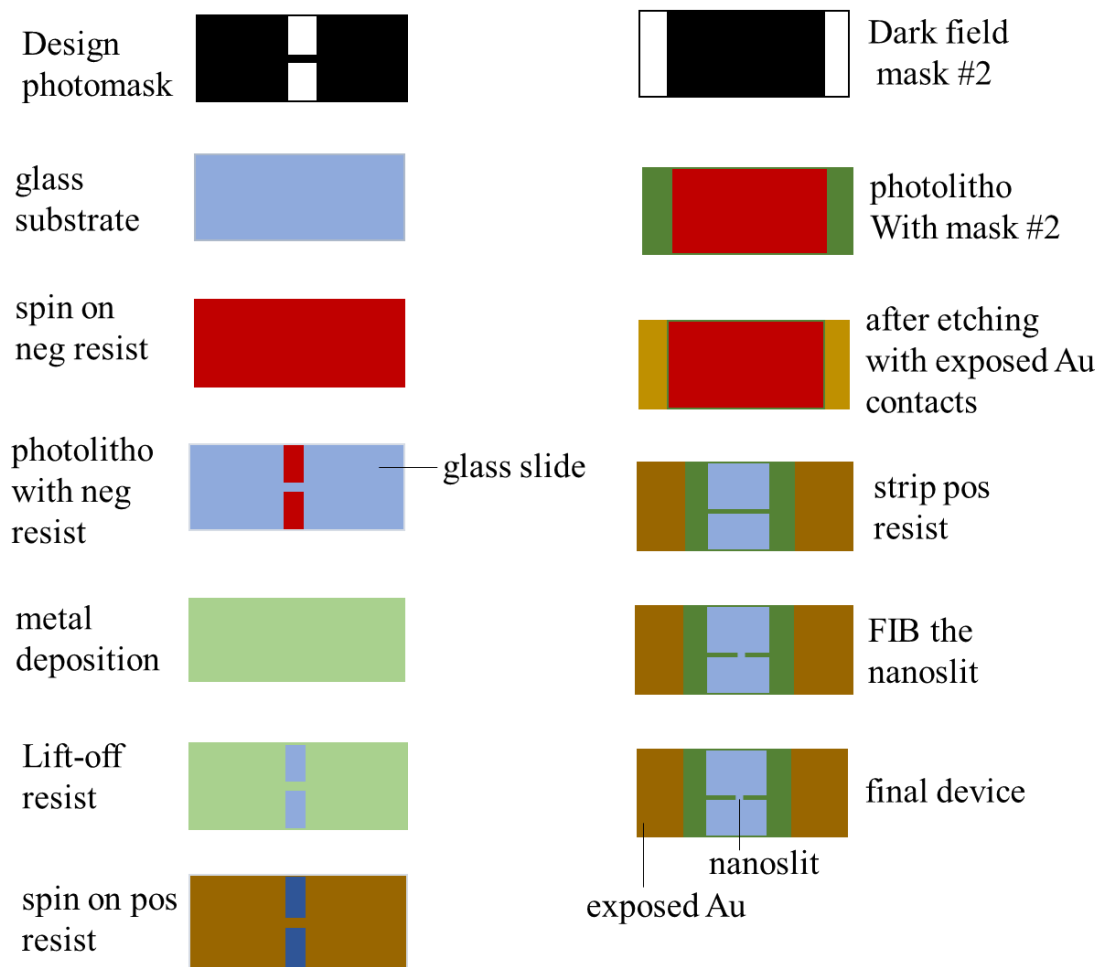


Figure 4.3. Illustration of the approach used for fabrication of the gold electrode device.

***Self-assembly monolayer formation***

The self-assembly monolayer (SAM) was formed on the gold electrode surface for its functionalization using the same method previously reported by our lab group as shown in Figure 4.4 [56].

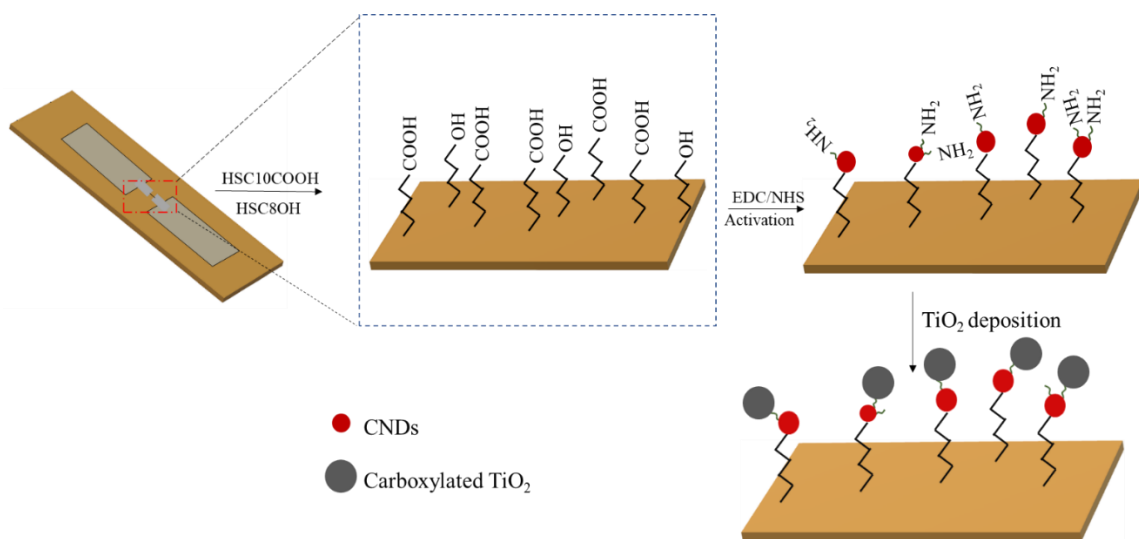


Figure 4.4. Schematic representation of the steps used for functionalization of the gold electrode surface.

Firstly, the fabricated Gold electrode with 100 nm nanoslit width was cleaned with O<sub>2</sub> plasma (South Bay Technologies PC2000 Plasma Cleaner) for 10 min. Then, the mixture of 11-mercaptoundecanoic acid (HS(CH<sub>2</sub>)<sub>10</sub>COOH, Sigma-Aldrich) and 8-mercapto-octanol (HS(CH<sub>2</sub>)<sub>8</sub>OH, Sigma-Aldrich) in an absolute ethanol solution (Acros Organics) was used to form a self-assembled monolayer (SAM). After SAM formation, the solution of 0.5 mM 1-(3-dimethylaminopropyl)-3-ethylcarbodiimide hydrochloride (TCI)/N-hydroxysuccinimide (Sigma-Aldrich) was used to activate the carboxylic acid groups formed by SAM. Once, the carboxylic acid groups activated then the freshly prepared 0.05 mg/mL concentration of CNDs solution was used to bind with the functionalized gold electrode surface. Then, the electrode surface was rinsed with DI water and dried and prepared for further functionalization. Meanwhile, a TiO<sub>2</sub> citrate solution was prepared to functionalize the TiO<sub>2</sub> surface with the carboxylic groups so that it can bind with the amine groups of the CNDs. After that, the gold electrodes were

moved to freshly prepared 10 nm size, 0.05 mg/mL of TiO<sub>2</sub> solution for 2h. During this surface chemistry, the TiO<sub>2</sub> bonded to CNs surface which was already attached to the gold electrode surface. Further, the functionalized electrode was washed with DI water, N<sub>2</sub> dried before the experiment. After each step of functionalization, the light intensity measurements on the electrode surface were carried out using CytoViva microscope in reflection mode. The Figure 4.5 shows the shift in the peak and decrease in intensity after each step of functionalization which indicates successful functionalization of the device surface.

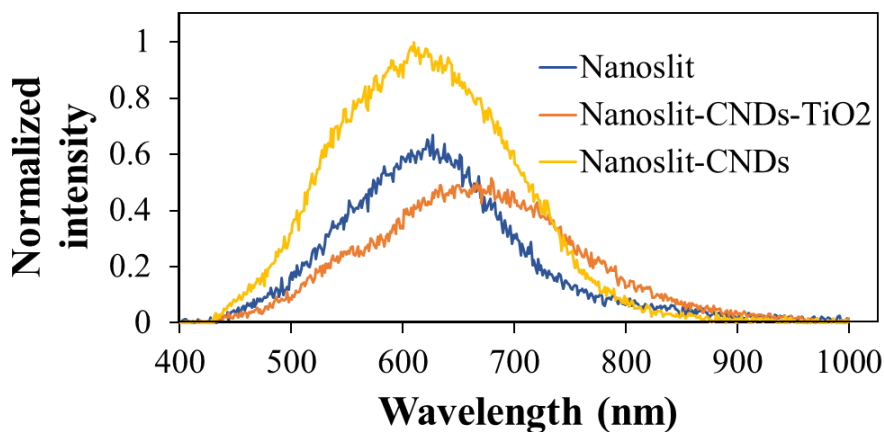


Figure 4.5. Light intensity spectra showing shift in peak and decrease in light intensity after each step of functionalization.

### ***Photovoltaic Measurements***

For the photovoltaic measurements, we have the photoelectrochemical cell having gold nanoslit electrode functionalized with CNs and TiO<sub>2</sub> nanoparticle. Photovoltaic measurements (i-v/p-v curve) were conducted using 4- probe Photo Emission Tech Inc- Solar Cell IV measurement solar simulator with power of 1000 W/m<sup>2</sup>. The functionalized

gold electrode was immersed into the methylene blue (MB) redox-active mediator with 100 mM KCl and 10 mM PBS electrolyte solution. Both side of the functionalized electrode was electrically connected through a piece of copper tape for the connection to the solar simulator. The concentration of MB was varied from 5mM to 30 mM (5mM, 10mM, 15mM, 20mM, 25 mM and 30mM). The i-v and p-v curves were measured for different concentration of MB in dark and light condition. For control, two measurements were recorded: plain gold electrode without nanoslit was functionalized with CNDs and TiO<sub>2</sub> and other was gold nanoslit electrode functionalized with only TiO<sub>2</sub> nanoparticles.

## **Results**

The Figure 4.6 (a-f) shows the i-v curve for different concentration of MB in light and dark conditions. The table 4.1-4.3 shows the different parameters and efficiency measured for working electrode with different concentration of MB. Table 4.2 and table 4.3 shows the data for the functionalized gold electrode in presence of light and dark, respectively. All the variables calculated for the control in presence of light shown in table 4.3. While calculating the efficiency, current density was used with active area of 0.004 m<sup>2</sup> (fabrication information). We found that 20 mM of the MB have the maximum efficiency with 4.07%. For the 20 mM MB the number of electron acceptor and electron donor balance each other which result in maximum photocurrent and efficiency. For the control measurements, photocurrent was measured on the plain gold surface with CNDs and TiO<sub>2</sub> as shown in Figure 4.7(a) and in gold nanoslit electrode without CNDs and only with TiO<sub>2</sub> nanoparticle immobilization as shown in Figure 4.7(b). For controls, efficiency measured was low as shown in table 4.3.

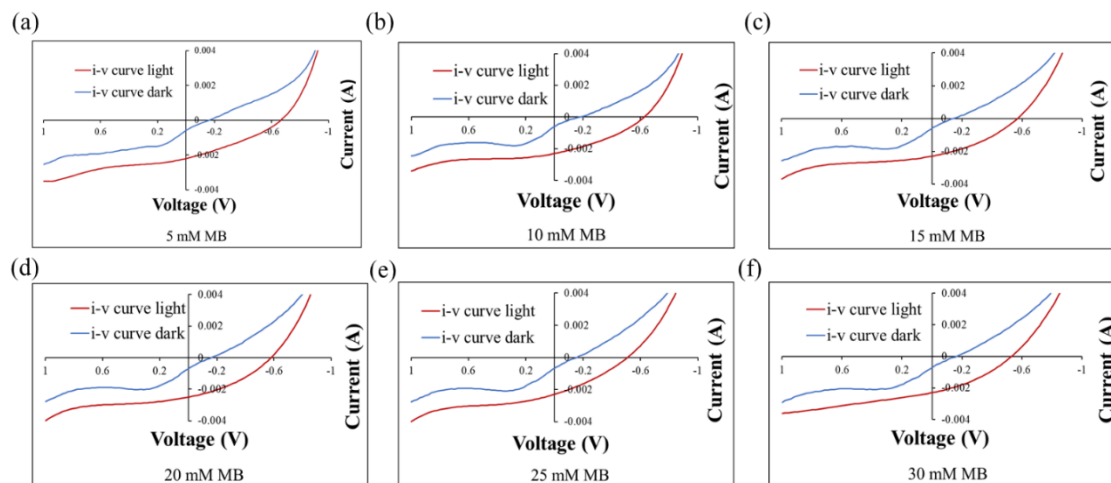


Figure 4.6. (a-f) i-v curve for the functionalized gold nanoslit electrode for different concentration of MB in light and dark condition.

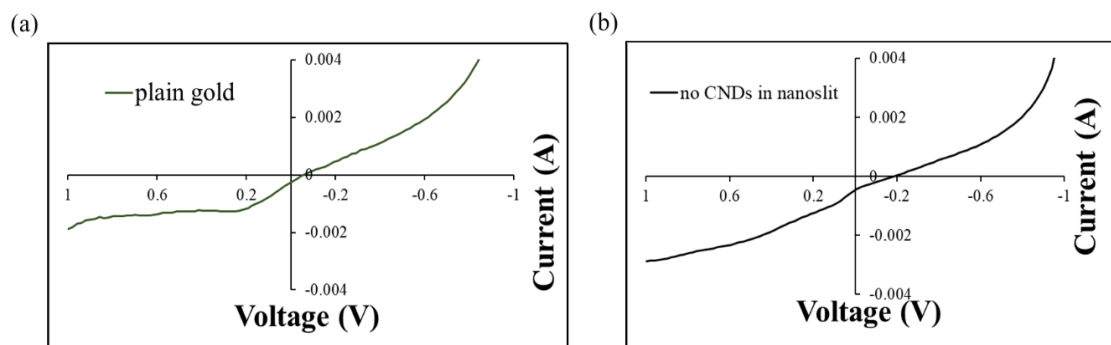


Figure 4.7. i-v curve for the control experiment in light using solar simulator in presence of light (a) photocurrent on plain gold immobilized with CNDs and TiO<sub>2</sub> (b) photocurrent measurement of gold nanoslit electrode with only TiO<sub>2</sub> nanoparticle.

Table 4.1. Different variables calculated for the working electrode in light.

<b>MB conc.</b>	<b>V<sub>max</sub> (V)</b>	<b>I<sub>max</sub> (A)</b>	<b>I<sub>sc</sub> (A)</b>	<b>V<sub>oc</sub> (V)</b>	<b>FF</b>	<b>efficiency</b>
5mM	0.5	0.00118	0.00201	0.53	0.553	3.68
10mM	0.49	0.00121	0.0021	0.51	0.553	3.70
15mM	0.48	0.00126	0.00212	0.51	0.553	3.78
20mM	0.498	0.00131	0.0023	0.55	0.545	4.07
25mM	0.48	0.00125	0.0021	0.48	0.595	3.75
30mM	0.47	0.00123	0.0021	0.505	0.545	3.61

Table 4.2. Different variables calculated for the working electrode in dark.

<b>MB conc.</b>	<b>V<sub>max</sub> (V)</b>	<b>I<sub>max</sub> (A)</b>	<b>I<sub>sc</sub> (A)</b>	<b>V<sub>oc</sub> (V)</b>	<b>FF</b>	<b>efficiency</b>
5mM	0.405	0.00013	0.00105	0.146	0.34	0.329
10mM	0.38	0.00014	0.00101	0.14	0.37	0.332
15mM	0.36	0.00015	0.00104	0.14	0.37	0.337
20mM	0.358	0.000142	0.00106	0.144	0.33	0.317
25mM	0.36	0.000135	0.00108	0.139	0.32	0.303
30mM	0.358	0.000136	0.00107	0.138	0.32	0.304

Table 4.3. Different variables calculated for the control experiment in presence of light.

<b>Control</b>	<b>MB conc.</b>	<b>V<sub>max</sub> (V)</b>	<b>I<sub>max</sub> (A)</b>	<b>I<sub>sc</sub> (A)</b>	<b>V<sub>oc</sub> (V)</b>	<b>FF</b>	<b>efficiency</b>
Plain gold with CNDs and TiO <sub>2</sub>	20 mM	0.32	0.00014	0.00101	0.14	0.31	0.28
Gold nanoslit electrode with TiO <sub>2</sub> nanoparticle only	20 mM	0.37	0.00014	0.00102	0.152	0.33	0.32

We studied the photocurrent generation for the gold nanoslit functionalized device. Under the light illumination, photon-induced electron-hole pair generated in the CNDs. Electrons from CNDs transferred to TiO<sub>2</sub> nanoparticle by direct electron transfer process and then from TiO<sub>2</sub> electrons were accepted by gold electrode via MB, leading to photocurrent generation as shown Figure 4.8. Before, other photon re-excites the CNDs, CNDs must be reduced by accepting electron. MB in the solution act as electron donor to oxidize the CNDs and electron transfer chain continues.

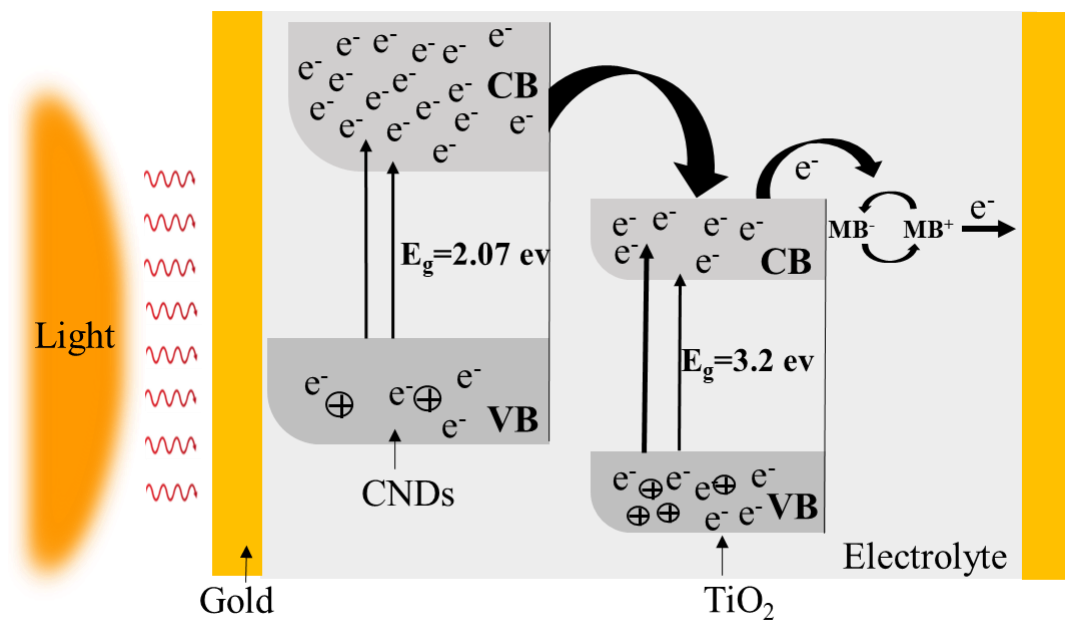


Figure 4.8. A schematic view of the electron transfer chain from CNDs to  $\text{TiO}_2$  to Au electrode.

## Discussion

In this study, we used 100 nm of gold nanoslit functionalized with CNDs and  $\text{TiO}_2$  nanoparticle as the working electrode. As in our previous work we already proved that 100 nm of nanoslit have the maximum Surface Plasmon Generation (SPG) efficiency which results in enhanced electro-magnetic (EM) field intensity [56, 57].

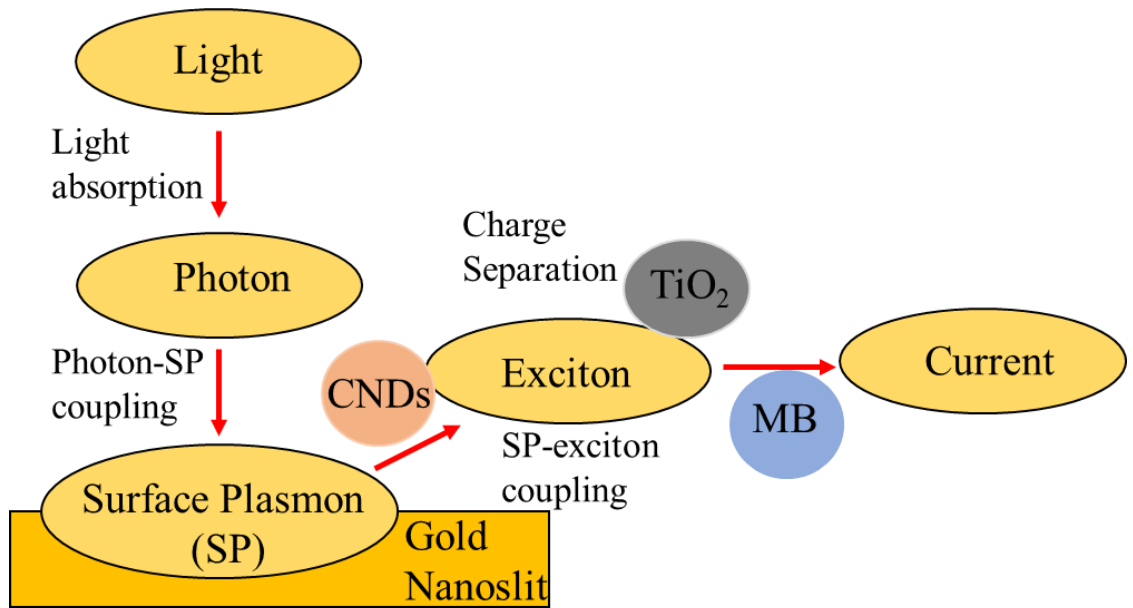


Figure 4.9. Schematic representation showing how plasmon induced the enhanced photocurrent generation.

Enhanced photocurrent generation arises from local enhanced EM field and energy transfer between gold nanoslit and CNDs. Nanoslit structure generates both LSPR and SPP, surface-plasmon induced light trapping/scattering of incident light in nanoslit cavities containing CNDs leads to generation of more energetic electrons in conduction band. Beside this, plasmon-induced resonance energy trapping (PIRET) also contributes for plasmonic enhancement. Dipole-dipole interaction between plasmons in gold and resonance dipoles in CNDs, results in resonance energy transfer from metal film to CNDs via PIRET process. Light trapping or scattering and PIRET generates more electron-hole pairs in CNDs, resulting in highly populated conduction band (CB) with excited electrons. These high energetic electron in conduction band can have three different relaxation pathways. First one, these excited electrons relax to a lower energy level i.e.

valence band (VB) and results in photoemission. Second, is the electron-phonon scattering i.e., phonon emission, leads to rapid thermalization of excited electrons. Third one is electron-hole separation and transfer of electron to nearby molecule or material. In our case, recombination of electron hole pair in excited CNDs is inhibited by TiO<sub>2</sub>. Photogenerated energetic electrons in CNDs directly transferred from CB of CNDs to CB of TiO<sub>2</sub> via direct electron transfer or injection mechanism. LUMO levels of CNDs is in the range of 4.2-4.4 eV and the conduction band potential of TiO<sub>2</sub> is 4.45 eV [52] which makes the electron transfer from CNDs to TiO<sub>2</sub> thermodynamically favorable. Furthermore, lower work function of CNDs results in more photogenerated electrons when excited by visible light. These photogenerated highly energetic electrons efficiently transferred to CB of TiO<sub>2</sub>. From TiO<sub>2</sub>, the electron transferred to MB which act as redox activator results in electron transportation to gold electrode which leads to photocurrent generation. More the EM field intensity produces more generation of excited (high density of state (DOE) at the CB of CNDs, as a result more electron moves to CB of TiO<sub>2</sub> which accelerates electron transfer kinetics, from TiO<sub>2</sub> to gold electrode. As a result, gold electrode, will receive more electrons per unit time scale and resulting in enhanced photocurrent. Figure 4.9 demonstrates the overall picture of the electron generation and their flow within the device. Low efficiency and photocurrent on plain gold immobilized with CNDs and TiO<sub>2</sub> nanoparticle can be explained by the less EM field intensity generation by plain gold surface than gold nanoslit. Low EM filed intensity results in a fewer number of electron-hole pair generation that eventually leads to minimal photocurrent. Similarly, it was noted that in absence of CNDs the photocurrent generation

and efficiency was lower than the CNDs TiO<sub>2</sub> immobilized gold nanoslit electrode. This result well supported the above conclusion that CNDs played an important role of photosensitizers for generation of more electron-hole pairs which eventually enhance the photocurrent generation in photoelectrochemical cell.

### **Conclusion**

This work demonstrates the use of a single metallic nanoslit gap as a photoelectrochemical device design to investigate the plasmon-exciton coupling effect on photocurrent generation and the power conversion efficiency. Metallic nanostructures have the property of SPR which attributed to the light trapping and enhanced EM field in their vicinity which results in more electron-hole pair generation of the CNDs and charge separation when using TiO<sub>2</sub> nanoparticle for photocurrent generation, hence, contributes to enhanced photocurrent. This new study offers the promising breakthrough in the development of a novel plasmonic based solar cells with high energy conversion efficiency

## REFERENCES

- [1] Q. Luo, C. Zhang, X. Deng, H. Zhu, Z. Li, Z. Wang, *et al.*, "Plasmonic Effects of Metallic Nanoparticles on Enhancing Performance of Perovskite Solar Cells," *ACS Applied Materials & Interfaces*, vol. 9, pp. 34821-34832, 2017/10/11 2017.
- [2] M. M. Lee, J. Teuscher, T. Miyasaka, T. N. Murakami, and H. J. Snaith, "Efficient Hybrid Solar Cells Based on Meso-Superstructured Organometal Halide Perovskites," *Science*, vol. 338, pp. 643-647, 2012.
- [3] N. J. Jeon, J. H. Noh, W. S. Yang, Y. C. Kim, S. Ryu, J. Seo, *et al.*, "Compositional engineering of perovskite materials for high-performance solar cells," *Nature*, vol. 517, pp. 476-480, 2015/01/01 2015.
- [4] M. A. Green, K. Emery, Y. Hishikawa, W. Warta, and E. D. Dunlop, "Solar cell efficiency tables (Version 45)," *Progress in Photovoltaics: Research and Applications*, vol. 23, pp. 1-9, 2015.
- [5] F. Enrichi, A. Quandt, and G. C. Righini, "Plasmonic enhanced solar cells: Summary of possible strategies and recent results," *Renewable and Sustainable Energy Reviews*, vol. 82, pp. 2433-2439, 2018/02/01/ 2018.
- [6] S. Morawiec, M. J. Mendes, F. Priolo, and I. Crupi, "Plasmonic nanostructures for light trapping in thin-film solar cells," *Materials Science in Semiconductor Processing*, vol. 92, pp. 10-18, 2019/03/15/ 2019.
- [7] P. Spinelli, M. A. Verschuuren, and A. Polman, "Broadband omnidirectional antireflection coating based on subwavelength surface Mie resonators," *Nature Communications*, vol. 3, p. 692, 2012/02/21 2012.
- [8] E. R. Martins, J. Li, Y. Liu, V. Depauw, Z. Chen, J. Zhou, *et al.*, "Deterministic quasi-random nanostructures for photon control," *Nature Communications*, vol. 4, p. 2665, 2013/10/24 2013.
- [9] J. Zhu, C.-M. Hsu, Z. Yu, S. Fan, and Y. Cui, "Nanodome Solar Cells with Efficient Light Management and Self-Cleaning," *Nano Letters*, vol. 10, pp. 1979-1984, 2010/06/09 2010.
- [10] C. Battaglia, C.-M. Hsu, K. Söderström, J. Escarré, F.-J. Haug, M. Charrière, *et al.*, "Light Trapping in Solar Cells: Can Periodic Beat Random?," *ACS Nano*, vol. 6, pp. 2790-2797, 2012/03/27 2012.

- [11] M. J. Mendes, A. Araújo, A. Vicente, H. Águas, I. Ferreira, E. Fortunato, *et al.*, "Design of optimized wave-optical spheroidal nanostructures for photonic-enhanced solar cells," *Nano Energy*, vol. 26, pp. 286-296, 2016/08/01/ 2016.
- [12] H. A. Atwater and A. Polman, "Plasmonics for improved photovoltaic devices," *Nature Materials*, vol. 9, pp. 205-213, 2010/03/01 2010.
- [13] V. E. Ferry, M. A. Verschuuren, M. C. v. Lare, R. E. I. Schropp, H. A. Atwater, and A. Polman, "Optimized Spatial Correlations for Broadband Light Trapping Nanopatterns in High Efficiency Ultrathin Film a-Si:H Solar Cells," *Nano Letters*, vol. 11, pp. 4239-4245, 2011/10/12 2011.
- [14] H. R. Stuart and D. G. Hall, "Island size effects in nanoparticle-enhanced photodetectors," *Applied Physics Letters*, vol. 73, pp. 3815-3817, 1998.
- [15] V. E. Ferry, L. A. Sweatlock, D. Pacifici, and H. A. Atwater, "Plasmonic Nanostructure Design for Efficient Light Coupling into Solar Cells," *Nano Letters*, vol. 8, pp. 4391-4397, 2008/12/10 2008.
- [16] M. A. Green, "High Efficiency Silicon Solar Cells," in *Seventh E.C. Photovoltaic Solar Energy Conference*, Dordrecht, 1987, pp. 681-687.
- [17] J. Q. Xi, M. F. Schubert, J. K. Kim, E. F. Schubert, M. Chen, S.-Y. Lin, *et al.*, "Optical thin-film materials with low refractive index for broadband elimination of Fresnel reflection," *Nature Photonics*, vol. 1, pp. 176-179, 2007/03/01 2007.
- [18] Y.-F. Huang, S. Chattopadhyay, Y.-J. Jen, C.-Y. Peng, T.-A. Liu, Y.-K. Hsu, *et al.*, "Improved broadband and quasi-omnidirectional anti-reflection properties with biomimetic silicon nanostructures," *Nature Nanotechnology*, vol. 2, pp. 770-774, 2007/12/01 2007.
- [19] Y.-J. Lee, D. S. Ruby, D. W. Peters, B. B. McKenzie, and J. W. P. Hsu, "ZnO Nanostructures as Efficient Antireflection Layers in Solar Cells," *Nano Letters*, vol. 8, pp. 1501-1505, 2008/05/01 2008.
- [20] T. Lohmüller, M. Helgert, M. Sundermann, R. Brunner, and J. P. Spatz, "Biomimetic Interfaces for High-Performance Optics in the Deep-UV Light Range," *Nano Letters*, vol. 8, pp. 1429-1433, 2008/05/01 2008.
- [21] W. L. Barnes, A. Dereux, and T. W. Ebbesen, "Surface plasmon subwavelength optics," *Nature*, vol. 424, pp. 824-830, 2003/08/01 2003.
- [22] K. Nakayama, K. Tanabe, and H. A. Atwater, "Plasmonic nanoparticle enhanced light absorption in GaAs solar cells," *Applied Physics Letters*, vol. 93, p. 121904, 2008.

- [23] S. Butun, E. Palacios, J. D. Cain, Z. Liu, V. P. Dravid, and K. Aydin, "Quantifying Plasmon-Enhanced Light Absorption in Monolayer WS<sub>2</sub> Films," *ACS Applied Materials & Interfaces*, vol. 9, pp. 15044-15051, 2017/05/03 2017.
- [24] G. Singh and S. S. Verma, "Plasmon enhanced light trapping in thin film GaAs solar cells by Al nanoparticle array," *Physics Letters A*, vol. 383, pp. 1526-1530, 2019/04/24/ 2019.
- [25] K. Yao, H. Zhong, Z. Liu, M. Xiong, S. Leng, J. Zhang, *et al.*, "Plasmonic Metal Nanoparticles with Core–Bishell Structure for High-Performance Organic and Perovskite Solar Cells," *ACS Nano*, vol. 13, pp. 5397-5409, 2019/05/28 2019.
- [26] A. Polman, "Plasmonics Applied," *Science*, vol. 322, pp. 868-869, 2008.
- [27] W. Ye, R. Long, H. Huang, and Y. Xiong, "Plasmonic nanostructures in solar energy conversion," *Journal of Materials Chemistry C*, vol. 5, pp. 1008-1021, 2017.
- [28] D. Thrithamarassery Gangadharan, Z. Xu, Y. Liu, R. Izquierdo, and D. Ma, "Recent advancements in plasmon-enhanced promising third-generation solar cells," in *Nanophotonics* vol. 6, ed, 2017, p. 153.
- [29] P. Mandal and S. Sharma, "Progress in plasmonic solar cell efficiency improvement: A status review," *Renewable and Sustainable Energy Reviews*, vol. 65, pp. 537-552, 2016/11/01/ 2016.
- [30] M. A. Green and S. Pillai, "Harnessing plasmonics for solar cells," *Nature Photonics*, vol. 6, pp. 130-132, 2012/03/01 2012.
- [31] D. Zhang, X. Yang, X. Hong, Y. Liu, and J. Feng, "Aluminum nanoparticles enhanced light absorption in silicon solar cell by surface plasmon resonance," *Optical and Quantum Electronics*, vol. 47, pp. 1421-1427, 2015/06/01 2015.
- [32] A. Ono, Y. Enomoto, Y. Matsumura, H. Satoh, and H. Inokawa, "Broadband absorption enhancement of thin SOI photodiode with high-density gold nanoparticles," *Optical Materials Express*, vol. 4, pp. 725-732, 2014/04/01 2014.
- [33] T. L. Temple, G. D. K. Mahanama, H. S. Reehal, and D. M. Bagnall, "Influence of localized surface plasmon excitation in silver nanoparticles on the performance of silicon solar cells," *Solar Energy Materials and Solar Cells*, vol. 93, pp. 1978-1985, 2009/11/01/ 2009.
- [34] K. R. Catchpole and A. Polman, "Design principles for particle plasmon enhanced solar cells," *Applied Physics Letters*, vol. 93, p. 191113, 2008.

- [35] T. V. Pfeiffer, J. Ortiz-Gonzalez, R. Santbergen, H. Tan, A. S. Ott, M. Zeman, *et al.*, "Plasmonic Nanoparticle Films for Solar Cell Applications Fabricated by Size-selective Aerosol Deposition," *Energy Procedia*, vol. 60, pp. 3-12, 2014/01/01/ 2014.
- [36] P. Spinelli and A. Polman, "Prospects of near-field plasmonic absorption enhancement in semiconductor materials using embedded Ag nanoparticles," *Optics Express*, vol. 20, pp. A641-A654, 2012/09/10 2012.
- [37] J.-Y. Lee and P. Peumans, "The origin of enhanced optical absorption in solar cells with metal nanoparticles embedded in the active layer," *Optics Express*, vol. 18, pp. 10078-10087, 2010/05/10 2010.
- [38] F. Ye, M. Burns, and M. Naughton, *Embedded metallic nanopatterns for enhanced optical absorption* vol. 8111: SPIE, 2011.
- [39] M. J. Mendes, S. Morawiec, T. Mateus, A. Lyubchyk, H. Águas, I. Ferreira, *et al.*, "Broadband light trapping in thin film solar cells with self-organized plasmonic nanocolloids," *Nanotechnology*, vol. 26, p. 135202, 2015/03/11 2015.
- [40] E. Wang, T. P. White, and K. R. Catchpole, "Resonant enhancement of dielectric and metal nanoparticle arrays for light trapping in solar cells," *Optics Express*, vol. 20, pp. 13226-13237, 2012/06/04 2012.
- [41] M. R. M. Atalla, "Multiple excitations of surface-plasmon-polariton waves in an amorphous silicon p-i-n solar cell using Fourier harmonics and compound gratings," *Journal of the Optical Society of America B*, vol. 31, pp. 1906-1914, 2014/08/01 2014.
- [42] P. Prabhathan and V. M. Murukeshan, "Surface Plasmon Polariton-coupled Waveguide Back Reflector in Thin-film Silicon Solar Cell," *Plasmonics*, vol. 11, pp. 253-260, 2016/02/01 2016.
- [43] L. V. Mercaldo, I. Usatii, E. Bobeico, F. Russo, L. Lancellotti, and P. D. Veneri, "Optical Performance of Ag-based Back Reflectors with different Spacers in Thin Film Si Solar Cells," *Energy Procedia*, vol. 84, pp. 221-227, 2015/12/01/ 2015.
- [44] J. Chantana, Y. Yang, Y. Sobajima, C. Sada, A. Matsuda, and H. Okamoto, "Localized surface plasmon enhanced microcrystalline-silicon solar cells," *Journal of Non-Crystalline Solids*, vol. 358, pp. 2319-2323, 2012/09/01/ 2012.
- [45] F. Huang, J. Hou, Q. Zhang, Y. Wang, R. C. Massé, S. Peng, *et al.*, "Doubling the power conversion efficiency in CdS/CdSe quantum dot sensitized solar cells with a ZnSe passivation layer," *Nano Energy*, vol. 26, pp. 114-122, 2016/08/01/ 2016.

- [46] S. Jiao, J. Wang, Q. Shen, Y. Li, and X. Zhong, "Surface engineering of PbS quantum dot sensitized solar cells with a conversion efficiency exceeding 7%," *Journal of Materials Chemistry A*, vol. 4, pp. 7214-7221, 2016.
- [47] J. Wang, I. Mora-Seró, Z. Pan, K. Zhao, H. Zhang, Y. Feng, *et al.*, "Core/Shell Colloidal Quantum Dot Exciplex States for the Development of Highly Efficient Quantum-Dot-Sensitized Solar Cells," *Journal of the American Chemical Society*, vol. 135, pp. 15913-15922, 2013/10/23 2013.
- [48] T. Majumder and S. P. Mondal, "Graphene quantum dots as a green photosensitizer with carbon-doped ZnO nanorods for quantum-dot-sensitized solar cell applications," *Bulletin of Materials Science*, vol. 42, p. 65, March 06 2019.
- [49] K. Zhao, Z. Pan, I. Mora-Seró, E. Cánovas, H. Wang, Y. Song, *et al.*, "Boosting Power Conversion Efficiencies of Quantum-Dot-Sensitized Solar Cells Beyond 8% by Recombination Control," *Journal of the American Chemical Society*, vol. 137, pp. 5602-5609, 2015/04/29 2015.
- [50] Z. Ma, Y.-L. Zhang, L. Wang, H. Ming, H. Li, X. Zhang, *et al.*, "Bioinspired Photoelectric Conversion System Based on Carbon-Quantum-Dot-Doped Dye-Semiconductor Complex," *ACS Applied Materials & Interfaces*, vol. 5, pp. 5080-5084, 2013/06/12 2013.
- [51] P. Mirtchev, E. J. Henderson, N. Soheilnia, C. M. Yip, and G. A. Ozin, "Solution phase synthesis of carbon quantum dots as sensitizers for nanocrystalline TiO<sub>2</sub> solar cells," *Journal of Materials Chemistry*, vol. 22, pp. 1265-1269, 2012.
- [52] Y.-Q. Zhang, D.-K. Ma, Y.-G. Zhang, W. Chen, and S.-M. Huang, "N-doped carbon quantum dots for TiO<sub>2</sub>-based photocatalysts and dye-sensitized solar cells," *Nano Energy*, vol. 2, pp. 545-552, 2013/09/01/ 2013.
- [53] J. Briscoe, A. Marinovic, M. Sevilla, S. Dunn, and M. Titirici, "Biomass-Derived Carbon Quantum Dot Sensitizers for Solid-State Nanostructured Solar Cells," *Angewandte Chemie International Edition*, vol. 54, pp. 4463-4468, 2015.
- [54] J. T. Margraf, F. Lodermeier, V. Strauss, P. Haines, J. Walter, W. Peukert, *et al.*, "Using carbon nanodots as inexpensive and environmentally friendly sensitizers in mesoscopic solar cells," *Nanoscale Horizons*, vol. 1, pp. 220-226, 2016.
- [55] Q. Zhang, G. Zhang, X. Sun, K. Yin, and H. Li, "Improving the Power Conversion Efficiency of Carbon Quantum Dot-Sensitized Solar Cells by Growing the Dots on a TiO<sub>2</sub> Photoanode In Situ," *Nanomaterials*, vol. 7, p. 130, 2017.

[56] Z. Zeng, T. Mabe, W. Zhang, B. Bagra, Z. Ji, Z. Yin, *et al.*, "Plasmon-exciton Coupling in Photosystem I Based Biohybrid Photoelectrochemical Cells," *ACS Applied Bio Materials*, 2018/08/15 2018.

[57] B. Bagra, W. Zhang, Z. Zeng, T. Mabe, and J. Wei, "Plasmon-Enhanced Fluorescence of Carbon Nanodots in Gold Nanoslit Cavities," *Langmuir*, vol. 35, pp. 8903-8909, 2019/07/09 2019.

## CHAPTER V

### A PLASMONIC NANOEDGE ARRAY SENSOR FOR DETECTION OF ANTI-INSULIN ANTIBODIES OF TYPE 1 DIABETES BIOMARKER

This chapter has been published as: Bagra, B., Mabe, T., Tukur, F., Wei, J. A plasmonic nanoledge array sensor for detection of anti-insulin antibodies of type 1 diabetes biomarker. *Nanotechnology* 2020, Volume 31, Number 32.

#### Overview

Here we present, a plasmonic nanoledge device with high sensitivity and selectivity used to detect protein biomarkers simply by functionalizing the device, which specifically binds to particular biomolecule or biomarkers. We employ this plasmonic nanoledge device for the detection of anti-insulin antibody of type 1 diabetes (T1D) in buffer and human serum at the range of  $\text{pg ml}^{-1}$  to  $100 \text{ ng ml}^{-1}$ . The signal transduction is based on the extraordinary optical transmission (EOT) through the nanoledge array and the optical spectral changes with the biological binding reaction between the surface functionalized insulin with anti-insulin antibody. Control experiments indicate little interferences from the human serum background and addition of other proteins such as bovine serum albumin (BSA) and epidermal growth factor (EGF) at  $20 \text{ ng ml}^{-1}$ . The high sensitivity, specificity and easy adaptability of plasmonic device offer new opportunities in biosensing and diagnostic applications for T1D.

## **Introduction**

Biomolecules or biomarkers play an important role in disease diagnosis and treatment [1]. A few methods have been demonstrated for biomolecules or biomarker detection, including Surface Enhanced Raman Spectroscopy (SERS) [2], Enzyme-Linked immunosorbent assay (ELISA) [3], colorimetry [4] and, electrochemical assay [5]. There are unmet needs which motivate to improve performance in terms of sensitivity, detection limit, turnaround time, sample amount, sample preparation requirements, multiplexing (multiple samples at a time), instrumentation, compactness, and portability [1]. Use of metal nanostructures in the biosensors has been an attractive and one of the most promising alternative methods [6]. Noble metal nanostructures have the property of Surface Plasmon Resonance (SPR) [7] and this property can be utilized to improve the sensitivity and selectivity of the currently available methods [8].

SPR detection methods have been gaining popularity lately because of their ability to handle complex samples and to provide label-free optical biosensors with real time detection [8-10]. These sensors can handle complex samples such as human serum/blood without tedious preparation and pretreatment [11, 12]. SPR makes use of nanostructures and/or nanostructured metal films which removes the need for complex detection instrumentation [13]. These abilities of SPR make it a good candidate for creating a plasmonic sensor which is easy to use, reliable, capable of on-site detection, selective, and sensitive enough to measure low concentration of biomolecules or biomarker targets[14-17]. Coupled with microfluidics, SPR detection can be used as a handheld device for easy diagnosis and treatment [18].

SPR can presents localized surface plasmon resonance (LSPR) or Surface Plasmon Polariton (SPP) [19] which can increase the local field near the metallic surfaces for sensing, optical enhancement, and/or energy conversion. When the metal structure gets smaller than the wavelength of incident light, it gives rise to a phenomenon called LSPR. LSPR is caused by electron oscillations (plasmons) at the surface that are “localized” within the nanostructure [20]. Various nanostructures such as nanoparticles, nanorods and other shapes have been studied for the LSPR generation [20, 21]. LSPR is very sensitive to the refractive index of the surrounding medium [22] and this property can be harnessed for biomolecule or biomarker detection. Whenever there is a binding between the surface-bound ligands and free biomarkers or biomolecules on the plasmonic surface, there will be change in the refractive index (dielectric constant) of the surrounding medium. This change in refractive index contributes to a change in the resonant frequency of the plasmon and that phenomenon can be used for detection of various biomarkers or biomolecules [23]. Various different shapes like lines, ledges, circles, rings, and squares can be milled on the surface of nanostructured metal films [24]. Metal films with the subwavelength nanostructures [25] exhibit the phenomenon called extraordinary optical transmission (EOT) [26] and scientists make use of this property while fabricating various detection devices. The array of nanostructures milled over the metal surface in periodic fashion transmit more light than the bulk at certain wavelengths [27]. Transmission SPR spectroscopy (tSPR) based on EOT and LSPR [28, 29] is of interest to many researchers for sensing or detection devices. The tSPR can be used by measuring the EOT allowing for high transmission of light. The small size of these

structures allows for easy incorporation of a light source and detector. This easy alignment and sensitivity due to EOT and LSPR allows for advancement in new lab on chip technology. This technology does not require any prisms, precision optics, or temperature control, further making tSPR based-sensors small, compact, and easy to carry [30]

In this work, detection of anti-insulin antibodies as a biomarker of type 1 Diabetes (T1D) was chosen as a model system. Anti-insulin antibody present in the body fights against the body's own insulin cells [31] and decreases the amount of insulin in the body which leads to insulin deficiency and results in T1D. The World Health Organization projects that the global prevalence of diabetes will increase from 217 million cases in 2005 to 366 million by 2030 [32]. Along with being a common disease in adults, diabetes is now the second most common pediatric disease. T1D is an autoimmune form of diabetes and the rate of T1D in children is rising with 3% annual rate [33, 34]. Known for being a pediatric disease, T1D is now diagnosed during adulthood for approximately one-fourth of patients [35]. T1D results from cellular mediated autoimmune destruction of the insulin producing pancreatic  $\beta$ -cells [36]. Patients suffering from T1D, frequently show life threatening symptoms like ketoacidosis, and all of them require insulin therapy for life. With the commencement or onset of T1D, patients have autoantibodies to at least one of the following: islet cell cytoplasm, insulin [insulin autoantibodies (IAAs)] [37], the 65-kDa isoform of glutamic acid decarboxylase (GAD65), insulinoma-associated antigen 2 (IA-2), and zinc transporter 8 (ZnT8) (these are collectively termed islet autoantibodies) [38, 39]. The development of T1D is predicted by islet autoantibodies.

While both electrochemical and SPR methods have been developed for insulin assays [40], there is an unmet need of medical devices for quantification of islet autoantibodies. Current diabetes diagnostics tests like ELISA and lateral flow assay are slow and costly, thus making this key test less accessible in areas with limited resources. In spite of a need for better diagnostics tests, their development has been challenging. It has been demonstrated over the past two decades that usual platforms like lateral flow assays and ELISA do not perform up to the mark when applied to T1D diagnostics, and thus don't meet the sensitivity and specificity required for this medical situation [41, 42].

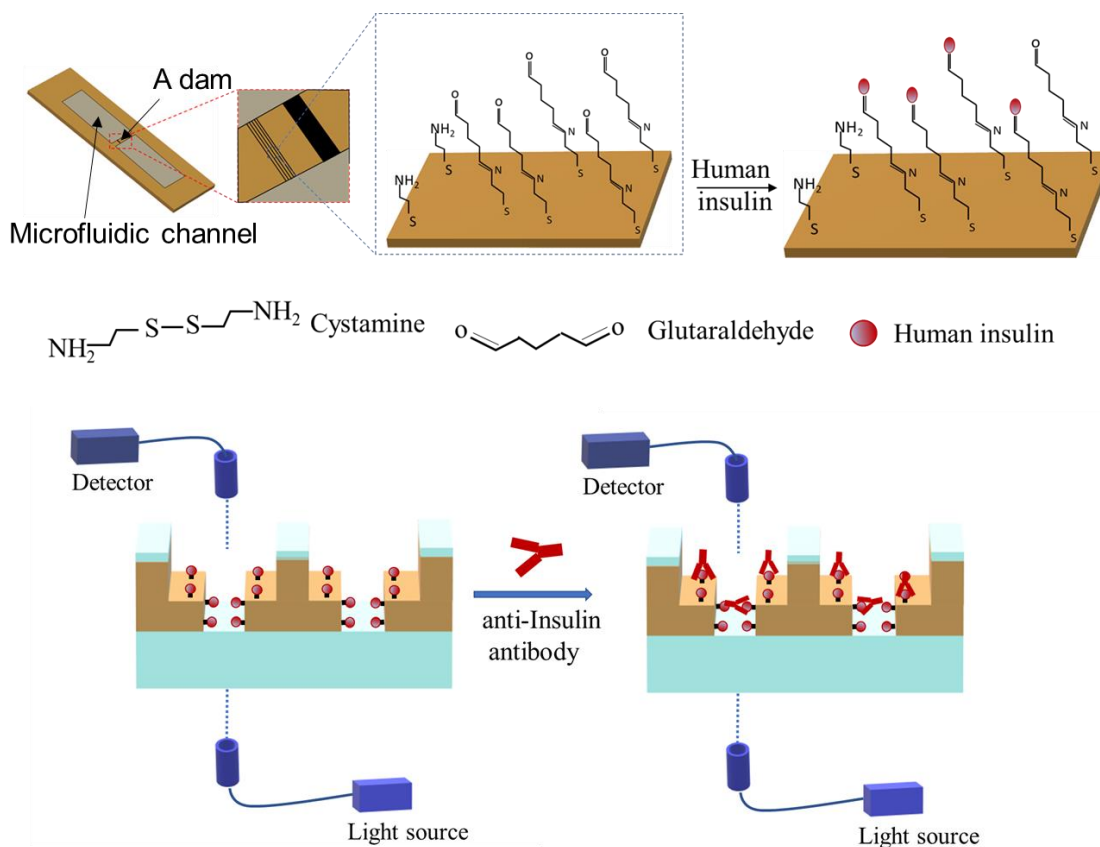


Figure 5.1. Illustration of the gold surface functionalization at the gold surfaces of the nanoledge array to immobilize human insulins and the model of plasmonic nanoledge device used for biomarker or biomolecule detection.

Based on recent advances in plasmonic nanoslit and nanoledge cavities for trapping and detection of various biomolecules or biomarkers[43], a plasmonic chip with a nanostructured nanoledge array in the metal film on a dam cross a microfluidic channel [43] was developed as shown in Figure 5.1 for detection of anti-insulin antibodies of T1D. The dam structure crosses a micro-channel that offers an advantage of using less sample volume for analysis. The nanostructured ledge array fabricated on the dam provides better capture of small biomolecules/biomarkers than straight nanoslits as it combines 50 nm of inner slits and 280 nm of outer slit. Small biomolecules/biomarkers can be trapped inside the nanoledge slits and hence give better sample delivery and detection sensitivity. The fluidic dam was fabricated with lithography technique. Self-assembled monolayers (SAMs) were formed on the surface of the exposed gold in nanoledge array. This allowed for easy linkage of Human insulin to the gold surface. Then anti-insulin antibodies were flowed over the human insulin and monitored by a wavelength shift after binding between the anti-insulin antibodies and the human insulin platform. This overcomes the major challenges in rapid, sensitive, and specific diagnosis of T1D, by allowing successful detection of ultra-low volumes of samples (buffer and human serum) containing T1D anti-insulin antibodies. This new platform offers promise to point-of-care detection of several isotypes of anti-insulin antibodies without any fluorescence labelling on a single chip [44].

## **Experimental Section**

### ***Materials and reagents***

Cystamine, Glutaraldehyde, Polyethylene glycol (PEG), Human insulin and auto-Insulin antibody were purchased from Sigma-Aldrich and used without further purification. All other solvents and chemicals were purchased from Sigma-Aldrich. LS 1 light source was purchased from Ocean Optics.

### ***Fabrication of nanoledge plasmonic chip***

In this study, a lithography technique with FIB (Focused Ion Beam) was developed as shown in Figure 5.2 to fabricate a flow-over fluidic dam with nanoledge structures. A multi-layer resist was used to get the side-wall sloped profile in desired direction. Photomask was designed in Auto computer-aided design (Auto CAD) software. Glass substrates (Glove Scientific) were prepared by treatment with a piranha acid (3:1 H<sub>2</sub>SO<sub>4</sub>:H<sub>2</sub>O<sub>2</sub>) solution, rinsing with deionized (DI) water, and N<sub>2</sub> drying. The substrates were dehydrated on a hot plate for more than 5 min at temperature 90 °C. SU-8 3050 photoresist (MicroChem) was applied to a clean, dry glass slide. Subsequently, the substrate was soft-baked and flood-exposed (no mask) by OAI mask aligner (Milpitas, CA, USA) and then hard-baked to develop a structural layer of SU-8. A 100 nm SiO<sub>2</sub> film was then deposited by physical vapour deposition (PVD75, Kurt Lesker) upon the SU-8 layer. Subsequently, second layer of NFR 016 D2 negative photoresist (JSR Micro) was applied and patterned by standard photolithography technique. NFR 016 D2 was first spin applied and soft baked at 90 °C for 150s on hot plate. Followed by exposure through the negative CAD photomask for 9s by OAI mask aligner with the dose of 100mJ/cm<sup>2</sup>.

Then the post bake was performed at 90 °C for 120 s, and resist was developed using PD523AD for 1 min, then rinsed with water, and dried with N<sub>2</sub> gun. Using the NFR resist as an etch mask, CF<sub>4</sub> and O<sub>2</sub> gases from a LAM Rainbow 4400 reactive ion etcher (RIE) were used to etch the oxide layer. The SU-8 layer was dry etched isotropically, in a controlled manner, with an O<sub>2</sub> plasma using SiO<sub>2</sub> as an etch mask. Etch parameter used were 100 mT pressure, RF power 100 W, bias -152 V, time 5 mins, CF<sub>4</sub> 45 sccm and O<sub>2</sub> 5 sccm flow rate. A small amount (about 3% to 5%) of SF<sub>6</sub> was added to the gas mixture and it improved the surface roughness of the SU-8 layer. Regulating the etch chamber pressure, gas mixture, and RF power gave tunability to the slope and sidewall profile of the dam structures. Overcut sidewall profiles (slopes < 90°) were desired and achieved by tuning the RIE's chamber parameters. The sloped profile with less than 90° angle can be easily coated uniformly everywhere by PVD. As PVD is directional deposition technique so we need to have overcut profile for uniform deposition of metal everywhere. The sloped profile was then transferred to PVD for deposition of 4 nm Ti + 250 nm Au + 4 nm Ti + 100 nm SiO<sub>2</sub>, with the Ti layers serving as adhesion layers. The thicknesses of the film and the deposition rate were monitored with a quartz crystal microbalance (QCM) and were further checked with a profilometer (KLA Tencor P-10). Nanoledge structures were then milled into the devices on top of the dam structures. Fibics software and a Zeiss Auriga Dual beam FIB/SEM were used for milling. Arrays of 100 nanoledge with 600 nm spacing periodicity between each structure were milled on the dam along with a reference box or burn box which did not have any gold film or any nanoledge structure. The 50 nm inner slit was milled using a 50-pA probe while the outer 280 nm

step was milled using a 140-pA probe. We used 280 nm-50 nm dimensions as these dimensions have maximum plasmons generation efficiency based on previously reported results[45].

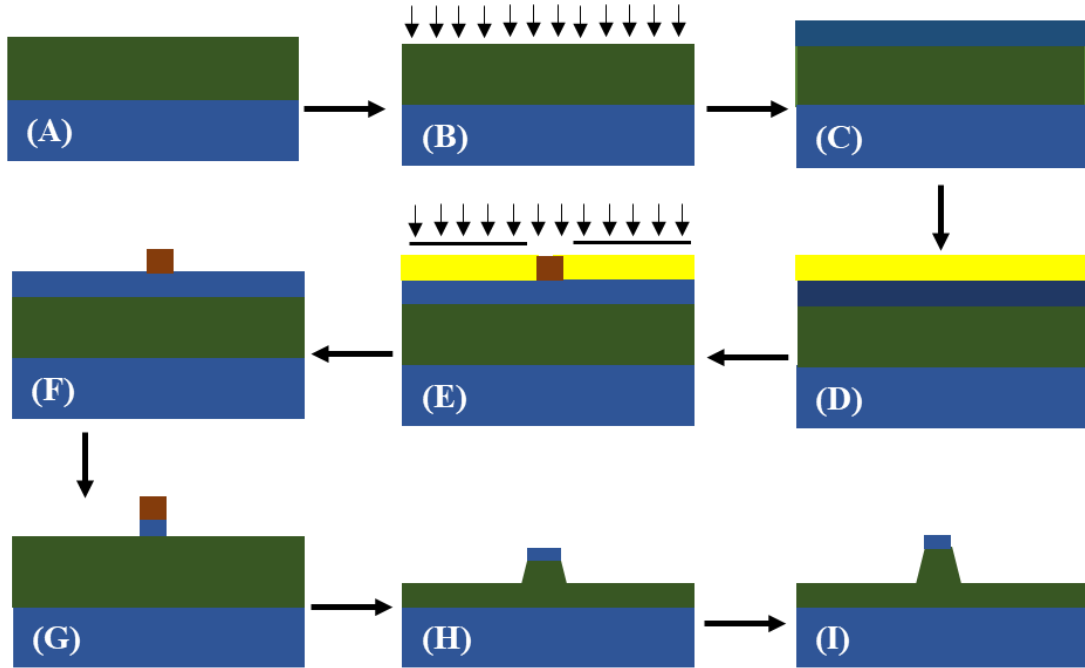


Figure 5.2. Fabrication Process for the Flow-over Fluidic Dam using a Multi-layered Resist (MLR) Method. (A) Spin Apply SU-8 Photoresist and Soft Bake, (B) Flood Expose and Bake the SU-8 post Exposure, (C) Deposit 100 nm of SiO<sub>2</sub> atop the Cross-linked SU-8 Structural Layer, (D) Spin Apply JSR NFR 016D2 Photoresist, (E) Expose the JSR NFR Photoresist through the Photomask with Design of the Flow-over Dam, (F) Bake and Develop the JSR NFR Post Exposure, (G) Dry Etch the SiO<sub>2</sub> Layer with a CF<sub>4</sub>/O<sub>2</sub> Plasma, (H) Dry Etch the SU-8 Layer with an O<sub>2</sub> Plasma, (I) Deposit 4 nm Ti, 250 nm Au, 4 nm Ti, and 100 nm SiO<sub>2</sub>.

### ***Functionalization of the plasmonic chip***

Cystamine and glutaraldehyde chemistry was used to establish the self-assembled monolayer (SAM). A chip surface was thoroughly cleaned with an ethanol rinse, O<sub>2</sub> plasma clean, ethanol rinse, N<sub>2</sub> dry, and UV/Ozone treatment. The oxygen plasma

treatment was done for 5 min at 100 W in an oxygen plasma cleaner (South Bay Technologies PC-2000 Plasma Cleaner) at 178.6 mTorr O<sub>2</sub> pressure and a -783 volts DC bias. A 5 mM solution of cystamine in 90% ethanol solution was used to form a SAM with the reaction catalysis done by a microwave synthesizer. The disulfide bond within the cystamine molecule breaks and yields two sulfur-gold bonds at the surface of the chip. The substrate was then rinsed with an ethanol solution of 90% concentration and then rinsed with DI water in order to remove the unbound molecules. The terminal amine, sticking up from the surface, would then be able to bond to an aldehyde on next reagent, glutaraldehyde, forming an imine bond. A 2.5% solution of glutaraldehyde was used to self-assemble atop of the formed cystamine layer. This provided a terminal aldehyde group to which human insulin can bind. A stock solution of 1 mg ml<sup>-1</sup> of anti-Insulin antibody solution was diluted with a buffer and with human serum to yield working solution of different concentration. This solution was then delivered to the nanostructured Plasmonic Nanoledge area of the chip and allowed to bond for a few minutes. During this time, the entire chip was encased in a high humidity environment so that anti-insulin antibody solution would not dry up and results in good binding between human insulin and anti-insulin antibody. Afterwards, the chip was rinsed and dried with a N<sub>2</sub> stream. Then, the EOT measurements were taken with the modified microscopic spectroscopy.

The chips were re-usable. In order to regenerate the clean metallic surface, the adsorbed SAM could be removed by subjecting the substrates to oxygen plasma (South Bay Technologies, PC-2000 Plasma Cleaner) for 5 minutes at 100 W. The plasma treated substrates were then exposed to sonication in acetone, ethanol, then to water[46] and then

were cleaned for 20 minutes by UV/Ozone exposure[47] using a Bioforce UV/Ozone ProCleaner. It had previously been demonstrated that plasma cleaning does not adversely affect the metallic surfaces and does not add roughness to the surface[48]. This is in contrast to the roughness and pinholes that can occur by some cleaning methods, such as the use of piranha ( $\text{H}_2\text{SO}_4$  and  $\text{H}_2\text{O}_2$ )[49].

## Results and Discussion

### *Fabrication results and optical characterization*

SEM images of a typical fabricated plasmonic nanoedge device is shown in Figure 5.3 (a). Figure 5.3 (b) shows the FIB images with good contrast which clearly shows the inner 50 nm nanoslit and outer 280 nm nanoslit. Each nanoedge has 280 nm outer width and 50 nm inner width slits with a periodicity of 600 nm. The 50 nm inner slits are to capture more biomolecules or biomarkers, thus increasing sensitivity and specificity.

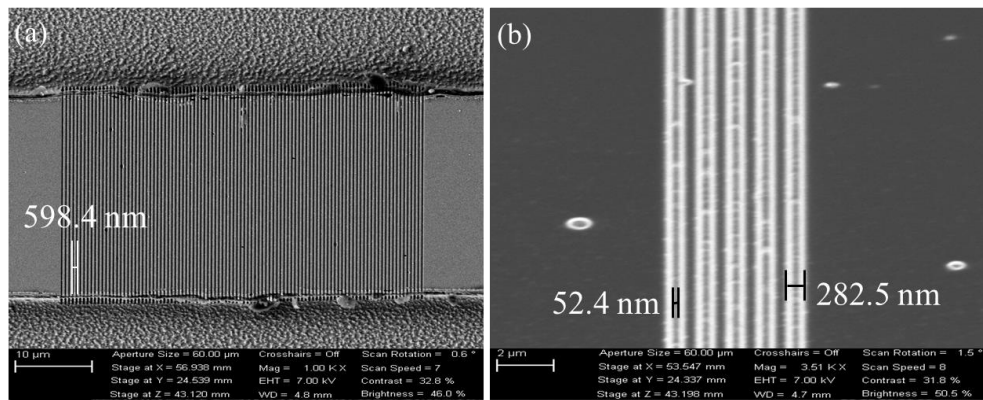


Figure 5.3. (a) SEM image of nanoedge array with 600 nm of periodicity. (b) represent the FIB images of the nanoedge.

Transmission spectrum measurements of plasmonic nanoledge chip were taken in air to gain the resonant peak locations. As shown in optical transmission spectra in Figure 5.4, the primary resonant peak locations are around 630-640 nm and 690-700 nm. Note that transmission spectra showing below is the final transmittance calculated after subtracting dark and reference that we will discuss below. For the measurement, the light source was placed underneath the substrate and shone directly onto the underside of the dam, which contained the nanoledge structures without any modification. For nanoledge structures, which behave as 2-d metallic nanomaterial, have two plasmon bands: longitudinal plasmons band (690-700 nm) and transverse plasmons (630-640 nm) [50]. The transverse plasmons are insensitive to size and surrounding medium but longitudinal plasmon band changes with change in dielectric properties, size, shape and, refractive index of the surrounding medium [51]. This change of the peak or band with the change in surrounding medium is an indicator of sensor response. Here, the peak around 690-700 nm is due to longitudinal plasmons band and changes with the change in the refractive index of the surrounding medium. The Gans theory explained the absorption spectra of the 2-d metallic nanomaterials and shows how absorption spectra changes with the surrounding medium [52].

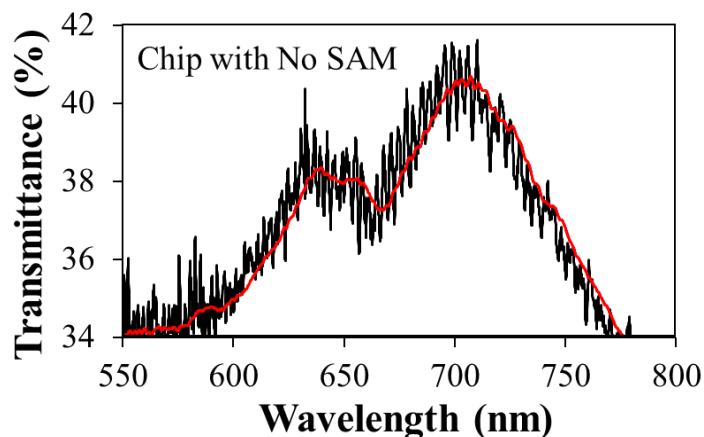


Figure 5.4. Represents the transmittance curve (smoothed in red color and unsmoothed in black color) of fabricated plasmonic chip without any modification.

#### ***Optical detection of T1D biomarker***

The anti-insulin antibody was used as a target in determining the sensitivity of the plasmonic nanoledge device fabricated and functionalized with different techniques as shown in figure S5.1, with the goal of determining if the device would be perceptive enough to determine the low concentration of anti-insulin antibody in buffer and in human serum (HS). The plasmonic nanoledge device was functionalized with human insulin and then different concentrations of anti-insulin antibody in buffer or human serum were flown over the functionalized device, and the optical transmission spectra were recorded using modified microscopic spectrometer (Figure S5.2 and S5.4). Further, the recorded spectra were smoothed and fitted with the best fit polynomial function (up to 8<sup>th</sup> degree) for peak position determination. These experiments were performed with a microscopic spectrometer since it has a microscope and stage that allows for measurements to be taken only from the area of the device with the fabricated dam and nanoledge structures. For our transmission spectra measurements, we used a broadband

white light source (LS 1 Light source, 400-1100 nm) instead of typical lasers. The LS 1 light source was connected to the instrument with a fiber optic cable and light was shining on the back of the sample, allowing optical spectrum collection. The light transmittance of a sample at the detection nanoledge arrays was obtained by equation below:

$$Transmittance = 100 \times \frac{slit - dark}{ref - dark}$$

where, *slit* represents the Nanoledge array, *ref.* is a burn box without any metal coating for full light transmission and, *dark* is any area coated with gold without any nanoledge or burn box and light is blocked.

To determine the peak wavelength shift in the transmission spectrum, a MATLAB program was created to fit the data using a certain order polynomial function to obtain smoothed transmittance curves. The transmittance spectra show red shift along with the antibody biomarker concentration increase. A linear relationship between the concentration (Logarithm value) and wavelength shift was obtained (Figure 5.6) which is typical for an affinity reaction-based sensing [53, 54]. Concentrations of 0.1, 1, 10, and 100 ng ml<sup>-1</sup> of anti-insulin antibody were used to demonstrate the detection capability of the plasmonic nanoledge device. The reaction time for each concentration was 15 mins and then the device was rinsed and dried with nitrogen stream. Then the three sets of the transmission spectra measured three times (3X3) for each concentration in buffer and in human serum, respectively, were recorded. For each concentration total 9 measurements were taken. The results are summarized in tables S5.1 and S5.2.

Figure 5.5 (a)-(b) show the normalized transmittance spectra of anti-insulin antibody taken for different concentration in buffer and in human serum.  $100 \text{ ng ml}^{-1}$  shows the maximum shift and for  $1 \text{ pg ml}^{-1}$  the shift is very small and almost insignificant. The peak shift was obtained by averaging the three sets of measurements. Figure 5.5 (c)-(d) show the wavelength shift with respect to different concentrations of anti-insulin antibody in buffer and in human serum, respectively. These plots both show high linearity, with correlation coefficient ( $R^2$ ) above 0.97-0.98 for both buffer and human serum. The peak shift observed was due to the change in the refractive index at the surface of the plasmonic chip with the binding of anti-insulin antibody. During the surface functionalization, the peak shift after each step of plasmonic chip functionalization was also recorded as shown in Figure S5.3. In order to examine the background of human serum, Human serum contains multiple proteins, so without added anti-insulin antibody Human serum was run and the results are shown in Figure S5.5. The minimal plasmon peak shift during this control concludes that the specificity of human insulin functionalized plasmonic nanoledge chip is very high.

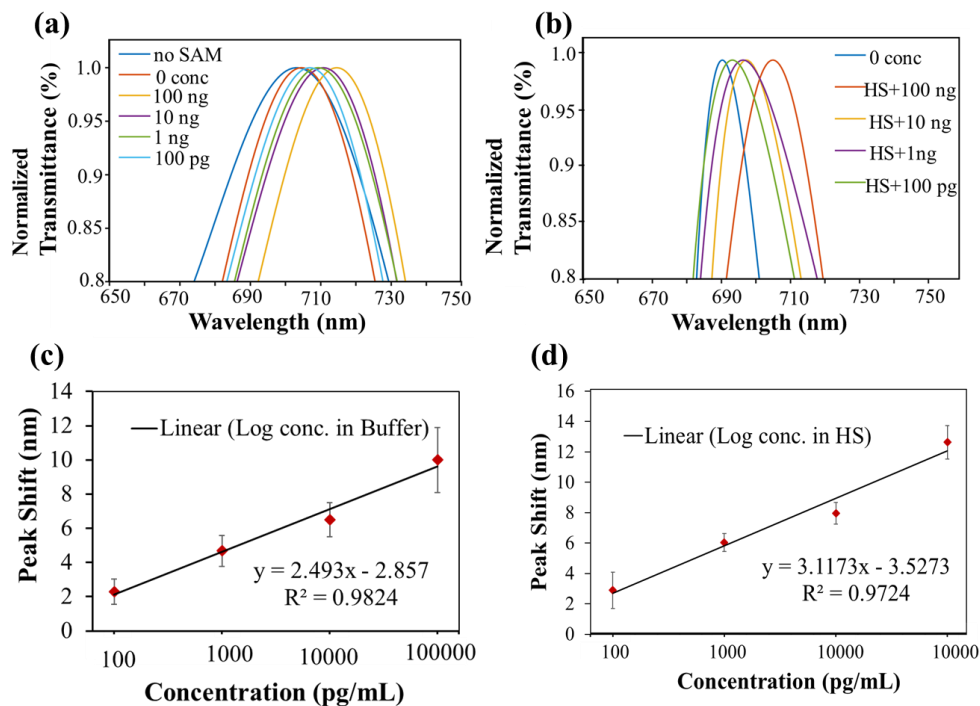


Figure 5.5. Representation of peak shift for anti-insulin antibody (a) in buffer and (b) in human Serum; (c) and (d) show correlation of concentration of anti-insulin antibody with respect to wavelength peak shift, the straight line shows the linear fit.

### Control experiments

Control experiments were performed to verify the specificity and selectivity of the human insulin modified plasmonic nanoledge device. Bovine serum albumin (BSA) and epidermal growth factor (EGF) of concentration (20 ng/mL) were used as a control. The optical peak shift of the insulin functionalized devices with flowing of BSA or EGF in the concentration (20 ng ml<sup>-1</sup>) gives 0.1-0.2 nm from three trials (see Table S5.3), indicating minimal non-specific binding of BSA and EGF to the human insulin-modified plasmonic nanoledge device. Three sets of individually functionalized devices for BSA and EGF binding were measured and the average peak shift is shown in Figure 5.6.

The measured results of the BSA and EGF interference are consistent and effective for the bioassay. The minimal non-specific binding of BSA and EGF to the detection devices indicates the high specificity of the designed biosensor. These results indicate that the plasmonic nanoledge device, along with tailored surface modification with appropriate receptors, can be used as biomarker or biomolecule detection with excellent sensitivity and specificity.

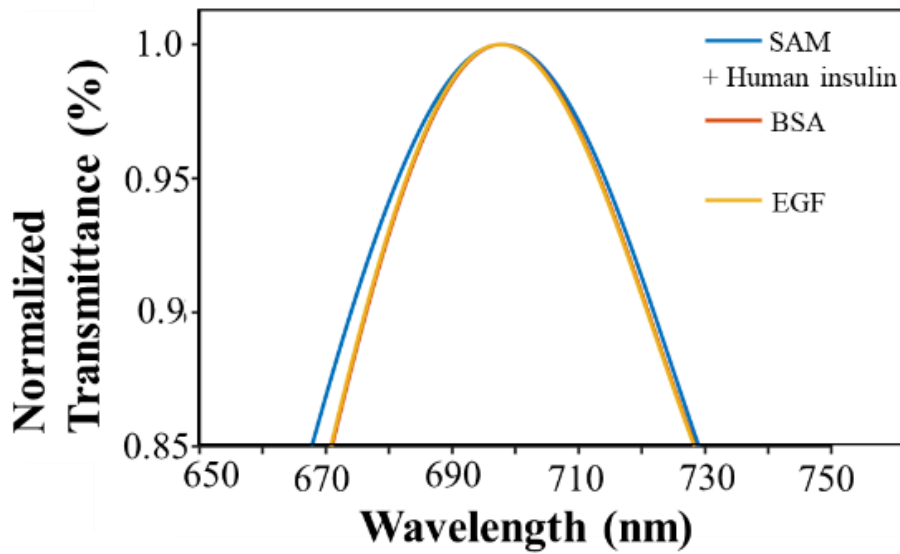


Figure 5.6. Measured peak shift for BSA and EGF to test the specificity of the plasmonic nanoledge device.

According to SPR sensing principle, there is a relationship between the wavelength shift and thickness of layer added as shown in equation 1 [43]:

$$\Delta\lambda = m (n_A - n_B)[1 - \exp(-2d_E/l_d)] \quad (1)$$

where  $\Delta\lambda$  is the peak or wavelength shift,  $m$  is the Refractive Index Unit (RIU) sensitivity,  $n_A$  and  $n_B$  are the refractive index of the medium at the plasmonic sensing

surfaces in nanoledge arrays after and before the biological binding,  $d_E$  is the effective thickness of the added binding layer and,  $l_d$  is the decay length of surface plasmon mode. Addition of different concentration of analytes into the plasmonic nanoledge device results different layer thickness which changes the dielectric constant of the surrounding medium at the gold surfaces, eventually leading to peak shift. There is red shift with the more concentration of the analytes because more concentration means more binding and more peak shift. The peak shift obtained in this work as a function of the concentration is consistent with our previous results from both the theoretical simulation and experiments [43]. Advance in this work of using the plasmonic nanoledge device in human serum biomarker sensing further demonstrates a few advantages over other thin film based SPR devices in terms of sensitivity and specificity. The device is  $\text{SiO}_2$  coated at the top gold surfaces so it allows only in-cavity detection and avoids nonspecific binding at other surface [55]. The plasmonic nanoledge device with outer and inner width generates more coupled SPR-induced optical transmission and trap small size biomolecules or biomarkers to increase sensitivity [43]. This device has the potential application in the field of sensing and may be integrated with smart devices for point-of-care applications.

## **Conclusion**

A novel plasmonic nanoledge device was fabricated with simple lithography and FIB technique which have high sensitivity and selectivity. The plasmonic nanoledge device can be reused with simple cleaning in a plasma cleaner. The device can be used for biomolecule or biomarker detection by simply functionalizing the device accordingly. In this work, human insulin is used to modify the nanoledge devices and demonstrated

for detection of anti-insulin antibody, a protein biomarker of T1D. The optical transmission peak shift was observed with the change in concentration of the protein biomarker binding reactions at the insulin functionalized device. The shift in peak wavelength is due to change in the refractive index or dielectric constant at the surface of the plasmonic nanoledge device. The sensitivity is high as it can detect in picograms concentration in buffer and in human serum. The background of human serum and additional control experiments using BSA and EGF indicate minimal interferences that caused by non-specific binding to the insulin functionalized nanoledge arrays. This study offers promise for the development of a new planar plasmonic microfluidic LOC device for early and quick diagnosis of biomarkers in health care sectors.

## REFERENCES

- [1] S. B. Nimse, M. D. Sonawane, K.-S. Song, and T. Kim, "Biomarker detection technologies and future directions," *Analyst*, vol. 141, pp. 740-755, 2016.
- [2] M. Li, S. K. Cushing, J. Zhang, S. Suri, R. Evans, W. P. Petros, *et al.*, "Three-Dimensional Hierarchical Plasmonic Nano-Architecture Enhanced Surface-Enhanced Raman Scattering Immunosensor for Cancer Biomarker Detection in Blood Plasma," *ACS Nano*, vol. 7, pp. 4967-4976, 2013/06/25 2013.
- [3] A. C. Donahue and M. Albitar, "Antibodies in Biosensing," in *Recognition Receptors in Biosensors*, M. Zourob, Ed., ed New York, NY: Springer New York, 2010, pp. 221-248.
- [4] J. Wang, L. Wu, J. Ren, and X. Qu, "Visualizing Human Telomerase Activity with Primer-Modified Au Nanoparticles," *Small*, vol. 8, pp. 259-264, 2012.
- [5] M. Labib, N. Khan, S. M. Ghobadloo, J. Cheng, J. P. Pezacki, and M. V. Berezovski, "Three-Mode Electrochemical Sensing of Ultralow MicroRNA Levels," *Journal of the American Chemical Society*, vol. 135, pp. 3027-3038, 2013/02/27 2013.
- [6] S. Krishnamoorthy, "Nanostructured sensors for biomedical applications—a current perspective," *Current Opinion in Biotechnology*, vol. 34, pp. 118-124, 2015/08/01/ 2015.
- [7] J. Homola and M. Piliarik, "Surface plasmon resonance (SPR) sensors," in *Surface plasmon resonance based sensors*, ed: Springer, 2006, pp. 45-67.
- [8] B. A. Prabowo, A. Purwidyantri, and K.-C. Liu, "Surface Plasmon Resonance Optical Sensor: A Review on Light Source Technology," *Biosensors*, vol. 8, p. 80, 2018.
- [9] S. T. Seiler, I. S. Rich, and N. C. Lindquist, "Direct spectral imaging of plasmonic nanohole arrays for real-time sensing," *Nanotechnology*, vol. 27, p. 184001, 2016/03/24 2016.
- [10] J. Zhu, Z. Wang, S. Lin, S. Jiang, X. Liu, and S. Guo, "Low-cost flexible plasmonic nanobump metasurfaces for label-free sensing of serum tumor marker," *Biosensors and Bioelectronics*, vol. 150, p. 111905, 2020/02/15/ 2020.
- [11] Y. Zeng, R. Hu, L. Wang, D. Gu, J. He, S.-Y. Wu, *et al.*, "Recent advances in surface plasmon resonance imaging: detection speed, sensitivity, and portability," *Nanophotonics*, vol. 6, pp. 1017–1030, June 01, 2017 2017.

- [12] J. Zhou, F. Tao, J. Zhu, S. Lin, Z. Wang, X. Wang, *et al.*, "Portable tumor biosensing of serum by plasmonic biochips in combination with nanoimprint and microfluidics," in *Nanophotonics* vol. 8, ed, 2019, p. 307.
- [13] A. Olaru, C. Bala, N. Jaffrezic-Renault, and H. Y. Aboul-Enein, "Surface Plasmon Resonance (SPR) Biosensors in Pharmaceutical Analysis," *Critical Reviews in Analytical Chemistry*, vol. 45, pp. 97-105, 2015/04/03 2015.
- [14] J.-F. Masson, "Surface Plasmon Resonance Clinical Biosensors for Medical Diagnostics," *ACS Sensors*, vol. 2, pp. 16-30, 2017/01/27 2017.
- [15] R. T. Hill, "Plasmonic biosensors," *WIREs Nanomedicine and Nanobiotechnology*, vol. 7, pp. 152-168, 2015.
- [16] S. Firdous, S. Anwar, and R. Rafya, "Development of surface plasmon resonance (SPR) biosensors for use in the diagnostics of malignant and infectious diseases," *Laser Physics Letters*, vol. 15, p. 065602, 2018/04/26 2018.
- [17] J. Zhu, X. Chen, Y. Xie, J.-Y. Ou, H. Chen, and H. Liu Qing, "Imprinted plasmonic measuring nanocylinders for nanoscale volumes of materials," in *Nanophotonics* vol. 9, ed, 2020, p. 167.
- [18] W. Jung, J. Han, J.-W. Choi, and C. H. Ahn, "Point-of-care testing (POCT) diagnostic systems using microfluidic lab-on-a-chip technologies," *Microelectronic Engineering*, vol. 132, pp. 46-57, 2015/01/25/ 2015.
- [19] M. Xia, P. Zhang, K. Qiao, Y. Bai, and Y.-H. Xie, "Coupling SPP with LSPR for Enhanced Field Confinement: A Simulation Study," *The Journal of Physical Chemistry C*, vol. 120, pp. 527-533, 2016/01/14 2016.
- [20] K. A. Willets and R. P. V. Duyne, "Localized Surface Plasmon Resonance Spectroscopy and Sensing," *Annual Review of Physical Chemistry*, vol. 58, pp. 267-297, 2007.
- [21] B. D. Gupta and R. Kant, "[INVITED] Recent advances in surface plasmon resonance based fiber optic chemical and biosensors utilizing bulk and nanostructures," *Optics & Laser Technology*, vol. 101, pp. 144-161, 2018/05/01/ 2018.
- [22] K. M. Mayer and J. H. Hafner, "Localized Surface Plasmon Resonance Sensors," *Chemical Reviews*, vol. 111, pp. 3828-3857, 2011/06/08 2011.
- [23] T. Akimoto, S. Sasaki, K. Ikebukuro, and I. Karube, "Refractive-index and thickness sensitivity in surface plasmon resonance spectroscopy," *Applied Optics*, vol. 38, pp. 4058-4064, 1999/07/01 1999.

- [24] P. Singh, "SPR Biosensors: Historical Perspectives and Current Challenges," *Sensors and Actuators B: Chemical*, vol. 229, pp. 110-130, 2016/06/28/ 2016.
- [25] W. L. Barnes, A. Dereux, and T. W. Ebbesen, "Surface plasmon subwavelength optics," *Nature*, vol. 424, pp. 824-830, 2003/08/01 2003.
- [26] T. W. Ebbesen, H. J. Lezec, H. F. Ghaemi, T. Thio, and P. A. Wolff, "Extraordinary optical transmission through sub-wavelength hole arrays," *Nature*, vol. 391, pp. 667-669, 1998/02/01 1998.
- [27] G. Gay, O. Alloschery, B. Viaris de Lesegno, C. O'Dwyer, J. Weiner, and H. J. Lezec, "The optical response of nanostructured surfaces and the composite diffracted evanescent wave model," *Nature Physics*, vol. 2, p. 262, 03/26/online 2006.
- [28] W. Yue, Z. Wang, Y. Yang, J. Li, Y. Wu, L. Chen, *et al.*, "Enhanced extraordinary optical transmission (EOT) through arrays of bridged nanohole pairs and their sensing applications," *Nanoscale*, vol. 6, pp. 7917-7923, 2014.
- [29] L. Tu, L. Huang, and W. Wang, "A novel micromachined Fabry-Perot interferometer integrating nano-holes and dielectrophoresis for enhanced biochemical sensing," *Biosensors and Bioelectronics*, vol. 127, pp. 19-24, 2019/02/15/ 2019.
- [30] M. Wang, C. Zhao, X. Miao, Y. Zhao, J. Rufo, Y. J. Liu, *et al.*, "Plasmofluidics: Merging Light and Fluids at the Micro-/Nanoscale," *Small*, vol. 11, pp. 4423-4444, 2015.
- [31] C. Pihoker, L. K. Gilliam, C. S. Hampe, and Å. Lernmark, "Autoantibodies in Diabetes," *Diabetes*, vol. 54, pp. S52-S61, 2005.
- [32] S. Smyth and A. Heron, "Diabetes and obesity: the twin epidemics," *Nature Medicine*, vol. 12, p. 75, 01/01/online 2006.
- [33] "Chapter One: Diabetes in children: epidemiology," *Pediatric Diabetes*, vol. 8, pp. 10-18, 2007.
- [34] M. Karvonen, M. Viik-Kajander, E. Moltchanova, I. Libman, R. LaPorte, and J. Tuomilehto, "Incidence of childhood type 1 diabetes worldwide. Diabetes Mondiale (DiaMond) Project Group," *Diabetes Care*, vol. 23, pp. 1516-1526, 2000.
- [35] D. M. Maahs, N. A. West, J. M. Lawrence, and E. J. Mayer-Davis, "Epidemiology of Type 1 Diabetes," *Endocrinology and Metabolism Clinics of North America*, vol. 39, pp. 481-497, 2010/09/01/ 2010.
- [36] M. A. Atkinson, G. S. Eisenbarth, and A. W. Michels, "Type 1 diabetes," *Lancet*, vol. 383, pp. 69-82, 2014.

- [37] A. G. Ziegler, M. Rewers, O. Simell, and et al., "Seroconversion to multiple islet autoantibodies and risk of progression to diabetes in children," *JAMA*, vol. 309, pp. 2473-2479, 2013.
- [38] D. B. Sacks and L. J. Kricka, "Plasmonic Chip Tackles Type 1 Diabetes Diagnosis," *Clinical Chemistry*, vol. 61, pp. 794-796, 2015.
- [39] B. Zhang, R. B. Kumar, H. Dai, and B. J. Feldman, "A plasmonic chip for biomarker discovery and diagnosis of type 1 diabetes," *Nature Medicine*, vol. 20, p. 948, 07/13/online 2014.
- [40] V. Singh and S. Krishnan, "Electrochemical and surface plasmon insulin assays on clinical samples," *Analyst*, vol. 143, pp. 1544-1555, 2018.
- [41] C. J. Greenbaum, J. P. Palmer, B. Kuglin, and H. Kolb, "Insulin autoantibodies measured by radioimmunoassay methodology are more related to insulin-dependent diabetes mellitus than those measured by enzyme-linked immunosorbent assay: results of the Fourth International Workshop on the Standardization of Insulin Autoantibody Measurement," *The Journal of Clinical Endocrinology & Metabolism*, vol. 74, pp. 1040-1044, 1992.
- [42] E. Liu and G. S. Eisenbarth, "Accepting Clocks that Tell Time Poorly: Fluid Phase Versus Standard ELISA Autoantibody Assays," *Clinical immunology (Orlando, Fla.)*, vol. 125, pp. 120-126, 09/27 2007.
- [43] Z. Zeng, X. Shi, T. Mabe, S. Christie, G. Gilmore, A. W. Smith, *et al.*, "Protein Trapping in Plasmonic Nanoslit and Nanoledge Cavities: The Behavior and Sensing," *Analytical Chemistry*, vol. 89, pp. 5221-5229, 2017/05/16 2017.
- [44] C. M. Pandey, S. Augustine, S. Kumar, S. Kumar, S. Nara, S. Srivastava, *et al.*, "Microfluidics Based Point-of-Care Diagnostics," *Biotechnology Journal*, vol. 13, p. 1700047, 2018.
- [45] Z. Zeng, M. N. Mendis, D. H. Waldeck, and J. Wei, "A semi-analytical decomposition analysis of surface plasmon generation and the optimal nanoledge plasmonic device," *RSC advances*, vol. 6, pp. 17196-17203, 02/03 2016.
- [46] J. Benesch, J. F. Mano, and R. L. Reis, "Analysing protein competition on self-assembled mono-layers studied with quartz crystal microbalance," *Acta biomaterialia*, vol. 6, pp. 3499-3505, 2010/09// 2010.
- [47] H. Ron, S. Matlis, and I. Rubinstein, "Self-Assembled Monolayers on Oxidized Metals. 2. Gold Surface Oxidative Pretreatment, Monolayer Properties, and Depression Formation," *Langmuir*, vol. 14, pp. 1116-1121, 1998/03/01 1998.

- [48] D. Berman and J. Krim, "Impact of oxygen and argon plasma exposure on the roughness of gold film surfaces," *Thin Solid Films*, vol. 520, pp. 6201-6206, 2012/07/31/ 2012.
- [49] J. Kang and P. A. Rowntree, "Gold Film Surface Preparation for Self-Assembled Monolayer Studies," *Langmuir*, vol. 23, pp. 509-516, 2007/01/01 2007.
- [50] J. Cao, T. Sun, and K. T. V. Grattan, "Gold nanorod-based localized surface plasmon resonance biosensors: A review," *Sensors and Actuators B: Chemical*, vol. 195, pp. 332-351, 2014/05/01/ 2014.
- [51] X. Huang, S. Neretina, and M. A. El-Sayed, "Gold Nanorods: From Synthesis and Properties to Biological and Biomedical Applications," *Advanced Materials*, vol. 21, pp. 4880-4910, 2009.
- [52] S. Link, M. B. Mohamed, and M. A. El-Sayed, "Simulation of the optical absorption spectra of gold nanorods as a function of their aspect ratio and the effect of the medium dielectric constant," *Journal of Physical Chemistry B*, vol. 103, pp. 3073-3077, 1999.
- [53] Z. Li, H. Zhang, X. Ge, Y. Liang, X. An, C. Yang, *et al.*, "A nanocomposite of copper(ii) functionalized graphene and application for sensing sulfurated organophosphorus pesticides," *New Journal of Chemistry*, vol. 37, pp. 3956-3963, 2013.
- [54] M. Sanders, Y. Lin, J. Wei, T. Bono, and R. G. Lindquist, "An enhanced LSPR fiber-optic nanoprobe for ultrasensitive detection of protein biomarkers," *Biosensors and Bioelectronics*, vol. 61, pp. 95-101, 2014/11/15/ 2014.
- [55] K.-L. Lee, W.-S. Wang, and P.-K. Wei, "Sensitive label-free biosensors by using gap plasmons in gold nanoslits," *Biosensors and Bioelectronics*, vol. 24, pp. 210-215, 2008/10/15/ 2008.

## CHAPTER VI

### CONCLUSION AND FUTURE CONSIDERATIONS

The primary theme of this dissertation was to develop new scientific understanding of plasmon-exciton coupling and to use the understanding to help development of nanostructured devices for energy conversion or for biosensing. The approaches and activities of the thesis included computational simulation-assisted device design, micro-nanofabrication, surface functionalization and testing of the corresponding optical properties. The phenomenon of plasmon-exciton coupling effect was examined in a few systems that either present the optical enhancement regarding photo-energy conversion or photo-electrical energy conversion. In chapter I, we provided an introduction of plasmon-exciton coupling and current state-of-arts in terms of the scientific concepts, background, recent findings and potential applications. Chapter II and III illustrated the fluorescence enhancement of CNDs confined in plasmonic nanoslit arrays. Chapter IV concentrated on the plasmonically enhanced photoelectrochemical cell with good efficiency and chapter V described a plasmonic nanoledge array design that was used for detection of protein biomarkers with high sensitivity and specificity.

In chapter II, gold nanoslit and nanoslit array of different width were introduced for enhanced fluorescence of CNDs. Different width nanoslit were chosen to get the optimized nanoslit width for enhanced fluorescence of CNDs. Fluorescence of CNDs was measured with or without nanoslit and nanoslit array of slit width, 50, 100, 200, 300, 400

and 500 nm. Experimental and theoretical results show maximum enhancement of CNDs when the CNDs were immobilized in 100 nm of nanoslit or nanoslit array. A 5X increase in fluorescence was reported when CNDs were used with the 100 nm width nanoslit or nanoslit array. This enhancement was explained on the basis of plasmon-induced resonance energy transfer (PIRET) and light trapping or scattering based on plasmon-exciton coupling between gold nanoslit or nanoslit array and CNDs. The findings of this study provide insights into the how CNDs fluorescence was enhanced, and the system may be utilized in photonic device development or biosensing application.

Plasmonic coupled gold nanoslit-CNDs-Au NPs hybrid system was proposed for further fluorescence enhancement of CNDs in chapter III. The above optimized gold nanoslit array of 100 nm width was chosen to investigate plasmon-plasmon coupling of gold nanoslit-Au NPs on the CNDs fluorescence. FDTD simulation was done for nanoslit array and nanoslit array with Au NPs to get better understanding of EM field intensity. CNDs fluorescence was observed in the solution both with or without Au NPs, and inside the gold nanoslit array both with and without Au NPs. It was observed that EM intensity was higher for nanoslit-Au NPs system which results in enhanced fluorescence of CNDs. Maximum fluorescence was observed when CNDs-Au NPs hybrid were immobilized inside the nanoslit array by SAM functionalization. Further, for the hybrid synthesis, different size of Au NPs was used to examine the effect of size on fluorescence of CNDs. It was observed that fluorescence was maximum when 20 nm of Au NPs were used, followed by 10 nm and minimum for 5nm of Au NPs. The difference in fluorescence with different size Au NPs was not much but it can be observable and fluorescence

intensities follows the same trend with the EM field intensity,  $E_{\text{Au}20\text{nm}} > E_{\text{Au}10\text{nm}} > E_{\text{Au}5\text{nm}} > E_{\text{M}}$ . The fluorescence enhancement was explained by two phenomena: plasmon-plasmon coupling and plasmon-exciton coupling. Plasmon-plasmon coupling between gold nanoslit and Au NPs enhanced the local electric field intensity around the CNDs which was utilized to dramatically enhance the fluorescence intensity of CNDs. Furthermore, energy trapping and PIRET between gold nanoslit-CNDs and Au NPs-CNDs generate more energetic electrons in CNDs, resulting more population of electrons in conduction band from valence band. More the number of electrons in the conduction band means more photoemission per unit time that eventually result in enhancement of CNDs fluorescence. This plasmon-coupling enhanced fluorescence phenomenon could be further utilized to develop platforms for highly sensitive sensing and imaging applications.

Chapter IV examined the plasmon-exciton coupling effect on light-electrical energy conversion. A single nanoslit photoelectrochemical cell was used to immobilize CNDs and  $\text{TiO}_2$  to realize the testing for dye-sensitized light energy conversion. The nanoslit device was designed and fabricated by microlithography and FIB. Nanoslit of 100 nm width was milled in the device which acts as a working electrode along with CNDs and  $\text{TiO}_2$  nanoparticles. CNDs and  $\text{TiO}_2$  nanoparticles were immobilized inside the nanoslit and whole system was placed inside an electrolyte solution to form photoelectrochemical cell. KCl and MB in PBS act as electrolyte solution which provides charge carriers to form a circuit for measuring electrical energy conversion. CNDs act as light sensitizer and  $\text{TiO}_2$  played a vital role by acting as a charge separator for photocurrent generation.

The i-v and p-v curve was measured with solar simulator both in presence of light and without light for the functionalized cell. Concentration of MB was also varied to see the effect of its concentration on the photocurrent generation and light energy conversion efficiency. It was noted that 20 mM of MB have the maximum efficiency as it balances the electron-hole pair in the solution. CNDs with TiO<sub>2</sub> nanoparticles result in absorbance of near UV and visible light wavelength range which further leads to increase in efficiency. The presence of gold nanoslit activates plasmon generation, which enhances the EM field intensity and leads efficiency of 4.07% while without the nanoslit the efficiency was only 0.28%. The enhanced photocurrent generation and efficiency was described by the plasmon-exciton coupling between gold nanoslit and CNDs. Presence of gold nanoslit concentrates more incident energy which non radiatively transferred to CNDs through PIRET to generate more electron-hole pairs in CNDs. These high energetic electrons transferred to gold electrode via TiO<sub>2</sub> nanoparticle and MB leading to enhanced photocurrent. These new findings potentially lead to the development of cost-effective solar cells with high efficiency and less engineering.

Chapter V described a plasmonic gold nanoledge array device and the use of as a plasmonic sensor chip for detection of protein biomarker of type 1 diabetes (T1D). Plasmonic nanoledge device had two openings, outer 280 nm and inner 50 nm, to efficiently capture the biomolecules. The device was functionalized with human insulin and then the different concentration of auto anti-insulin antibody in buffer and human serum were flown over the device. Binding events between the human insulin and auto anti-insulin antibody were monitored by resonant peak shift. The sensitivity of the device

was very high, with the range of detection  $\text{pg ml}^{-1}$  to  $100 \text{ ng ml}^{-1}$ . The selectivity of the device was tested by running control experiments using BSA and EGF of concentration  $20 \text{ ng ml}^{-1}$ . This new device with high sensitivity and selectivity can be used for detection or sensing of any biomolecules or biomarkers simply by functionalizing the device accordingly. The device can be reused simply by regenerating the metallic surface by subjecting the surface to oxygen plasma for cleaning, it is very cost effective and can be used with complex samples like human serum or blood. Future work will be to develop the device for multiple biomarker detection i.e. multiplexing simply by fabricating multiple channels into the device.

We believe the findings in this work present some advances in knowledge of plasmon-exciton coupling in newly designed systems which will aid facilitating the development of more advanced plasmonic based optical and biosensing devices.

**APPENDIX A**

**PLASMON ENHANCED FLUORESCENCE OF CNDS IN GOLD NANOSLIT**

**CAVITIES**

*Semi-analytical Analysis*

In order to study nanoslit geometries that are of interest in practice and consider the geometric diffraction with the bounded surface plasmon (SP) modes launching on the flat interfaces surrounding the slits, the SP scattering coefficients and efficiencies at the slit apertures need to be considered. With the semi-analytical model, the SPG efficiency,  $e$ , which is defined as the rate of surface plasmon polaritons launching and scattering by matching the continuous electromagnetic fields quantities at the interface, for the Au/glass interface at the bottom of the nanoslit aperture for one side of the aperture can be calculated using the following equations:

$$e = |\alpha^+(w/2)|^2 = |\alpha^-(w/2)|^2 = \frac{4w'n_1^3}{\pi n_2^2} \left| \frac{\varepsilon^{1/2}}{\varepsilon + n_1^2} \right| \left| \frac{I_1}{1 + (n_1/n_2)w'I_0} \right|^2$$

where,

$$I_0 = \int_{-\infty}^{\infty} du [\sin(\pi w'u)/(\pi w'u)]^2 / v$$

$$I_1 = \int_{-\infty}^{\infty} du \frac{\exp(-i\pi w'u)\sin(\pi w'u)/(\pi w'u)}{v\{v + [\frac{2}{1} / (\varepsilon + n_1^2)]^{1/2}\}}$$

$$w' = n_1 w / \lambda$$

where  $e$  is the SPG efficiency,  $\alpha$  is the SPG coefficient,  $w$  is the width of the nanoslit structure,  $\varepsilon$  is the dielectric constant,  $n$  is the refractive index,  $I$  is the integration calculation,  $w'$  represents the scaled width and  $u$  and  $v$  are applied for numerical integration with  $u^2 + v^2 = 1$ .

***Python Numerical Calculation used for solving semi-analytical model.***

```
import numpy as N
from scipy import special

def I0_integrand(u, w):
    return N.sinc(N.outer(u, w)) ** 2

def I1_integrand(u, w, gamma):
    v = N.sqrt(N.asarray(1 - u ** 2, dtype=complex))
    wu = N.outer(u, w)
    return N.sinc(wu) * N.exp(-1j * N.pi * wu) / (v + gamma)[:, N.newaxis]

def lalanne_integral(func, order=20, *args):
    points, weights = special.orthogonal.p_roots(order)
    x1, w1 = (N.pi / 4) * (points + 1), (N.pi / 4) * weights
    x2, w2 = (points + 1) / 2, weights / 2
    gauss1 = func(N.cos(x1), *args) + func(-N.cos(x1), *args)
    uuu = 1 / x2 - 1
    uu = N.sqrt(uuu ** 2 + 1)
    gauss2 = (func(uu, *args) + func(-uu, *args)) \
        * (((uuu + 1) ** 2) / uu)[:, N.newaxis]
    return (w1[:, N.newaxis] * gauss1).sum(axis=0) \
        - 1j * (w2[:, N.newaxis] * gauss2).sum(axis=0)

def calc_I0(w_norm):
    return lalanne_integral(I0_integrand, 20, w_norm)

def calc_I1(w_norm, epsilon, n):
    gamma_SP = -N.sqrt(n ** 2 / (n ** 2 + epsilon))
    return lalanne_integral(I1_integrand, 120, w_norm, gamma_SP)

def interface_calculation(w, w1, epsilon, n1, n2, theta):
```

```

w_norm = w * n1 / w1
temp = (n1 / n2) * w_norm * calc_I0(w_norm)
r0 = (temp - 1) / (temp + 1)
alpha = (-1j * (1 - r0) * calc_I1(w_norm, epsilon, n1)
        * N.sqrt((w_norm * n1 ** 2 / (n2 * N.pi))
        * (N.sqrt(N.abs(epsilon)) / (-epsilon - n1 ** 2))))
t0 = ((1 - r0) * N.sinc(w_norm * N.sin(theta))
      ) * N.sqrt(n1 / (n2 * N.cos(theta)))
beta = -alpha * t0 / (1 - r0)
return r0, t0, alpha, beta

```

def calculation():

```

# Iteration 1
w = N.array([0.1,0.2,0.3,0.4,0.5,0.6,0.7,0.8,0.9,1.0])
epsilon = -1.1148 + 6.4176j
I0 = calc_I0(w)
I1 = calc_I1(w, epsilon, 1.0)
print ' w
{0[0]:10.2} {0[1]:10.2} {0[2]:10.2} {0[3]:10.2} {0[4]:10.2} {0[5]:10.2} {0[6]:10.2} {0[7]:1
0.2} {0[8]:10.2} {0[9]:10.2}'.format(w)
print ' I0
{0[0]:10.2f} {0[1]:10.2f} {0[2]:10.2f} {0[3]:10.2f} {0[4]:10.2f} {0[5]:10.2f} {0[6]:10.2f} {0
[7]:10.2f} {0[8]:10.2f} {0[9]:10.2f}'.format(I0)
print ' I1
{0[0]:10.2f} {0[1]:10.2f} {0[2]:10.2f} {0[3]:10.2f} {0[4]:10.2f} {0[5]:10.2f} {0[6]:10.2f} {0
[7]:10.2f} {0[8]:10.2f} {0[9]:10.2f}'.format(I1)
print('\n');

# Iteration 2
w = N.array([0.1,0.2,0.3,0.4,0.5,0.6,0.7,0.8,0.9,1.0])
epsilon = -1.9435 + 3.8004j
I0 = calc_I0(w)
I1 = calc_I1(w, epsilon, 1.0)
print ' w
{0[0]:10.2} {0[1]:10.2} {0[2]:10.2} {0[3]:10.2} {0[4]:10.2} {0[5]:10.2} {0[6]:10.2} {0[7]:1
0.2} {0[8]:10.2} {0[9]:10.2}'.format(w)
print ' I0
{0[0]:10.2f} {0[1]:10.2f} {0[2]:10.2f} {0[3]:10.2f} {0[4]:10.2f} {0[5]:10.2f} {0[6]:10.2f} {0
[7]:10.2f} {0[8]:10.2f} {0[9]:10.2f}'.format(I0)
print ' I1
{0[0]:10.2f} {0[1]:10.2f} {0[2]:10.2f} {0[3]:10.2f} {0[4]:10.2f} {0[5]:10.2f} {0[6]:10.2f} {0
[7]:10.2f} {0[8]:10.2f} {0[9]:10.2f}'.format(I1)
print('\n');

```

```

# Iteration 3
w = N.array([0.1,0.2,0.3,0.4,0.5,0.6,0.7,0.8,0.9,1.0])
epsilon = -7.3203 + 1.6786j
I0 = calc_I0(w)
I1 = calc_I1(w, epsilon, 1.0)
print ' w\'
{0[0]:10.2} {0[1]:10.2} {0[2]:10.2} {0[3]:10.2} {0[4]:10.2} {0[5]:10.2} {0[6]:10.2} {0[7]:1
0.2} {0[8]:10.2} {0[9]:10.2}'.format(w)
print ' I0
{0[0]:10.2f} {0[1]:10.2f} {0[2]:10.2f} {0[3]:10.2f} {0[4]:10.2f} {0[5]:10.2f} {0[6]:10.2f} {0
[7]:10.2f} {0[8]:10.2f} {0[9]:10.2f}'.format(I0)
print ' I1
{0[0]:10.2f} {0[1]:10.2f} {0[2]:10.2f} {0[3]:10.2f} {0[4]:10.2f} {0[5]:10.2f} {0[6]:10.2f} {0
[7]:10.2f} {0[8]:10.2f} {0[9]:10.2f}'.format(I1)
print('\n');

# Iteration 4
w = N.array([0.1,0.2,0.3,0.4,0.5,0.6,0.7,0.8,0.9,1.0])
epsilon = -13.134 + 1.3044j
I0 = calc_I0(w)
I1 = calc_I1(w, epsilon, 1.0)
print ' w\'
{0[0]:10.2} {0[1]:10.2} {0[2]:10.2} {0[3]:10.2} {0[4]:10.2} {0[5]:10.2} {0[6]:10.2} {0[7]:1
0.2} {0[8]:10.2} {0[9]:10.2}'.format(w)
print ' I0
{0[0]:10.2f} {0[1]:10.2f} {0[2]:10.2f} {0[3]:10.2f} {0[4]:10.2f} {0[5]:10.2f} {0[6]:10.2f} {0
[7]:10.2f} {0[8]:10.2f} {0[9]:10.2f}'.format(I0)
print ' I1
{0[0]:10.2f} {0[1]:10.2f} {0[2]:10.2f} {0[3]:10.2f} {0[4]:10.2f} {0[5]:10.2f} {0[6]:10.2f} {0
[7]:10.2f} {0[8]:10.2f} {0[9]:10.2f}'.format(I1)
print('\n');
if __name__ == '__main__':
    calculation()

```

### ***Finite-Difference Time-Domain (FDTD) Simulations***

Numerical simulations were conducted using the FDTD method. To calculate the electric-magnetic field intensity profiles of the nanoslit a Lumerical FDTD method was used with the following simulation details. The background RI of the total mesh area was 1.0 (air). Perfectly matched layer (PML) was applied for the boundary conditions. The

indices of Au and glass followed the data of optical constants of solids. Electric-magnetic field distribution calculations were performed on the slit width of 50 nm, 100 nm, 200 nm, 300 nm, 400 nm, or 500 nm (Fig. S6). Fourier transform of the polarization, with help of the Drude-Lorentz model, was used in the model and its implementation into the FDTD formalism resulted in the transverse electric (TE) and transverse magnetic (TM) equations. TE equations can be solved using the components of  $E_x$ ,  $E_y$ , and  $H_z$  and TM equations can be solved using components of  $H_x$ ,  $H_y$  and  $E_z$ .

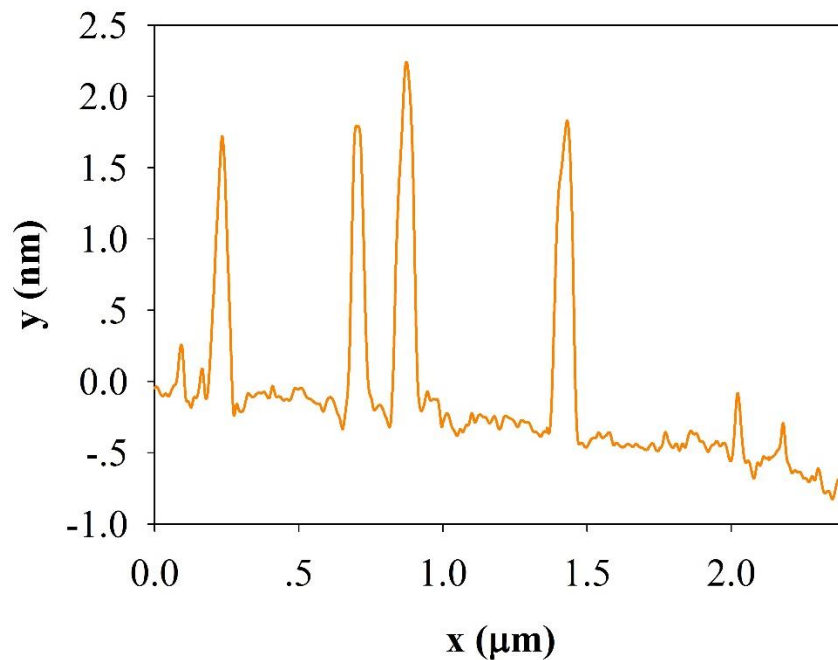


Figure S2.1. Height profile of CNDs (CNDs) measured by AFM.

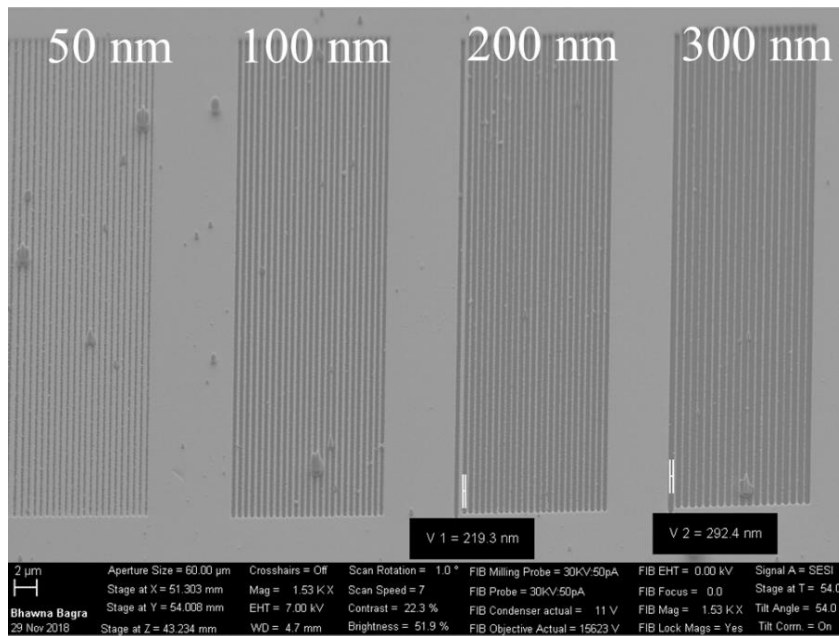
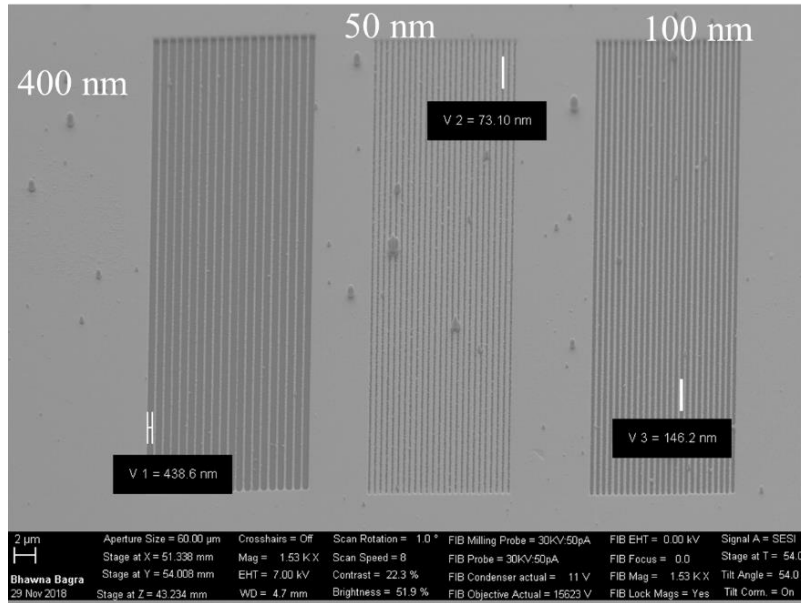
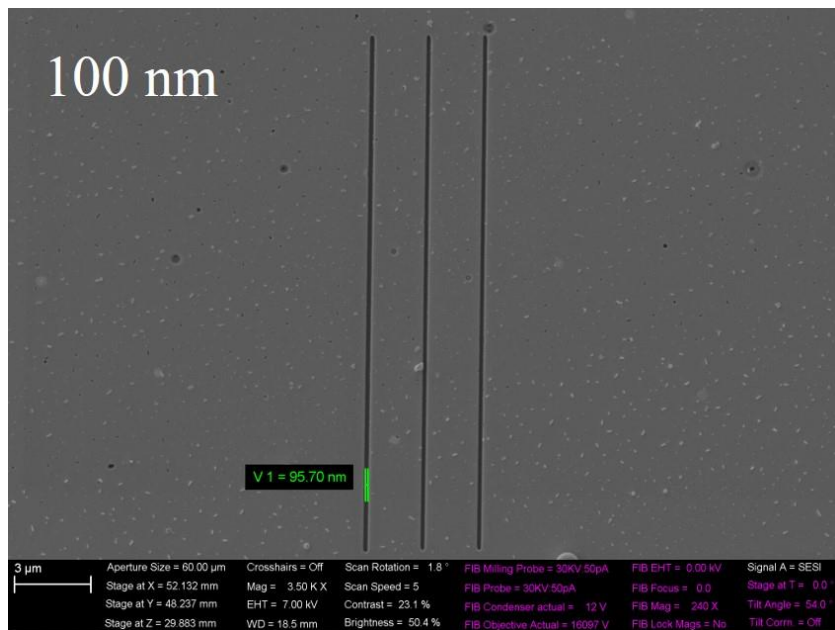
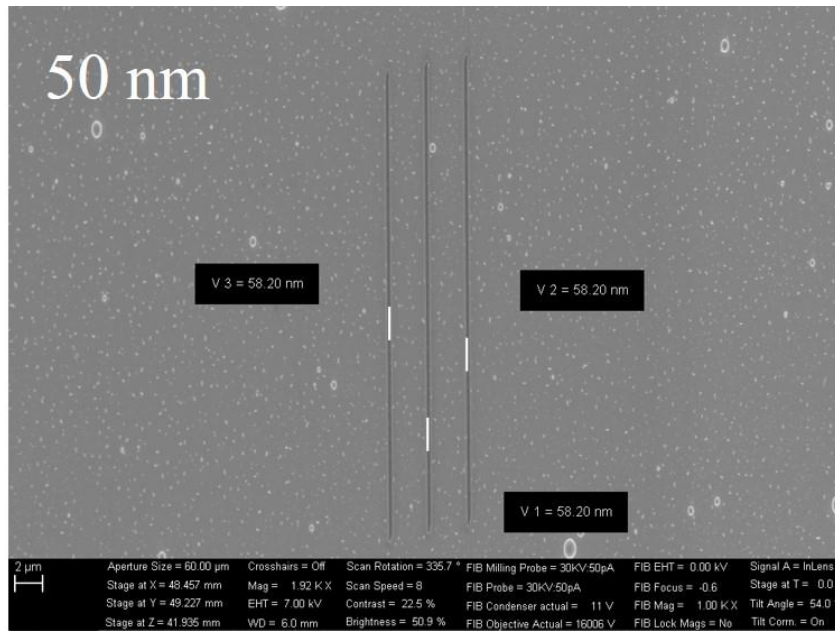
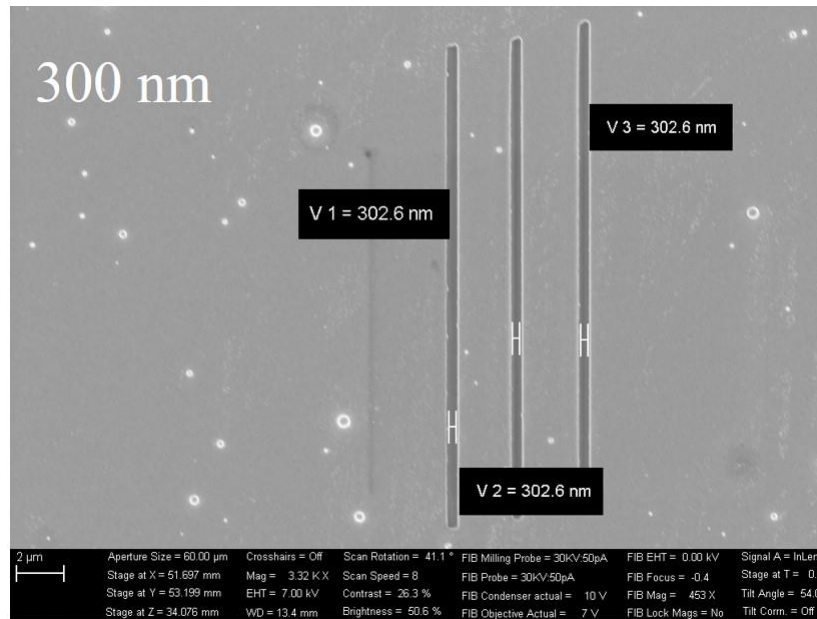
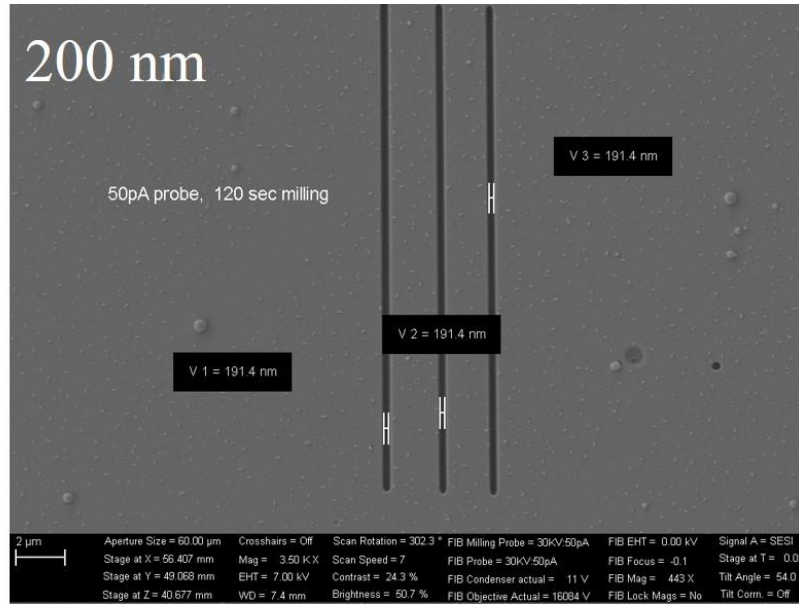


Figure S2.2. SEM images of the nanoslit array (width of 50 nm, 100 nm, 200 nm, 300 nm, or 400 nm).





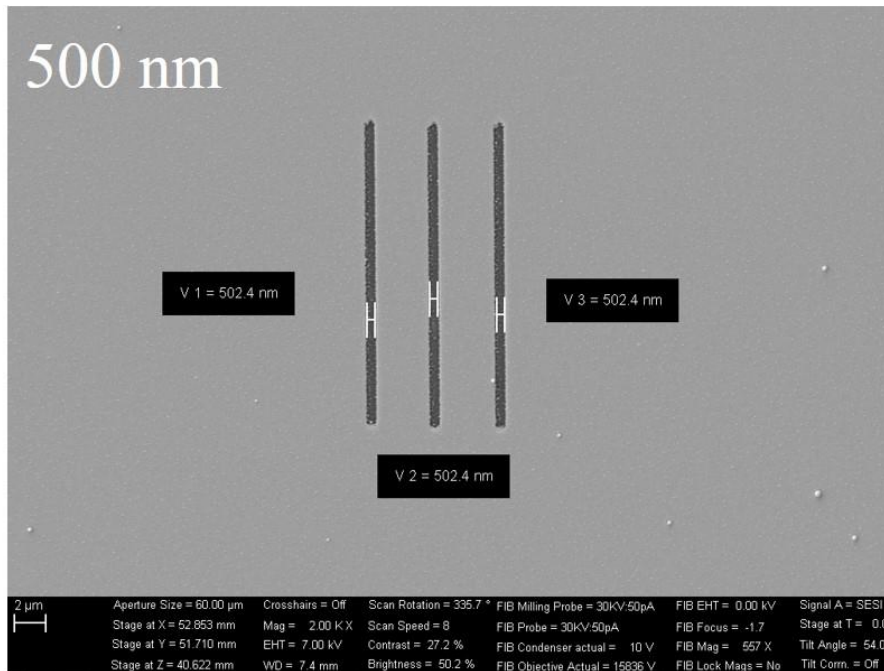
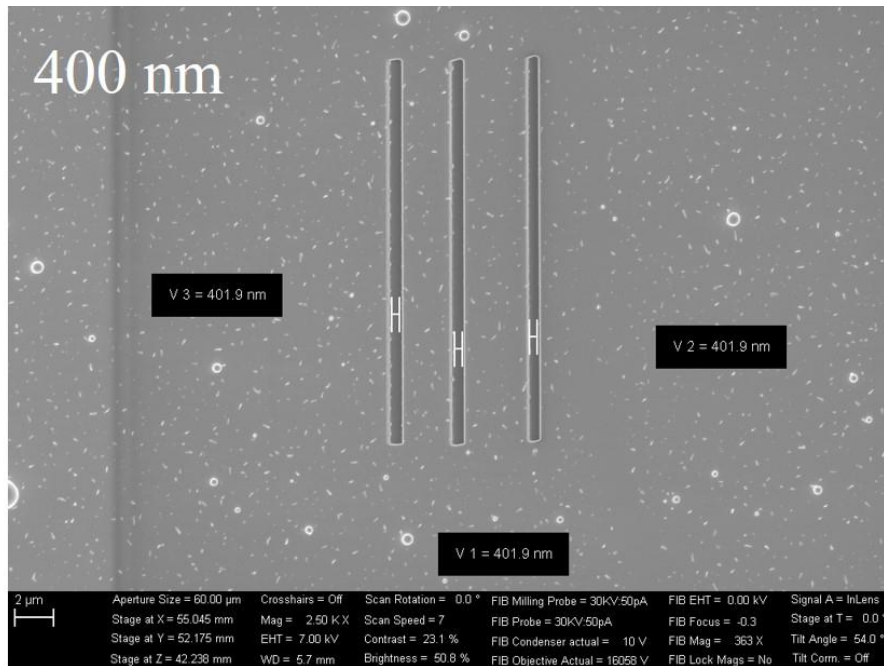


Figure S2.3. SEM images of the nanoslit (width of 50 nm, 100 nm, 200 nm, 300 nm, 400 nm or 500 nm)

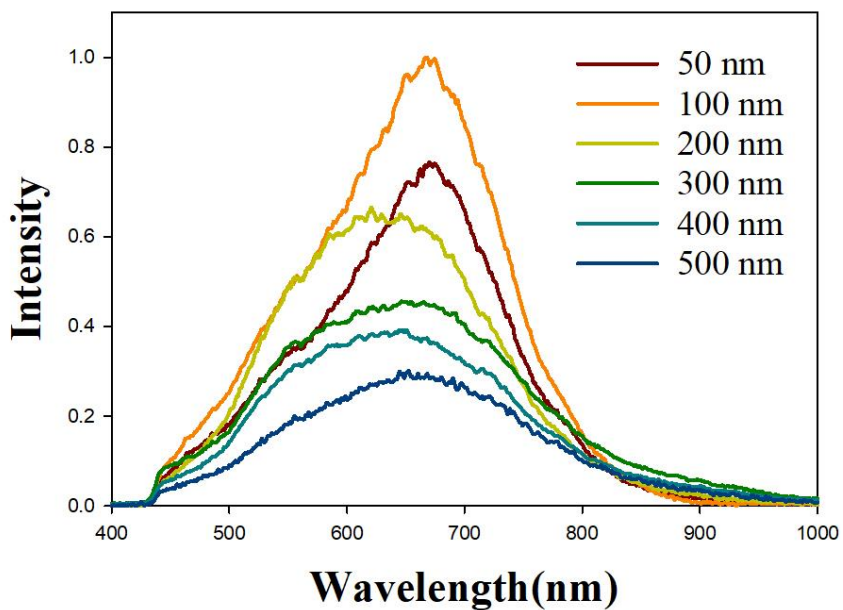
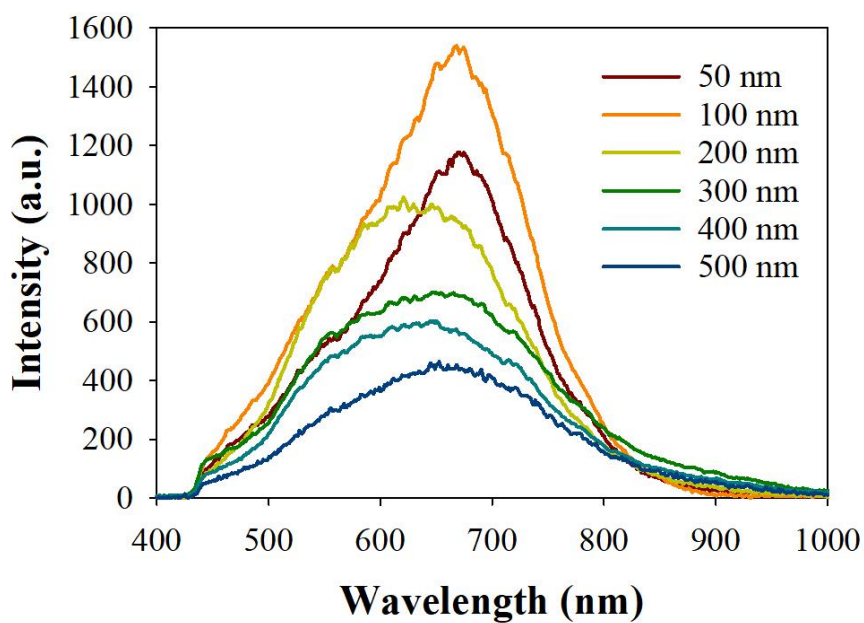


Figure S2.4. The absolute light reflection intensity (upper panel) and normalized intensity (lower panel) of the different nanoslit width before deposition of CNDs.

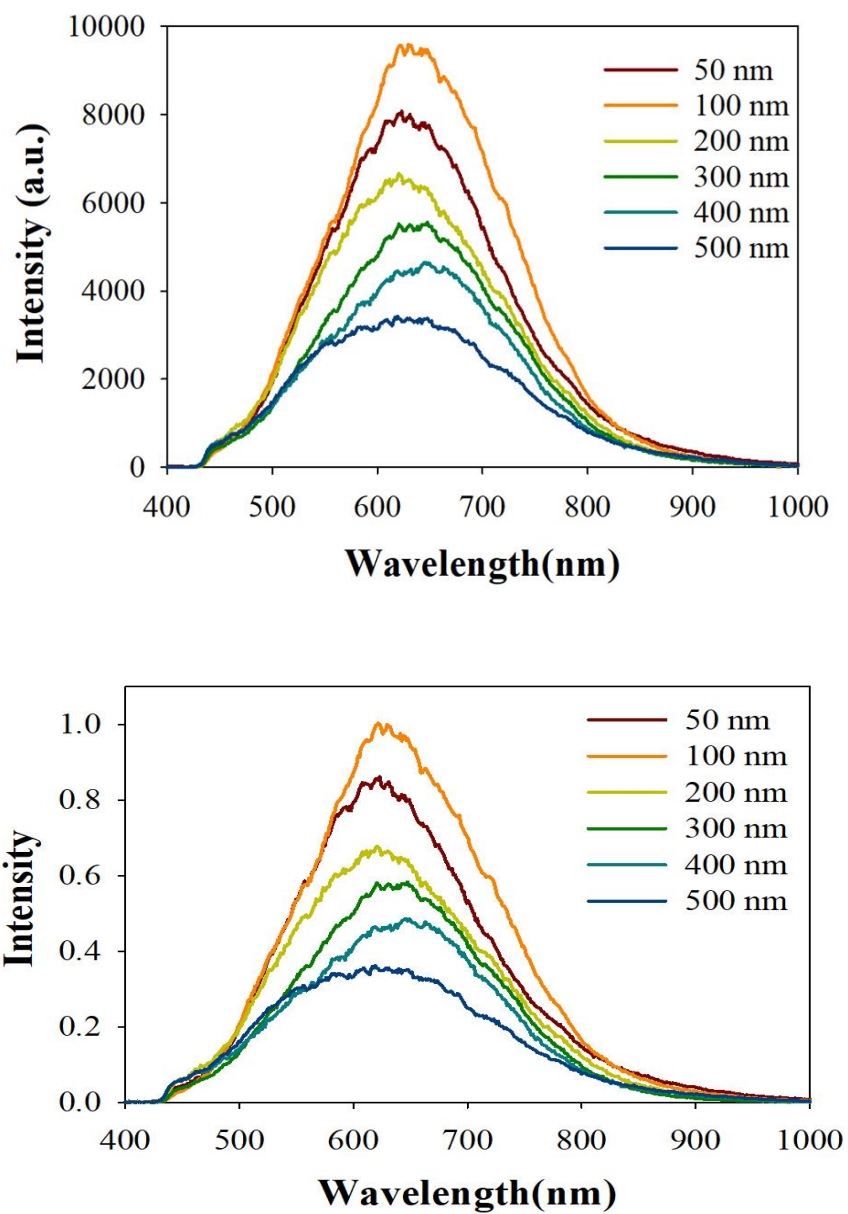


Figure S2.5. The absolute light reflection intensity (upper panel) and normalized intensity (lower panel) of the different nanoslit width after deposition of CNDs.

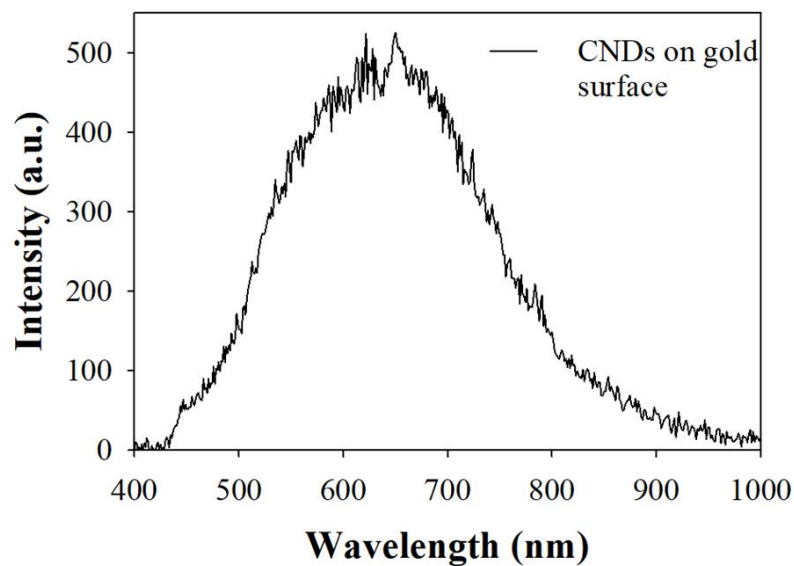


Figure S2.6. CytoViva hyperspectral light intensity spectrum of CNDs on gold surface

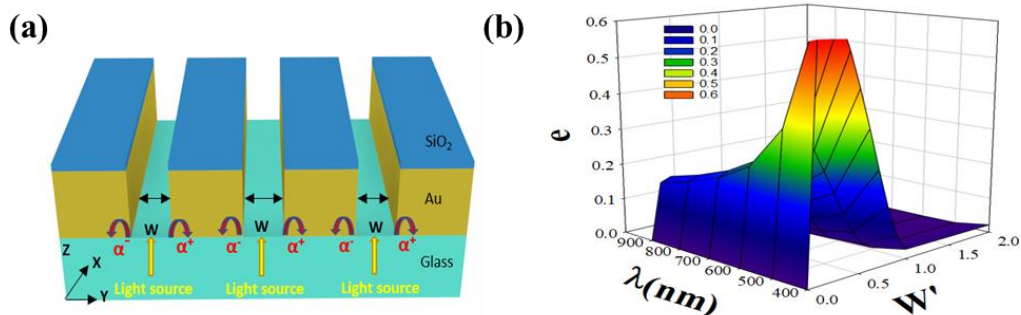


Figure S2.7. (a) The scheme illustrates the parameters to calculate the SPG efficiency “ $e$ ” for the nanoslit structure by a plane wave at normal incidence. (b) The SPG efficiencies  $e$  at the Au-glass interface are plotted as a function of  $\lambda$  and  $w'$  obtained by semi-analytical model.

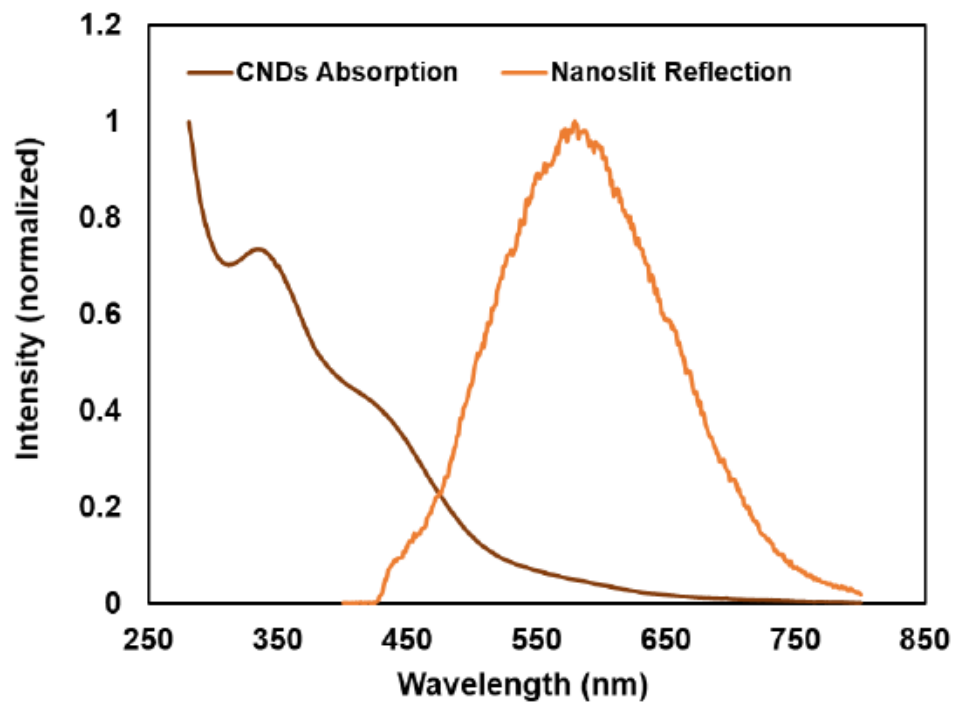


Figure S2.8. Plot of normalized absorption spectrum of CNDs reflection spectrum of nanoslit. The overlap of absorption and reflection is obvious.

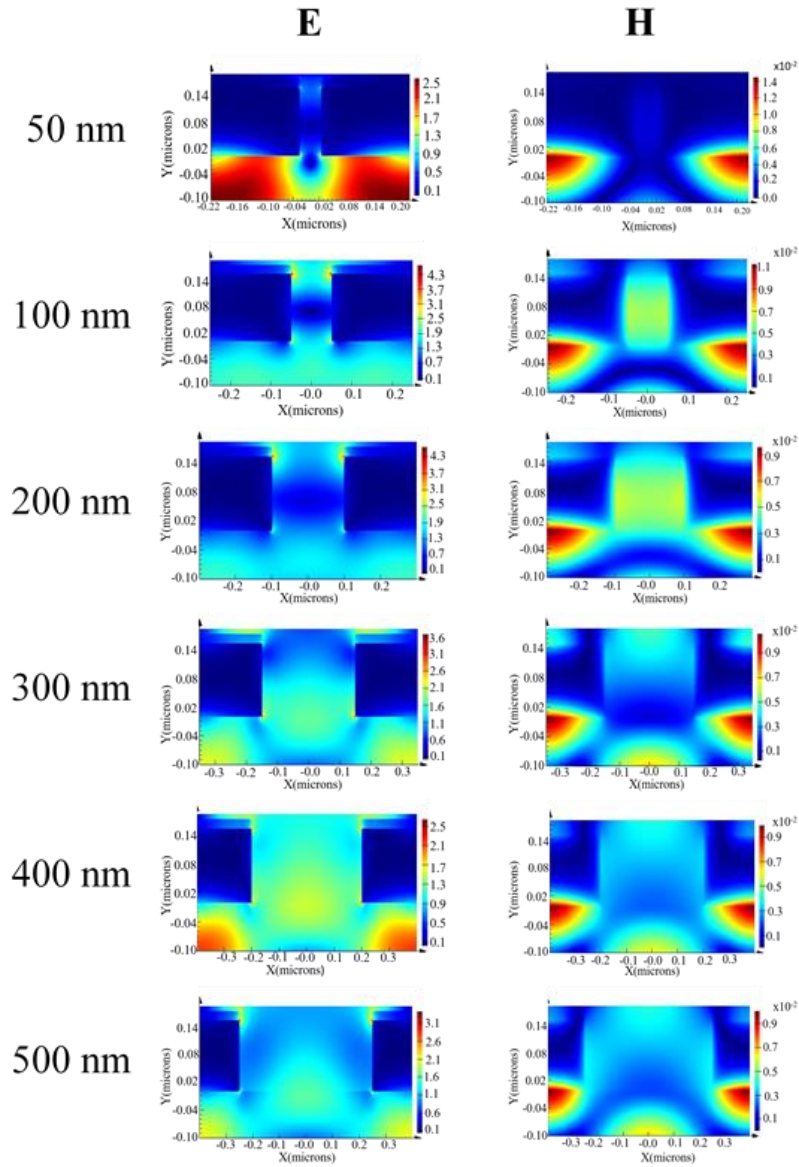


Figure S2.9. FDTD simulation of transverse electric-magnetic field intensity for different nanoslit structure. E: transverse electric field intensity; H: transverse magnetic field intensity. The units of electric field intensity ( $E^2$ ) is  $(V/m)^2$  and  $(A/m)^2$  is unit of magnetic field intensity.

Table S2.1. Intensity calculation for different width nanoslit array using 395-440 nm filter after the deposition of CNDs.

Slit width (nm)	Area Calculated	Mean Intensity	Standard Deviation
50 nm	990	253.575	4.71
100 nm	990	255.51	4.80
200 nm	990	222.00	0
300 nm	990	212.00	0
400 nm	990	161.661	3.21
Burn Box	990	43.94	8.45

Table S2.2. Intensity calculation for different width nanoslit array using 450-490 nm filter after the deposition of CNDs.

Slit width (nm)	Area Calculated	Mean Intensity	Standard Deviation
50 nm	990	238.87	5.88
100 nm	990	251.85	5.51
200 nm	990	231.60	7.54
300 nm	990	228.86	8.19
400 nm	990	225.45	10.90
Burn Box	990	19.88	6.51

Table S2.3. Intensity and surface plasmon generation efficiency calculation for different nanoslit.

Nanoslit width (nm)	Light intensity before CNDs deposition (a.u)	Light intensity after CNDs deposition (a.u)	SPG efficiency
50	1177.48, 32.81	8132.77, 533.7	0.336,0.185
100	1539.313, 46.7	9629.83, 529.8	0.341,0.151
200	1024.18, 138.19	6856.88, 472.1	0.224,0.054
300	701.37, 113.12	5878.44, 429.4	0.102,0.086
400	603.74, 63.82	4598.88, 425.5	0.0449,0.030
500	464.01, 75.91	3543.88, 327.1	0.018,0.015

Table S2.4. Intensity difference between the slit of different width before and after the deposition of CNDs.

Slit width (nm)	Before deposition of CNDs	After deposition of CNDs
100	1	1
50	0.76	0.85
200	0.60	0.67
300	0.45	0.57
400	0.39	0.47
500	0.30	0.35

Table S2.5.  $I_0$  and  $I_1$  for gold at different wavelengths when the refractive index  $n_2$  is 1.45 ( $I_0$  equals to each other for different  $\lambda$ ).

		<b>400nm</b> $\epsilon = -1.65+$ <b>5.7i</b>	<b>500nm</b> $\epsilon = -2.56+$ <b>3.6i</b>	<b>600nm</b> $\epsilon = -9.38+$ <b>1.5i</b>	<b>700nm</b> $\epsilon = -16.48+$ <b>1.0i</b>	<b>800nm</b> $\epsilon = -24.06+$ <b>1.5i</b>	<b>900nm</b> $\epsilon = -32.71+$ <b>1.9i</b>	<b>1000nm</b> $\epsilon = -41.84+$ <b>2.9i</b>
<b>w'</b>	<b><math>I_0</math></b>	<b><math>I_1</math></b>	<b><math>I_1</math></b>	<b><math>I_1</math></b>	<b><math>I_1</math></b>	<b><math>I_1</math></b>	<b><math>I_1</math></b>	<b><math>I_1</math></b>
0.1	3.09- 4.09i	0.01-3.46j	-0.24-3.26j	0.23-2.88j	0.42-2.90j	0.51-2.92j	0.57-2.93j	0.62-2.94j
0.2	2.94- 2.61i	0.84-3.12j	0.55-2.96j	0.96-2.48j	1.15-2.46j	1.25-2.47j	1.32-2.46j	1.37-2.46j
0.3	2.72- 1.69i	1.48-2.55j	1.16-2.46j	1.45-1.90j	1.63-1.83j	1.73-1.80j	1.80-1.78j	1.84-1.77j
0.4	2.43- 1.05i	1.85-1.84j	1.53-1.83j	1.66-1.24j	1.81-1.13j	1.90-1.07j	1.96-1.04j	2.00-1.01j
0.5	2.13- 0.64i	1.94-1.12j	1.64-1.19j	1.61-0.62j	1.72-0.48j	1.78-0.41j	1.82-0.36j	1.85-0.32j
0.6	1.82- 0.34i	1.76-0.49j	1.52-0.62j	1.36-0.14j	1.41+0.00j	1.45+0.08j	1.46+0.13j	1.48+0.17j
0.7	1.54- 0.18i	1.41-0.04j	1.24-0.21j	1.00+0.14j	1.00+0.27j	1.01+0.34j	1.01+0.38j	1.01+0.42j

0.8	1.30- 0.10i	0.99+0.18j	0.89+0.02j	0.63+0.23j	0.60+0.32j	0.59+0.37j	0.57+0.40j	0.56+0.43j
0.9	1.11- 0.06i	0.59+0.20j	0.55+0.06j	0.34+0.15j	0.30+0.20j	0.27+0.23j	0.26+0.25j	0.24+0.26j
1.0	0.97- 0.07i	0.30+0.07j	0.31-0.03j	0.17-0.01j	0.13+0.00j	0.12+0.01j	0.10+0.02j	0.09+0.02j
2.0	0.49- 0.02i	0.21-0.02j	0.20-0.03j	0.11-0.01j	0.09+0j	0.08+0.01j	0.07+0.01j	0.07+0.02j

Table S2.6. Surface plasmon generation efficiency calculation under different incident wavelengths for different nanoslit.

	50 nm	100 nm	200 nm	300 nm	400 nm	500 nm
400 nm	0.56	0.52	0.21	0.016	0.015	0.013
500 nm	0.66	0.65	0.39	0.10	0.024	0.023
600 nm	0.38	0.37	0.25	0.09	0.014	0.004
700 nm	0.26	0.27	0.21	0.12	0.03	0.004
800 nm	0.20	0.22	0.19	0.13	0.06	0.009
900 nm	0.15	0.19	0.17	0.13	0.08	0.03
1000 nm	0.14	0.17	0.15	0.13	0.09	0.04

## APPENDIX B

### DYADS OF AU NANOPARTICLES AND CARBON NANODOTS CONFINED IN PLASMONIC NANOSLITS FOR OPTICAL ENHANCEMENT

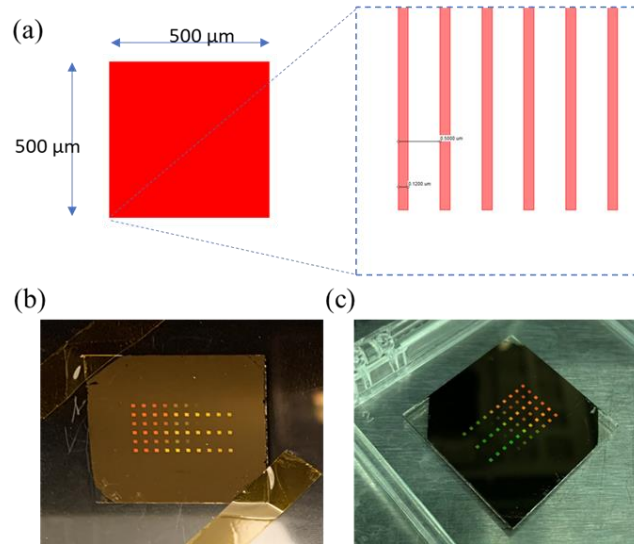


Figure S3.1. (a) shows the device design used for fabrication (b) and (c) shows the optical images of the final device fabricated.

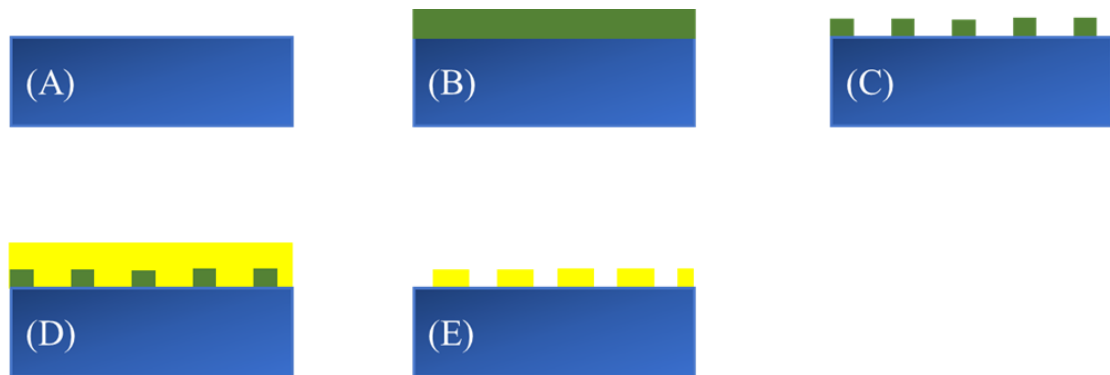


Figure S3.2. Fabrication Process for the Nanoslit array using E-beam lithography. (A) Cleaning of ITO coated glass substrate (B) Spin Apply maN-2403 resist and Soft Bake, (c) use E-beam with 1nA current and dose of  $184 - 258 \mu\text{C}/\text{cm}^2$  to write the pattern on resist, (D) Deposit 4nm/120 nm of Ti/Au atop of the pattern, (E) Lift-off the Au layer using 1165 solution to get the desired structure as shown in Figure.

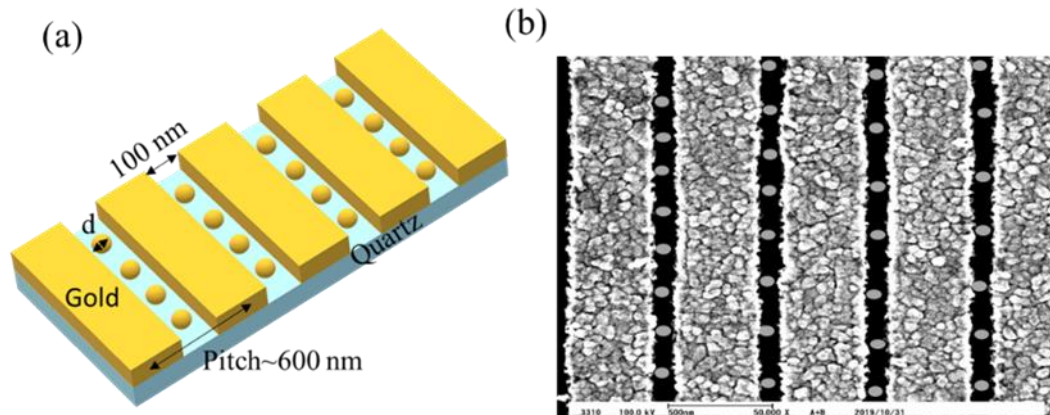


Figure S3.3. (a) The model used for FDTD calculation with gold nanoslits and Au nanoparticles (b) SEM image showing the nanoslit array with Au nanoparticles inside them.

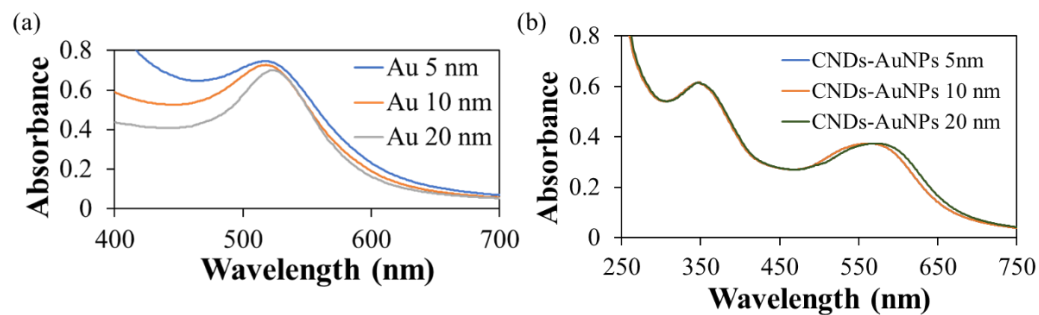


Figure S3.4. Absorption spectra for (a) different size of Au nanoparticles (b) CNDs-Au hybrid with different size of Au nanoparticles.

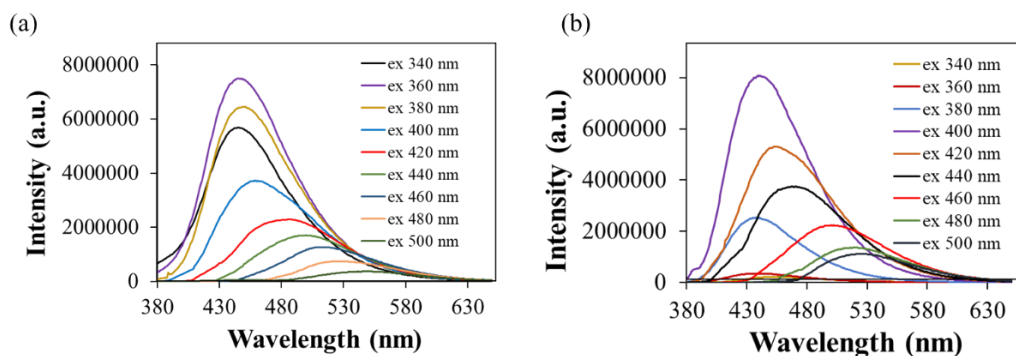


Figure S3.5. Fluorescence intensity spectra for (a) CNDs (b) CNDs-Au (10 nm of Au nanoparticles) hybrid at different excitation wavelength.

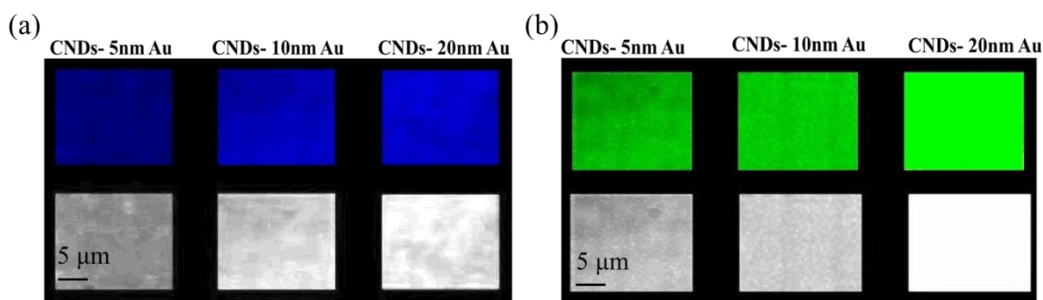


Figure S3.6. shows the fluorescence images and grey scale images taken using a light source with (a) 395–440 nm filter, (b) 450–490 nm filter, of the different CNDs-Au hybrid inside the nanoslit.

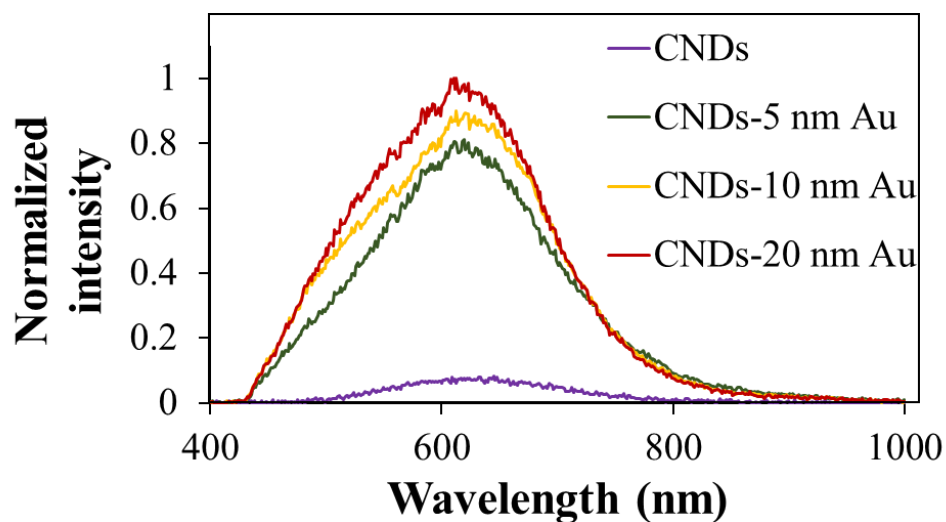


Figure S3.7. Normalized reflection light intensity spectra showing intensity for CNDs and different size CNDs-Au hybrid system.

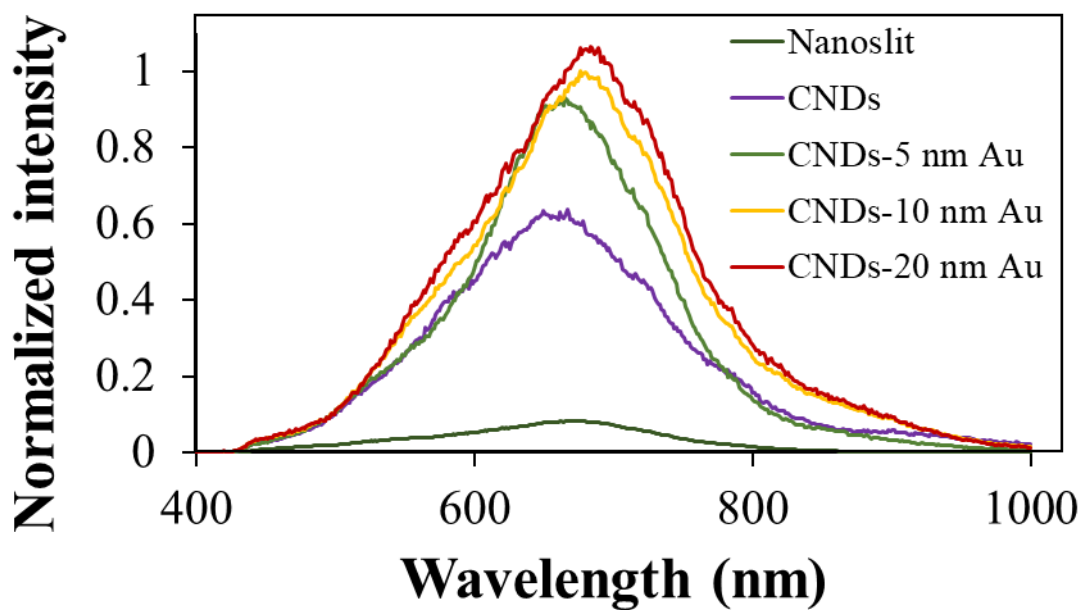


Figure S3.8. Normalized reflection light intensity spectra showing intensity for nanoslit, CNDs and different size CNDs-Au hybrid system inside the nanoslit.

Table S3.1. Fluorescence intensity calculated for different size CNDs-Au hybrids without using nanoslits with different filters.

Sample Name	Filter	Mean Intensity	Standard Deviation
CNDs	395-440 nm	65.469	2.670
	450-490 nm	84.795	3.291
CNDs- 5nm Au	395-440 nm	101.623	2.570
	450-490 nm	110.445	2.551
CNDs- 10nm Au	395-440 nm	106.848	8.366
	450-490 nm	113.24	2.166
CNDs- 20nm Au	395-440 nm	108.245	5.67
	450-490 nm	115.38	3.98
Au NPs	395-440 nm	5.197	1.008
	450-490 nm	2.053	1.530

Table S3.2. Fluorescence intensity calculated for different size CNDs-Au hybrids when placed inside the nanoslit array with different filters.

Sample Name	Filter	Mean Intensity	Area	Standard Deviation
CNDs	395-440 nm	102.289	886	3.029
	450-490 nm	108.776	886	4.641
CNDs- 5nm Au	395-440 nm	216.683	886	12.5
	450-490 nm	236.431	886	6.473
CNDs- 10nm Au	395-440 nm	223.129	886	8.802
	450-490 nm	248.852	886	6.288
CNDs- 20nm Au	395-440 nm	241.990	886	8.604
	450-490 nm	250	886	0
Au NPs	395-440 nm	5.197	886	1.008
	450-490 nm	2.053	886	1.530

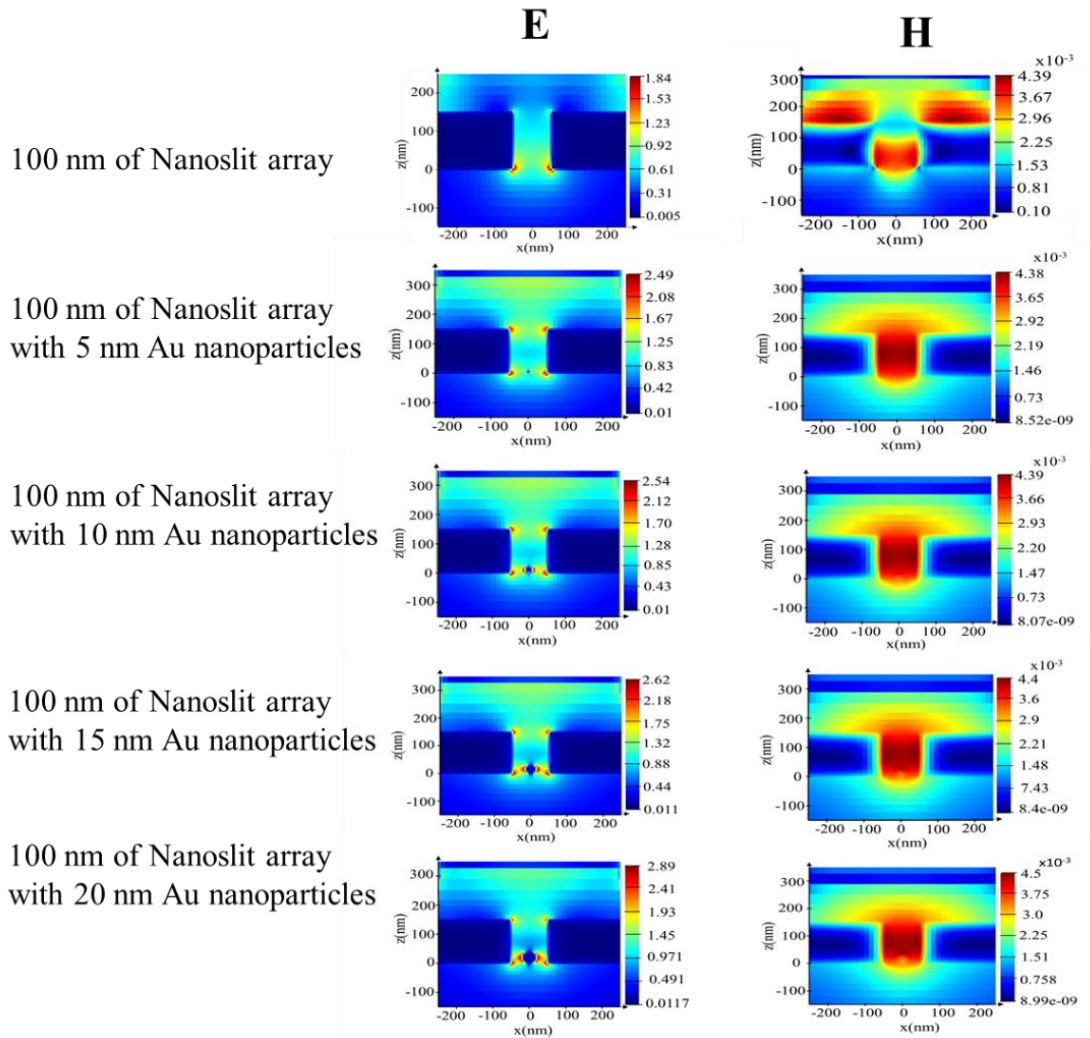


Figure S3.9. FDTD simulation showing the electro-magnetic field intensity for the various structure. E is transverse electric field intensity with the unit of  $(\text{v/m})^2$  and H is transverse magnetic field intensity with the unit of  $(\text{A/m})^2$ .

## APPENDIX C

### A PLASMONIC NANOEDGE ARRAY SENSOR FOR DETECTION OF ANTI-INSULIN ANTIBODY OF TYPE 1 DIABETES BIOMARKER

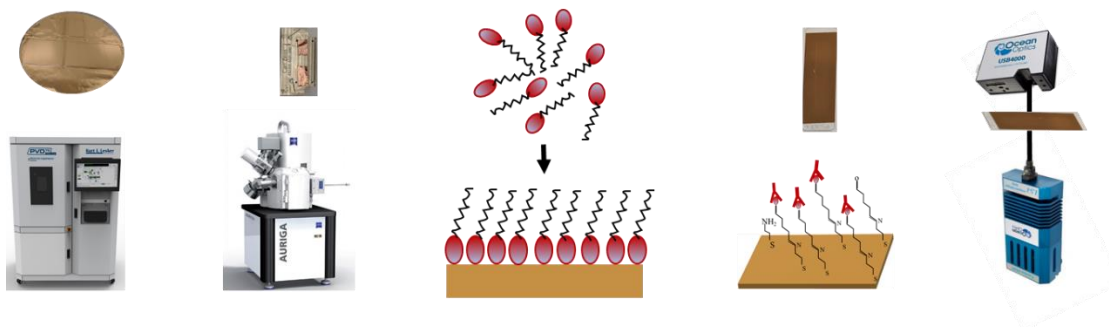


Figure S5.1. Schematic representation of different set-ups used for the fabrication and functionalization of the Plasmonic Nanoedge device.

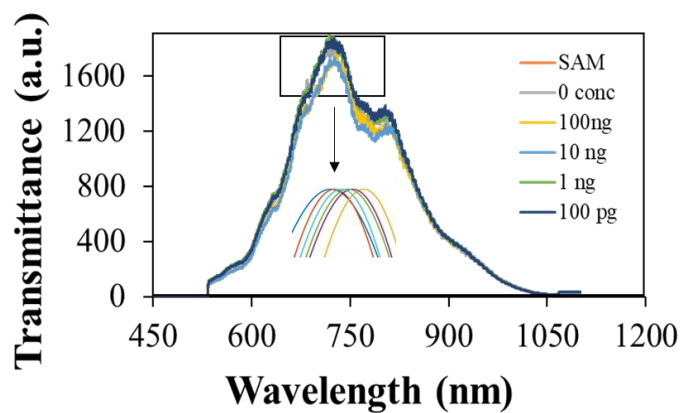


Figure S5.2. One of typical transmittance spectra showing peak shift of the various anti-insulin antibody concentration solutions in buffer when attached to human insulin in plasmonic nanoedge device.

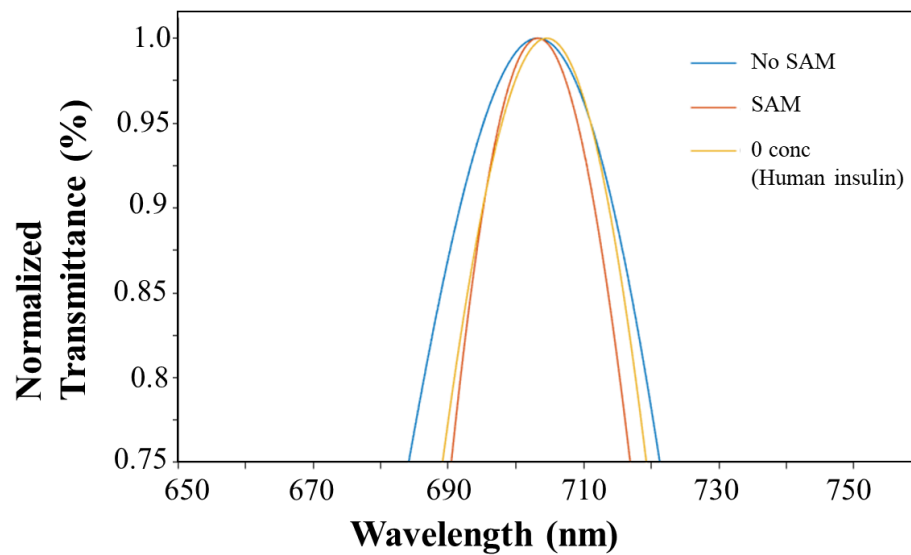


Figure S5.3. Transmittance spectra showing peak shift at each step of functionalization of plasmonic nanoledge device.

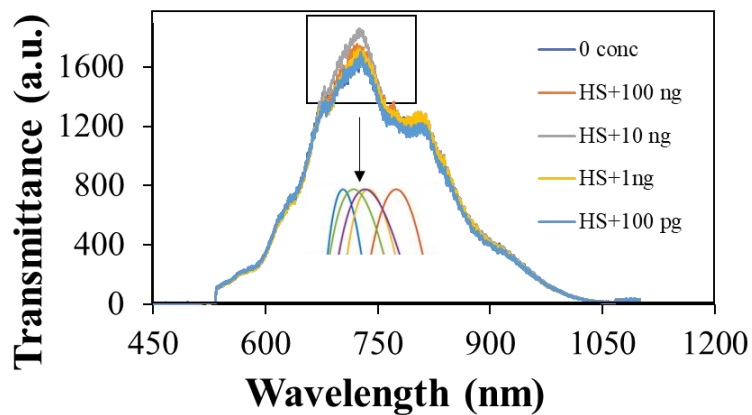


Figure S5.4. One of typical transmittance spectra showing peak shift of the various anti-insulin antibody concentration solutions in Human serum (HS) when attached to human insulin in plasmonic nanoledge device.

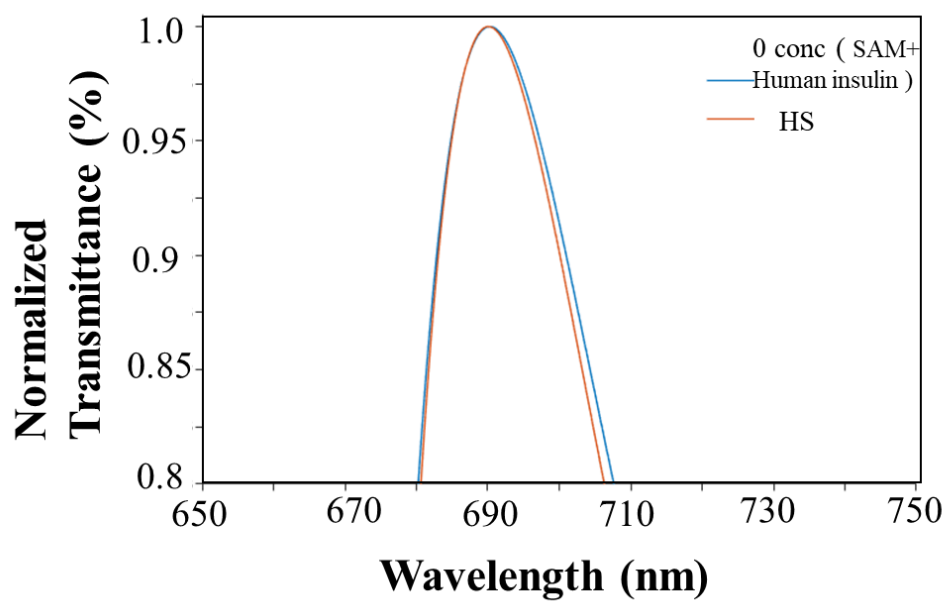


Figure S5.5. Transmittance spectra showing almost no peak shift or negligible peak shift (~0.207 nm) when Human serum (HS) was added to plasmonic nanoledge device attached human insulin, showing non-specific binding.

Table S5.1. A summary of the three sets of experiments in buffer with the peak positions (nm), peak shift and standard deviation.

	Trial 1	Trial 2	Trial 3	Avg. peak shift (nm)	Standard deviation
Blank (no SAM)	703.239			-	
0 conc (Human insulin)	705.128	703.288	704.363	-	1.032
100 pg	706.758	707.725	707.98	2.293	0.727
1 ng	708.792	708.08	709.973	4.682	0.910
10 ng	712.593	711.429	710.466	6.503	1.03
100 ng:	715.852	713.249	716.826	9.996	2.06

Table S5.2. A summary of the three sets of SAM control experiments in Human serum (HS) with the peak positions (nm), peak shift and standard deviation

	Trial 1	Trial 2	Trial 3	Avg. peak shift (nm)	Standard deviation
0 conc (Human insulin)	690.489	690.178	690.127	-	0.224
	691.78	692.453	694.12	2.893	1.34
100 pg	696.398	696.524	695.083	6.036	0.52
1 ng	698.528	697.499	698.371	7.962	0.63
10 ng	704.56	702.268	703.495	12.642	1.19
100 ng					

Table S5.3. Table showing peak position of BSA and EGF in presence of Human insulin in plasmonic nanoledge device

	SAM + Human insulin	BSA	EGF
Peak Position (nm)	697.86	697.757	697.655
Peak Shift (nm)		0.103	0.205

MATLAB code used for smoothing of graph

```

clear workspace;
clc;
M = readtable("HSA+diff conc 0 day.xlsx");
arr = M{:, :};

rowCount = size(arr, 1);
filteredArr = [];
for i=1:rowCount
    wavelength = arr(i, 1);
    if (wavelength > 680 && wavelength < 800)
        filteredArr = [filteredArr; arr(i, :)];
    end
end

wavelengths = filteredArr(:, 1);
c1 =filteredArr(:, 2);
c2 =filteredArr(:, 3);
c3 =filteredArr(:, 4);
c4 =filteredArr(:, 5);
c5 =filteredArr(:, 6);

[f1, e1] = polyfit(wavelengths, c1, 6);
c1_fit = polyval(f1, wavelengths, e1);

```

```
[f2, e2] = polyfit(wavelengths, c2, 6);  
c2_fit = polyval(f2, wavelengths, e2);  
  
[f3, e3] = polyfit(wavelengths, c3, 6);  
c3_fit = polyval(f3, wavelengths, e3);  
  
[f4, e4] = polyfit(wavelengths, c4, 6);  
c4_fit = polyval(f4, wavelengths, e4);  
  
[f5, e5] = polyfit(wavelengths, c5, 6);  
c5_fit = polyval(f5, wavelengths, e5);  
  
figure;  
plot(wavelengths, c1_fit);  
hold on;  
plot(wavelengths, c2_fit);  
hold on;  
plot(wavelengths, c3_fit);  
hold on;  
plot(wavelengths, c4_fit);  
hold on;  
plot(wavelengths, c5_fit);  
  
legend('HS+0 conc', 'HS+100 ng', 'HS+10 ng', 'HS+1 ng', 'HS+100 pg');
```